공학박사 학위논문

Arbitrary-order symplectic time integrator for the acoustic wave equation using the pseudo-spectral method

음향 파동방정식에 적용된 유사 스펙트럴 방법을

이용한 임의 차수의 심플렉틱 시간 적분법

2017 년 2 월

서울대학교 대학원

협동과정 계산과학전공

이 재 준

Arbitrary-order symplectic time integrator for the acoustic wave equation using the pseudo-spectral method

음향 파동방정식에 적용된 유사 스펙트럴 방법을 이용한
임의 차수의 심플렉틱 시간 적분법

지도 교수 신 창 수

이 논문을 공학박사 학위논문으로 제출함
2016 년 12 월

서울대학교 대학원
계산과학협동과정
이 재 준

이재준의 공학박사 학위논문을 인준함
2017 년 1 월

위 원 장 _____ (인)

부위원장 _____ (인)

위 원 _____ (인)

위 원 _____ (인)

위 원 _____ (인)

Abstract

A Hamiltonian system is symplectic. To simulate a Hamiltonian system, symplectic time integrators are generally applied; otherwise, the energy or the generalized energy is not conserved in the volume of interest. In this study, the symplectic nature of the acoustic wave system is proven. Then, a symplectic scheme that can be extended arbitrarily in temporal dimensions is suggested. The method is based on the Lax-Wendroff expansion of the time differentiation of acoustic wave variables, such as pressure and velocity, existing on the staggered time axis, i.e., one is on the integer grid, and the other is defined on the half integer of the time step. The series can be reduced to the pseudo-differential operator, which enables the application of other approximation techniques, such as the Jacobi-Anger expansion. By virtue of considering the property of the nature of the acoustic wave phenomena, the scheme is more stable and accurate than methods that do not consider symplecticity. Moreover, the phase error per time step can be kept sufficiently small to conduct simulation over long periods of time. According to the analysis of the scheme, the larger the time strides are, the more efficient the simulation is in terms of computing power when a sufficient number of multiplications of the map are accumulated. The effectiveness and accuracy are verified through simulation results using a homogeneous model in which the computed wavefield is equivalent to the analytic solution. The numerical results of the wavefield in the heterogeneous model also yield equivalent results irrespective of the time step lengths. The scheme can be applied to the source problems; however, the time step is confined to describing the entire frequency component of the wavelet.

Keywords : Symplectic time integrator, acoustic wave equation, pseudo-spectral method, extremely accurate simulation

Student number : 2012-30910

Contents

List of Figures

List of Tables

1. Introduction

1.1. Background

Imaging via migration techniques or inverse problems plays an essential role in characterizing the interior of a medium that does not allow direct inspection (e.g., the biopsy of body parts, drilling of land or slicing of complex mechanical parts) because of safety or economic issues, allowing decision-makers to understand the properties of the medium. The resulting images help decision-makers accurately evaluate the conditions because the data acquired via direct examination are reliable. However, locally confined information presents difficulties in realizing the broad tendency of the subsurface structure.

Numerical simulation of the wave propagation is the essential technique of imaging algorithms because it requires iteratively applying forward and adjoint wave modeling procedures once or many times (Baysal et al. 1983; Whitmore 1983; Tarantola 1983; Tarantola 1984; Pratt et al. 1998; Shin and Cha 2008; Shin and Cha 2009). We usually refer to the modeling algorithm as a 'modeling engine' because it generates the results (here, quality of the resulting image),

just as car engines do. The more accurate the modeling engine, the higher the resolution of the obtained image. To this end, various methodologies have been developed to improve the accuracy of wave phenomena simulations.

Discretization of the wave equation yields numerical errors, i.e., phase and amplitude errors. Such errors cause the simulation results to violate the dispersion relation of the wave phenomena. Marfurt (1984) analyzed the dispersion characteristics of the standard 5-point finite-difference (FD) method and 9-point finite-element method (FEM) using linear elements. The results of Marfurt's work suggest that the eclectic mass matrix, the weighted summation of the lumped mass matrix and the consistent mass matrix, decreases the dispersion error of standard FEM. Virieux (1986) introduced a FD scheme termed the staggered-grid finite-difference method (SGFDM) to simulate the seismic wave equation represented by a first-order system of stress and velocity fields. This method defines the wavefields and material properties in the staggered grids separately and updates the stress and velocity fields alternatively. Such grid and time stepping was adopted by Yee (1966) to simulate electromagnetic waves. Such gridding enables the even-odd decoupling to be suppressed to avoid generating high-frequency oscillation.

The scheme was extended by Levander (1988) using a fourth-order differential operator in space. This work confirmed that enlarging the stencil can reduce the dispersion error due to the discretized spatial operator. The coefficients of the large stencil operator are determined by solving equations of Taylor series expansion at the points (Fornberg 1988). Instead of the standard high-order FD coefficients, schemes using optimized coefficients to fit the

dispersion relation of the wave were introduced. (Tam and Webb 1993, Geller and Takeuchi 1998, Liu and Sen 2009, Liu and Sen 2011). A diamond shaped stencil was introduced by Liu and Sen (2013) and Tan and Huang for solving collocated and staggered grids, respectively. Using the dispersion-optimized coefficients, this scheme effectively reduces the numerical anisotropy. Liu and Sen (2013) also noted that the gridding relaxes the stability criterion allowing for a larger time step than that of the conventional FD scheme with the same order of accuracy in space. Ghost cell points are required outside of the computational domain address boundary condition when using large stencil schemes.

FEM-based schemes enlarge stencils in a different manner; they increase the density of the local nodes in the element. This approach enables the definition of a high-order basis to fit the solution function, which leads to a spectral convergence with respect to the order of accuracy. In the field of seismology, the spectral element method (SEM), a type of FEM technique is used in global seismic modeling (Komatitsch 1998). This method usually uses high-order Gauss-Lobatto collocation nodes to define nodal basis functions, which generates a diagonal global mass matrix naturally, allowing effective massive time-domain modeling. De Bassabe (2008) compared the dispersion characteristics of the elastic wave equation of the discontinuous Galerkin (DG) method with that of the SEM. DG schemes are non-conforming methods that evaluate the wave solution of each element separately and compensate the discontinuity of the solution with numerical flux terms such, as Godnov or Lax-Freidrich flux (Arnold et al. 2002; Hesthavan and Warburton 2007). Such

methods are used for special purposes when studying models that contain complex geometry, i.e., models with complex topography or interfaces of different phases, which is almost impossible to solve with FD schemes (Hermann et al. 2010).

A stability issue accompanies FEM-based schemes using high-order basis functions for the effective grid space, inversely proportional to the order of the basis function; the Courant Friedrichs Lewy (CFL) number can easily increase to exceed the stability criterion. The use of implicit methods, such as the Crank-Nicolson method (Crank and Nicolson 1947), alternating direction implicit (ADI) method (Fairweather and Mitchell 1967) or implicit locally one-dimensional (LOD) method (Kim and Lim 2007), can be a feasible solution. The implicit schemes are unconditionally stable in general, but they necessitate additional computational cost to conduct matrix inversion. Using a high-order explicit scheme is another potential solution. The Lax-Wendroff method (Lax and Wendroff 1964) expands the time derivative term using a Taylor expansion series and converts it to high-order spatial terms. This method has been successfully implemented to FEM-based schemes (Dumbser and Käser 2005; Käser and Dumbser 2006; Dumbser et al. 2007; Hermann et al. 2010; De Basabe and Sen 2010). Cohen and Joly (1986) and Dablain (1986) evaluated FD schemes of fourth-order accuracy in temporal dimensions using the Lax-Wendroff method; they found that method resolves stability and alleviates the time dispersion error. Tan and Huang (2014) extended the SGFDM to use the fourth- and sixth-order terms in time. Although they omitted certain high-order spatial derivative terms, the scheme enables the CFL relaxation effects, which

allows a larger time step. Such expansion can be implemented in a recursive manner, and we can arbitrarily increase the order of accuracy in time. Representation of the operator via exponential matrix form, i.e., pseudo-differential operator, provides different options in terms of the time-domain modeling philosophy to geophysicists such that, once the time step length is determined, the number of expansions can be determined to satisfy the stability and dispersion error criterion.

Tal-Ezer (1986) introduced the new concept of a wave marching technique to achieve spectral accuracy in the time domain. His method numerically expands the exponential matrix operator using a modified version of the Jacobi-Anger expansion to the extent of covering the highest spatial mode of the wavefield. Although it is clear that the Jacobi-Anger expansion is a best-fit approximation of sinusoidal functions, the Taylor expansion of the matrix operator produces similar solutions and is equivalent to the Lax-Wendroff method of arbitrary order. This point is addressed in the work of Pestana and Stoffa (2010), who adapted the one-step rapid expansion method (REM) of Kosloff et al. (1989) into a finite time-stepping method accommodating multi-source problems. Because of the freedom achieved in the time domain-dispersion error, pseudo-spectral (PS) methods are chiefly used. PS methods usually offer spectral accuracy in the spatial domain, which implies that the scheme is dispersion free within the describable band of wavenumber. The scheme incurs a pair of discrete Fourier transforms, i.e., forward and inverse, which can be accelerated using the fast Fourier transform (FFT) algorithm. Using PS, it is possible to achieve spectral accuracy in both the time and spatial

domains. However, reiteration of the FFT is required to calculate the pseudo-differential operator, which can be burdensome in certain applications. Although Etgen and Bradsberg-Dahl (2009) introduced a pseudo-analytic method to calculate the operator matrix in an effective manner, it is relatively error-prone in the high-wavenumber region using the heterogeneous model.

Lu and Schmid (1997) adopted symplectic integrators to solve the acoustic wave equation. Symplecticity is an intrinsic property of the fundamental laws of physics that have a conservative quantity such as mechanical energy in a closed system; the symplectic integrator is the time marching technique corresponding to such physics. The symplecticity is not equivalent to the accuracy of the model but the physical property to be obeyed, which confines the variables bounded in some level on the phase space and yields much more stable and improved solutions in long-term simulations. (Hairer et al. 2006). Alternatively, the accuracy simply means the approximation order. There exists a non-symplectic method of a given order, as well as the symplectic integrator. The latter is always better than the former. Symplectic time operators have been successfully applied to numerous problems in diverse fields, such as astronomy, modern physics, fluid dynamics, molecular dynamics and wave modeling.

Geophysicists are familiar with the Störmer–Verlet method, a second-order symplectic integrator, because the scheme is equivalent to the time marching strategy of the SGFDM, which alternatively updates stresses and velocities. To improve the accuracy, higher-order schemes have been devised. Ruth (1983) and Forest and Ruth (1990) invented the third- and fourth-order symplectic integrators. Another forth-order scheme, the symplectic Nyström method

(Okunbor and Skeel 1992), was implemented with an acoustic wave equation by Chen (2009). The result verified that the symplectic Nyström method yields better solutions than the explicit Lax-Wendroff method of the same order of accuracy. Yosida (1990) suggested methodology to derive higher-order symplectic schemes using the Baker-Campbell-Hausdorff (BCH) formula. However, the derivation process of the optimal coefficients is extremely cumbersome and yields multiple solutions. Another strategy is to expand and combine low-order symplectic integrators with well-known explicit time marching schemes, which is expected to be much easier than the schemes derived using the approach of Yosida (1990). Ma et al. (2011) applied a symplectic version of the Runge-Kutta (RK) method to the 2D seismic wave problem. Araujo et al. (2014) combined the velocity-Verlet scheme with the REM, which was successfully applied to the reverse time migration (RTM). Ma et al. (2015, 2016) extended the RK scheme up to the fourth order of accuracy, and it was also adapted to the RTM algorithm by Li et al. (2015).

1.2. Overview

This work is essentially an extension of the study of a high-order symplectic time integrator for the wave equation solver in the time domain. I invented a symplectic time integrator that can be extended to an arbitrary order of accuracy in the temporal dimension. The scheme is implemented for a first-order system of wave equations. Two types of wave equations are considered. One is the system dynamics of pressure and time derivative of pressure vectors, and the other is of pressure and velocity vectors. As the established symplecticity condition (Hairer et al. 2006) is valid only for the bilinear system, I generalized the condition to accommodate the multilinear system to determine whether the scheme is applicable to acoustic wave systems with respect to pressure and velocity fields. The suggested scheme combines the Störmer–Verlet method with the Lax-Wendroff method. The series of spatial derivatives is found to be the sine hyperbolic function series of the characteristic matrix, which can be approximated by another series such as one generated by the Jacobi-Anger expansion. The stability criterion of the suggested scheme when using PS approaches is calculated and proven to be more stable than the non-symplectic scheme of equivalent computational cost. The phase error (which is also termed the dispersion error) is analyzed, and the result illustrates the relation between the error and the degree of the approximation of the symplectic map with respect to given modeling geometries. These characteristics are also compared to those of the non-symplectic method to provide evidence of improvement in terms of accuracy and efficiency when considering symplecticity. Based on the analysis, a strategy to use the scheme is suggested and applied to several p-

wave velocity models to yield seismograms and time traces.

1.3. Outline

In the following section, I briefly review the system of the acoustic wave and prove the symplecticity of the system. The conventional symplectic integrators are introduced to be compared by the formulation of the arbitrary-order symplectic time integrator that is suggested in this study. In section 3, stability and dispersion characteristics of the suggested scheme are analyzed. Phase error analysis is also conducted to illustrate the quantitative effect of increasing the order of accuracy in time, which introduces the strategy to use this scheme effectively and efficiently. In section 4, the arbitrary-order symplectic time integrator is applied to the homogenous and synthetic model to verify the properties derived in the analysis section.

2. Theory

2.1. Acoustic wave equation

In this chapter, I briefly review the formulation method of the linearized acoustic wave motion. We consider the control volume in 3D space,

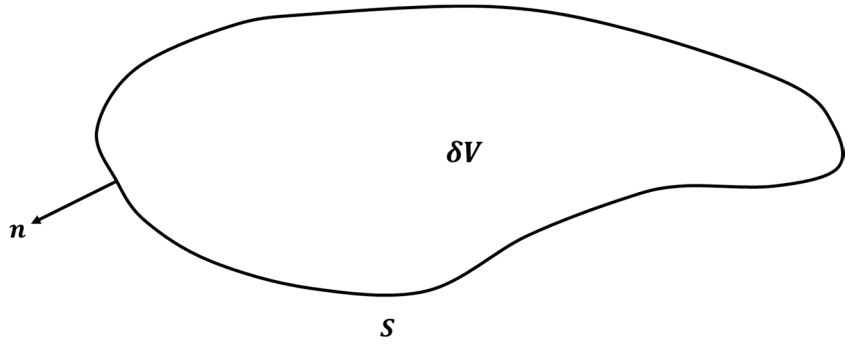

Figure 2.1 Control volume δV bounded by a surface S with n normal to S.

where δV is the control volume, S is the surface of the volume and n is the normal vector on the surface. The acoustic wave equation is formulated by representing the conservative relation of the fluid motion. First consider the mass conservation in the control volume δV and its surface S as follows:

$$\delta V \frac{\partial \rho}{\partial t} = -\int_S \rho_0 v \cdot n \, dS \tag{2.1.1}$$

where ρ is the density perturbation field, ρ_0 is the gauge density of the media, and $v = \{v_1, v_2, v_3\}$ is the velocity vector of the wave. Equation (2.1.1) implies that the mass change rate inside the volume δV is equivalent to the net mass flow rate across the surface S.

By applying Gauss' theorem,

$$\frac{\partial \rho}{\partial t} = -\rho_0 \nabla \cdot v \tag{2.1.2}$$

is derived. We secondly consider the momentum conservation law as follows:

$$\rho_0 \frac{\partial v}{\partial t} = -\nabla p \tag{2.1.3}$$

where p is the pressure field. The meaning of the acoustic wave as linearized motion is a natural assumption for the weakly perturbed field, and the relation between p and ρ is deduced as follows:

$$p = \frac{\partial p}{\partial \rho} \rho = c^2 \rho \tag{2.1.4}$$

where c is the wave propagation speed. With this relation, the mass conservation law (2.1.2) is reformulated as follows:

$$\frac{\partial p}{\partial t} = -\rho_0 \mathrm{c}^2 \nabla \cdot v \tag{2.1.5}$$

We can rewrite equations (2.1.5) and (2.1.3) in the first-order system equation form as follows:

$$\frac{\partial}{\partial t} \begin{bmatrix} p \\ v \end{bmatrix} = \begin{bmatrix} 0 & -\rho_0 \mathrm{c}^2 \nabla \cdot \\ -1/\rho_0 \nabla & 0 \end{bmatrix} \begin{bmatrix} p \\ v \end{bmatrix} \tag{2.1.6}$$

The system equation is considered to be fundamental for the implication of the physical law itself (LeVeque 2002) and adequate for modeling the multicomponent wavefields.

The wave equation itself is primarily described as a second-order form with respect to pressure or displacement vector, which is also termed the standard or primal form. A familiar formulation of the acoustic wave, i.e., the scalar partial differential equation (PDE) form with respect to pressure, is derived by eliminating the velocity term from equations (2.1.5) and (2.1.3) as follows:

$$\frac{1}{c^2}\frac{\partial^2 p}{\partial t^2} - \rho_0 \nabla \cdot \left(\frac{1}{\rho_0}\right) \nabla p = 0 \tag{2.1.7}$$

If we assume that the density or wave velocity is locally homogeneous or constant in space, equation (2.1.7) can be replaced by the standard form as follows:

$$\frac{1}{c^2}\frac{\partial^2 p}{\partial t^2} - \nabla^2 p = 0 \tag{2.1.8}$$

Such an assumption yields inaccurate wave simulation with the model rapidly changing in the space dimension; however, the errors are generally negligible for practical cases (Tan and Huwang 2014).

If we substitute the density ρ for pressure p using (2.1.4), we obtain

$$\frac{1}{c^2}\frac{\partial^2 \rho}{\partial t^2} - \nabla^2 \rho = 0 \tag{2.1.9}$$

As the differentiation of the wave equation also satisfies the wave equation and is proportional to the gradient of pressure, particle velocity also satisfies (2.8) as follows:

$$\frac{1}{c^2}\frac{\partial^2 v}{\partial t^2} - \nabla^2 v = 0 \tag{2.1.10}$$

where ∇^2 of (2.1.10) is the vector Laplacian. We can conjecture that the displacement vector also satisfies the wave equation if we integrate (2.10) over time t.

In addition, by taking the curl of (2.1.3),

$$\frac{\partial}{\partial t}(\nabla \times v) = 0 \tag{2.1.11}$$

is derived, which implies that the curl of the particle velocity vector is constant. It is valid from the initial state of rest, i.e., $v = 0$; thus,

$$\nabla \times v = 0 \tag{2.1.12}$$

is satisfied, which implies that the wave motion is irrotational and that the velocity potential function can be defined as follows:

$$v = \nabla\varphi \tag{2.1.13}$$

In some cases, it is convenient to express the wave motion with respect to φ, which guarantees the curl-free constraint of the wavefield. The momentum conservation law can be rewritten in terms of φ as follows:

$$\nabla\left(\rho_0 \frac{\partial\varphi}{\partial t} + p\right) = 0 \tag{2.1.14}$$

or

$$p = -\rho_0 \frac{\partial\varphi}{\partial t} \tag{2.1.15}$$

because we can set φ arbitrarily as the sum of the pressure field and set $\rho_0\, \partial\varphi/\partial t$ to be zero. Moreover, φ also satisfies the wave equation if we take the gradient of (2.1.10) as follows:

$$\frac{1}{c^2}\frac{\partial^2\varphi}{\partial t^2} - \nabla^2\varphi = 0 \tag{2.1.16}$$

Irrespective of the fact that the unstable weak motion of all the physical quantities satisfies the standard second-order wave equation, among the various formulations, (2.1.6) and (2.1.8) are used most frequently in practical problems.

In the following sections, we manage the structure of the acoustic wave in

the first-order system formulation. The standard second-order wave equation of various physical quantities above can be easily modified to a bilinear system equation of first order by introducing β, the time derivative of α, as follows:

$$\frac{\partial \beta}{\partial t} = c^2 \nabla^2 \alpha$$
$$\frac{\partial \alpha}{\partial t} = \beta \tag{2.1.17}$$

or

$$\frac{\partial}{\partial t}\begin{bmatrix}\alpha \\ \beta\end{bmatrix} = \begin{bmatrix}0 & I \\ c^2\nabla^2 & 0\end{bmatrix}\begin{bmatrix}\alpha \\ \beta\end{bmatrix} \tag{2.1.18}$$

Thus we can rewrite the acoustic wave system in a general form as follows:

$$\frac{\partial}{\partial t} y = My \tag{2.1.19}$$

where y is the vector of wave variables and M is the linear operator of the acoustic wave equation. M is referred to as the characteristic matrix of the system PDE because the eigenvalues of the operator determine the type of the PDE. The acoustic wave system is hyperbolic, as the eigenvalues M are all real values (Strikwerda 2004). The general solution of the initial value problem in the infinite media is

$$y = e^{tM} y_0. \tag{2.1.20}$$

where y_0 is the initial condition and e^{Mt} is the transformation matrix of the acoustic wave system.

In the following section, we analyze the interesting property of the symplecticity of the acoustic wave system and the transformation map using the first-order acoustic system formulations below:

$$\frac{\partial}{\partial t}\begin{bmatrix} p \\ v \end{bmatrix} = \begin{bmatrix} 0 & -\rho_0 \mathrm{c}^2 \nabla \cdot \\ -1/\rho_0 \nabla & 0 \end{bmatrix} \begin{bmatrix} p \\ v \end{bmatrix} \tag{2.1.21a}$$

$$\frac{\partial}{\partial t}\begin{bmatrix} p \\ \dot{p} \end{bmatrix} = \begin{bmatrix} 0 & 1 \\ c^2\nabla^2 & 0 \end{bmatrix} \begin{bmatrix} p \\ \dot{p} \end{bmatrix} \tag{2.1.21b}$$

In the following, I refer the wavefield of interest as

$$y = \begin{bmatrix} p \\ q \end{bmatrix} \tag{2.1.20}$$

where q is the counterpart of the pressure such as v or $\dot{p}$. The characteristic matrix M is composed of two submatrices S_i as follows:

$$M = \begin{bmatrix} 0 & S_1 \\ S_2 & 0 \end{bmatrix} \tag{2.1.22}$$

where S_1 corresponds to q and S_2 corresponds to p. I also define M_i to be the matrix filled with zero, except S_i, as follows:

$$\begin{aligned} M_1 &= \begin{bmatrix} 0 & S_1 \\ 0 & 0 \end{bmatrix} \\ M_2 &= \begin{bmatrix} 0 & 0 \\ S_2 & 0 \end{bmatrix} \end{aligned} \tag{2.1.23}$$

Then, the system equation of the acoustic wave is

$$\begin{aligned} \frac{\partial p}{\partial t} &= M_1 y = S_1 q \\ \frac{\partial q}{\partial t} &= M_2 y = S_2 p \end{aligned} \tag{2.1.24}$$

For instance, system (2.1.21a) satisfies the following:

$$y = \begin{bmatrix} p \\ v \end{bmatrix}$$

$$M = \begin{bmatrix} 0 & -\rho_0 \mathrm{c}^2 \boldsymbol{\nabla} \cdot \\ -1/\rho_0 \boldsymbol{\nabla} & 0 \end{bmatrix} \tag{2.1.25}$$

$$S_1 = -\rho_0 \mathrm{c}^2 \boldsymbol{\nabla} \cdot, \quad S_2 = {}^{-1}/_{\rho_0} \boldsymbol{\nabla}$$

$$M_1 = \begin{bmatrix} 0 & -\rho_0 c^2 \nabla \cdot \\ 0 & 0 \end{bmatrix}, \quad M_2 = \begin{bmatrix} 0 & 0 \\ -1/\rho_0 \nabla & 0 \end{bmatrix}$$

$$\frac{\partial p}{\partial t} = M_1 y = S_1 v$$

$$\frac{\partial q}{\partial t} = M_2 y = S_2 p$$

2.2. Symplecticity and symplectic time integrator

In this section, I briefly introduce the concept of symplecticity. Many problems in physics can be represented with Hamiltonian mechanics, which delineate the motion of mass via a bilinear system with respect to generalized coordinates and momentum. Symplecticity is an important property of Hamiltonian systems and indicates that the total mechanical energy in the system is conserved. As del Castilo and Linares (2003) confirmed, we can define the equivalent Hamiltonian structure for each standard acoustic wave equation in various physical quantities. However, (2.1.21a) is not a Hamiltonian system because the system is not in bilinear form; p is the scalar and $\boldsymbol{v}$ is the vector in 2- or 3-dimensions. Thus, in this work, I extend the definition of symplecticity to the multilinear map and show that (2.1.21a) is symplectic. For a deeper exposition, look for Goldstein (1980) and Hairer et al. (2006).

2.2.1. Symplecticity of the transformation map

Consider the system of p, q and r in $\mathbb{R}$, if there exist three vectors ξ, η and ζ in $\mathbb{R}^3$ that can be defined as follows:

$$\xi = \begin{bmatrix} \xi_p \\ \xi_q \\ \xi_r \end{bmatrix}, \ \eta = \begin{bmatrix} \eta_p \\ \eta_q \\ \eta_r \end{bmatrix}, \ \zeta = \begin{bmatrix} \zeta_p \\ \zeta_q \\ \zeta_r \end{bmatrix} \tag{2.2.1}$$

A parallelepiped L spanned by the three vectors in $\mathbb{R}^3$ space is

$$\begin{aligned} L = \{ & \left(s\xi_p + t\eta_p + u\zeta_p, s\xi_p + t\eta_q + u\zeta_r, s\xi_p + t\eta_q + u\zeta_r\right) \Big| \\ & 0 \le s \le 1, \ 0 \le t \le 1, \ 0 \le u \le 1 \}. \end{aligned} \tag{2.2.2}$$

The volume of L in (p, q, r) is calculated by a tensor product in Einstein

notation as follows:

$$V(\xi,\eta,\zeta) := \begin{vmatrix} \xi_p & \eta_p & \zeta_p \\ \xi_q & \eta_q & \zeta_q \\ \xi_r & \eta_r & \zeta_r \end{vmatrix} = \varepsilon_{lmn}\xi_l\eta_m\zeta_n \tag{2.2.3}$$

where ε_{ijk} is the Levi-Civita symbol, which is defined as follows:

$$\varepsilon_{ijk} = \begin{cases} 1 & \text{if even permulation of } i,j,k \\ -1 & \text{if odd permutation of } i,j,k \\ 0 & \text{otherwise} \end{cases} \tag{2.2.4}$$

The essential meaning of the symplecticity of the mapping is the preservation of area or volume in the state space, (p,q,r) in this case, which means that a linear transformation matrix $A\colon \mathbb{R}^3 \to \mathbb{R}^3$ is symplectic if

$$V(A\xi, A\eta, A\zeta) = V(\xi,\eta,\zeta) \text{ for all } \xi,\eta,\zeta \in \mathbb{R}^3 \tag{2.2.5}$$

Equation (2.2.5) is reduced to a simple relation as follows:

$$\varepsilon_{lmn}A_{li}A_{mj}A_{nk} = \varepsilon_{ijk} \tag{2.2.6}$$

Although the transformation map is nonlinear, we can approximate the map by a locally linear map using a Taylor series, which implies that a differentiable function $g\colon \mathbb{R}^3 \to \mathbb{R}^3$ is symplectic at $(\xi,\eta,\zeta) \in \mathbb{R}^3$ if the Jacobian matrix g' is symplectic:

$$V(g'\xi, g'\eta, g'\zeta) = V(\xi,\eta,\zeta) \quad \text{or} \quad \varepsilon_{lmn}{g'}_{li}{g'}_{mj}{g'}_{nk} = \varepsilon_{ijk} \tag{2.2.7}$$

This result implies that the infinitesimal parallelepiped dL at (ξ,η,ζ) preserves the volume after the transformation. If the structure $H = \varphi(K)$ in the state space where $K \subset \mathbb{R}^3$, its volume $\Omega(H)$ is the integration of small parallelepipeds spanned by three vectors defined at $(s,t,u) \in K$ as

$$\Omega(H) := \iiint_K V\left(\frac{\partial\varphi}{\partial s}, \frac{\partial\varphi}{\partial t}, \frac{\partial\varphi}{\partial u}\right) ds\, dt\, du \tag{2.2.8}$$

Then, the volume of the transformed structure via symplectic mapping g

satisfies

$$\Omega\big(g(H)\big) = \iiint_K V\left(\frac{\partial(g\circ\varphi)}{\partial s}, \frac{\partial(g\circ\varphi)}{\partial t}, \frac{\partial(g\circ\varphi)}{\partial u}\right) ds\, dt\, du = \Omega(H) \tag{2.2.9}$$

because $(g\circ\varphi)' = g(\varphi)'\varphi'$ and by the symplecticity condition of g.

Now, recall the acoustic system PDE (2.1.21b) and define a flow Ψ to be the Jacobian matrix of the wavefield vector with respect to its initial values p_0, u_0 and v_0 as follows:

$$\Psi = \begin{bmatrix} \frac{\partial p}{\partial p_0} & \frac{\partial p}{\partial u_0} & \frac{\partial p}{\partial v_0} \\ \frac{\partial u}{\partial p_0} & \frac{\partial u}{\partial u_0} & \frac{\partial u}{\partial v_0} \\ \frac{\partial v}{\partial p_0} & \frac{\partial v}{\partial u_0} & \frac{\partial v}{\partial v_0} \end{bmatrix} \tag{2.2.10}$$

The system equation of Ψ is as follows:

$$\frac{\partial}{\partial t}\Psi = \begin{bmatrix} 0 & -\rho_0 c^2 \frac{\partial^2}{\partial x^2} & -\rho_0 c^2 \frac{\partial^2}{\partial z^2} \\ -\frac{1}{\rho_0}\frac{\partial^2}{\partial x^2} & 0 & 0 \\ -\frac{1}{\rho_0}\frac{\partial^2}{\partial z^2} & 0 & 0 \end{bmatrix}\Psi \tag{2.2.11}$$

which can be derived by applying the Gâteaux derivative to (2.1.21a) with respect to the initial values. Then, it can be shown that flow Ψ is symplectic for all sufficiently small t if the flowing relation is satisfied.

$$\frac{\partial}{\partial t}\left(\varepsilon_{lmn}\Psi_{mi}\Psi_{nj}\Psi_{lk}\right) = \varepsilon_{lmn}\dot{\Psi}_{mi}\Psi_{nj}\Psi_{lk} + \varepsilon_{lmn}\Psi_{mi}\dot{\Psi}_{nj}\Psi_{lk} + \varepsilon_{lmn}\Psi_{mi}\Psi_{nj}\dot{\Psi}_{lk} = 0 \tag{2.2.12}$$

This result implies that the symplectic relation $\varepsilon_{lmn}\Psi_{li}\Psi_{mj}\Psi_{nk} = \varepsilon_{lmn}$ is satisfied elsewhere and at any time because Ψ is the identity matrix at $t = 0$

for any initial values in the phase space (p, u, w).

The symplectic condition (2.2.6) can be extended to a system of arbitrary dimension. In general, if a linear map $A: \mathbb{R}^n \to \mathbb{R}^n$ is symplectic,

$$\varepsilon_{l_1 l_2 \dots l_n} A_{l_1 i_1} A_{l_2 i_2} \dots A_{l_n i_n} = \varepsilon_{i_1 i_2 \dots i_n} \tag{2.2.13}$$

is satisfied. For instance, the two-dimensional system

$$J_{mn} A_{mi} A_{nj} = J_{ij} \tag{2.2.14}$$

is satisfied, which proves that system (2.1.21b) is also symplectic.

2.2.2. Symplectic time integrator

A symplectic time integrator is a special time marching scheme that is only applicable to a symplectic system, e.g., an acoustic wave system.

For relation (2.1.20), e^{Mt} is the transformation matrix of the acoustic wavefields, which is symplectic as shown in section 2.2.1. If we consider the propagation of the wavefields during a single time step Δt,

$$y_{n+1} = e^{\Delta t M} y_n \tag{2.2.15}$$

is satisfied, where $\boldsymbol{y}_n$ and $\boldsymbol{y}_{n+1}$ are the wavefield vectors at t and $t + \Delta t$, respectively. We cannot apply the transformation map in the exponential matrix, thus, an approximate map obtained from a Taylor series is typically used. The first-order Taylor series of $e^{\Delta t M}$ is

$$e^{\Delta t M} \simeq I + \Delta t M \tag{2.2.16}$$

The linear formulation using map (2.2.15) is

$$\boldsymbol{y}_{n+1} = (I + \Delta t M) \boldsymbol{y}_n \tag{2.2.17}$$

which is known as the explicit Euler method. This scheme is unconditionally unstable. The approximate map $I + \Delta t M$ is not symplectic, i.e. the scheme is

not a symplectic integrator, because the transformation map (2.2.15) does not satisfy the symplectic condition (2.2.13). It is not a matter of the order of accuracy that the high-order Taylor series of $e^{\Delta tM}$ does not satisfy (2.2.13) either.

Now, I consider the split operator $e^{\Delta tM}$ as follows:

$$e^{\Delta tM} = e^{\Delta t(M_2+M_1)} \simeq e^{\Delta tM_2} e^{\Delta tM_1} + O(\Delta t^2) \tag{2.2.18}$$

The Taylor series of the first order of each split operator leads to a linear formulation as follows:

$$y_{n+1} = (I + \Delta tM_2)(I + \Delta tM_1)y_n \tag{2.2.19}$$

which is known as the symplectic Euler method. Although the order of accuracy with respect to time is the same as in the explicit Euler method, the scheme is conditionally stable. As we expect, the system is symplectic since the split operator satisfies (2.2.13).

The characteristic feature of the symplectic Euler method is the alternate update of the variables, i.e., we update one variable first and then update the other using the updated variable. In the case of the acoustic system, the symplectic Euler method updates p and q alternatively by two stages as follows:

$$\begin{aligned} p_{n+1} &= p_n + \Delta tS_1 q_n \\ q_{n+1} &= q_n + \Delta tS_2 p_{n+1}. \end{aligned} \tag{2.2.20}$$

The second-order symplectic integrator, the Störmer–Verlet method, is generally used and approximates the transform map in three alternating stages as follows:

$$e^{\Delta tM} \simeq e^{\frac{1}{2}\Delta tM_1} e^{\Delta tM_2} e^{\frac{1}{2}\Delta tM_1} + O(\Delta t^3) \tag{2.2.21}$$

Then,

$$y_{n+1} = \left(I + \frac{\Delta t}{2} M_1\right)(I + \Delta t M_2)\left(I + \frac{\Delta t}{2} M_1\right) y_n \tag{2.2.22}$$

or

$$\begin{aligned} p_{n+1/2} &= p_n + \frac{1}{2}\Delta t S_1 q_n \\ q_{n+1} &= q_n + \Delta t S_2 p_{n+1/2} \\ p_{n+1} &= p_{n+1/2} + \frac{1}{2}\Delta t S_1 q_{n+1} \end{aligned} \tag{2.2.23}$$

is satisfied. This scheme consists of three stages to march one time step, and this approach can easily be modified to a two-step method if the operator is adapted as follows:

$$\begin{aligned} & e^{\frac{1}{2}\Delta tM_1} e^{\Delta tM_2} e^{\frac{1}{2}\Delta tM_1} \\ \simeq\ & e^{\frac{1}{2}\Delta tM_1} e^{\Delta tM_2} e^{\Delta tM_1} e^{-\frac{1}{2}\Delta tM_1} \end{aligned} \tag{2.2.24}$$

Then,

$$\begin{aligned} y_{n+1} &= e^{\frac{1}{2}\Delta tM_1} e^{\Delta tM_2} e^{\Delta tM_1} e^{-\frac{1}{2}\Delta tM_1} y_n \\ e^{-\frac{1}{2}\Delta tM_1} y_{n+1} &= e^{\Delta tM_2} e^{\Delta tM_1} e^{-\frac{1}{2}\Delta tM_1} y_n \end{aligned} \tag{2.2.25}$$

is satisfied. I define the acoustic wave vector $\overline{y}_n$ as

$$\overline{y}_n = e^{-\frac{1}{2}\Delta tM_1} y_n = \begin{bmatrix} p_n \\ q_{n-1/2} \end{bmatrix} \tag{2.2.26}$$

which sets the variables on the staggered grid on the time axis. Then, equation (2.2.25) is

$$\overline{y}_{n+1} = e^{\Delta tM_2} e^{\Delta tM_1} \overline{y}_n \tag{2.2.27}$$

or

$$\overline{y}_{n+1} = (I + \Delta t M_2)(I + \Delta t M_1)\overline{y}_n \tag{2.2.28}$$

Yosida (1990) suggested methodology to approximate the symplectic map e^{Mt} in the general order of accuracy as follows:

$$e^{\Delta t M} = e^{\Delta t(M_2+M_1)} \simeq \prod_{i=1}^{k} e^{d_i \Delta t M_2} e^{c_i \Delta t M_1} + O\left(\Delta t^{k+1}\right) \tag{2.2.29}$$

where $\sum_{i=1}^{k} c_i = \sum_{i=1}^{k} d_i = 1$. The coefficients c_i and d_i are determined by applying the BCH formula repeatedly to build higher-order symplectic schemes using the coefficients of the lower-order method. However, it is not unique in determining the coefficients of the scheme, particularly for higher orders. As confirmed in Table 2.1, several different ways to approximate the symplectic map in third-order accuracy have been suggested.

The symplectic time integrator mentioned above requires multiple stages to update one time step. For instance, the third order of the accurate symplectic integrator discovered by Ruth (1983) approximates the transform map in six separate stages as follows:

$$e^{\Delta t M} \simeq e^{\frac{7}{24}\Delta t M_2} e^{\frac{2}{3}\Delta t M_1} e^{\frac{3}{4}\Delta t M_2} e^{-\frac{2}{3}\Delta t M_1} e^{-\frac{1}{24}\Delta t M_2} e^{\Delta t M_1} \tag{2.2.30}$$

This approach is relatively cumbersome to implement and is inflexible when one is attempting to alter the order of accuracy of the scheme because it is impossible to find any rule of the composition and order of the coefficients between each scheme in different orders.

In the next section, I suggest a symplectic time integrator that is governed by a simple and consistent rule to arbitrarily increase the order of accuracy in time.

Table 2.1 Coefficients of the third-order symplectic schemes.

	c_1	c_2	c_3	d_1	d_2	d_3
Ruth (1983)	$-\frac{1}{24}$	$\frac{3}{4}$	$\frac{7}{24}$	1	$-\frac{2}{3}$	$\frac{2}{3}$
Bonomi et al. (1998)	$\frac{1}{6}$	$\frac{2}{3}$	$\frac{1}{6}$	$\frac{1}{2}$	$\frac{1}{2}$	-
Iwatsu-A (2009)	$\frac{8-\sqrt{209/2}}{12}$	$\frac{11}{12}$	$\frac{-7+\sqrt{209/2}}{12}$	$\frac{5}{9}$	$\frac{2}{9}\left(1-\sqrt{\frac{38}{11}}\right)$	$\frac{2}{9}\left(1+\sqrt{\frac{38}{11}}\right)$
Iwatsu-B (2009)	$\frac{8+\sqrt{209/2}}{12}$	$\frac{11}{12}$	$\frac{-7-\sqrt{209/2}}{12}$	$\frac{5}{9}$	$\frac{2}{9}\left(1+\sqrt{\frac{38}{11}}\right)$	$\frac{2}{9}\left(1-\sqrt{\frac{38}{11}}\right)$

2.3. Arbitrary-order symplectic time integrator

In this section, an arbitrary-order symplectic time operator is suggested. Consider the Taylor series of vector q at $t + \Delta t/2$ and $t - \Delta t/2$ with respect to t as follows:

$$\begin{aligned} q_{n+1/2} &= q_n + \frac{\Delta t}{2} q_t + \frac{\Delta t^2}{8} q_{tt} + \frac{\Delta t^3}{48} q_{ttt} + \cdots + \frac{\Delta t^k}{k!\, 2^k} q_{(k)} + \cdots \\ q_{n-1/2} &= q_n - \frac{\Delta t}{2} q_t + \frac{\Delta t^2}{8} q_{tt} - \frac{\Delta t^3}{48} q_{ttt} + \cdots + \frac{(-\Delta t)^k}{k!\, 2^k} q_{(k)} \\ &\quad + \cdots \end{aligned} \tag{2.3.1}$$

If we subtract the two equations, we obtain the expression of $q_{n+1/2}$ as follows:

$$\begin{aligned} q_{n+1/2} = q_{n-1/2} &+ \Delta t q_t + \frac{\Delta t^3}{24} q_{ttt} + \frac{\Delta t^5}{1920} q_{ttttt} + \cdots \\ &+ 2 \frac{\Delta t^{2m+1}}{(2m+1)!\, 2^{2m+1}} q_{(2m+1)} + \cdots \end{aligned} \tag{2.3.2}$$

We can obtain a similar equation of p_{n+1} by the Taylor series of vector q at $t + \Delta t$ and t with respect to $t + \Delta t/2$ as follows:

$$\begin{aligned} p_{n+1} = p_n &+ \Delta t p_t + \frac{\Delta t^3}{24} p_{ttt} + \frac{\Delta t^5}{1920} p_{ttttt} + \cdots \\ &+ 2 \frac{\Delta t^{2m+1}}{(2m+1)!\, 2^{2m+1}} p_{(2m+1)} + \cdots \end{aligned} \tag{2.3.3}$$

For (2.3.2) and (2.3.3), high-order time derivatives of p and q are required to update the variables. By replacing the time derivatives with the spatial ones, we can easily implement the high-order time marching scheme (Lax and Wendroff 1960). Via (2.1.19), we obtain the relation between the time and spatial differential operators:

$$\frac{\partial^n}{\partial t^n} y = M^n y \tag{2.3.4}$$

The power of the characteristic matrix M is

$$M = \begin{bmatrix} 0 & S_1 \\ S_2 & 0 \end{bmatrix}$$

$$M^3 = \begin{bmatrix} 0 & S_1 S_2 S_1 \\ S_2 S_1 S_2 & 0 \end{bmatrix}$$

$$M^5 = \begin{bmatrix} 0 & S_1 S_2 S_1 S_2 S_1 \\ S_2 S_1 S_2 S_1 S_2 & 0 \end{bmatrix} \tag{2.3.5}$$

$$\vdots$$

$$M^{2m-1} = \begin{bmatrix} 0 & (S_1 S_2)^m S_1 \\ (S_1 S_1)^m S_2 & 0 \end{bmatrix}$$

M and M^{2m-1} are equivalent in block structure, which enables the time marching scheme to retain the alternating nature of variable updates mentioned in the previous section. Using (2.3.5), equations (2.3.2) and (2.3.3) are reduced as follows:

$$\begin{aligned} q_{n+1/2} &= q_{n-1/2} + 2 \sum_{m=0}^{l} \frac{\Delta t^{2m+1}}{(2m+1)!\, 2^{2m+1}} (S_2 S_1)^m S_2\, p_n \\ p_{n+1} &= p_n + 2 \sum_{m=0}^{l} \frac{\Delta t^{2m+1}}{(2m+1)!\, 2^{2m+1}} (S_1 S_2)^m S_1\, q_{n+1/2} \end{aligned} \tag{2.3.6}$$

The transformation matrix of (2.3.6) is expressed in the split form of the resulting operator as follows:

$$e^{\Delta t M} \simeq e^{\Delta t M_2} e^{\Delta t M_1} \tag{2.3.7}$$

where

$$e^{\Delta t M_1} \simeq I + 2 \left(\sum_{m=0}^{l} \frac{\Delta t^{2m+1}}{(2m+1)!\, 2^{2m+1}} M^{2m+1} \right)_1 \tag{2.3.8}$$

$$e^{\Delta t M_2} \simeq I + 2\left(\sum_{m=0}^{l} \frac{\Delta t^{2m+1}}{(2m+1)!\,2^{2m+1}} M^{2m+1}\right)_2$$

Subscripts 1 and 2 are defined in the same manner as the definition of M_1 and M_2, which contains only the upper-right and lower-left submatrices, respectively. Then,

$$\overline{y}_{n+1} = e^{\Delta t M_2} e^{\Delta t M_1} \overline{y}_n \tag{2.3.9}$$

is obtained. The map satisfies the symplectic condition (2.3.7), and the approximated transformation map can be regarded as an extension of the two-stage Störmer–Verlet method in arbitrary order.

The suggested transformation operator can be calculated efficiently using the recurrence relation by defining a_m as follows:

$$2\sum_{m=0}^{l} \frac{\Delta t^{2m+1}}{(2m+1)!\,2^{2m+1}} (S_2 S_1)^m S_2\, p_n = \sum_{m=0}^{l} a_m \tag{2.3.9}$$

where

$$\begin{aligned} a_0 &= \Delta t S_2 p_n \\ a_k &= \frac{\Delta t^2}{8k(2k+1)} S_2 S_1 a_{k-1}, \quad k = 1, 2, 3, \cdots \end{aligned} \tag{2.3.10}$$

In a similar manner, we can define b_m as follows:

$$2\sum_{m=0}^{l} \frac{\Delta t^{2m+1}}{(2m+1)!\,2^{2m+1}} (S_1 S_2)^m S_1\, q_{n+1/2} = \sum_{m=0}^{l} b_m \tag{2.3.11}$$

where

$$\begin{aligned} b_0 &= \Delta t S_1 q_{n+1/2} \\ b_k &= \frac{\Delta t^2}{8k(2k+1)} S_1 S_2 b_{k-1}, \quad k = 1, 2, 3, \cdots \end{aligned} \tag{2.3.12}$$

Increasing the order of accuracy of the approximate symplectic map only

requires the repetitive calculation of the second-order spatial operators and additional memory to contain the wavefields of the previous step.

In addition, the series of the characteristic matrix can be represented as the pseudo-differential operator as follows:

$$\sum_{m=0}^{l} \frac{\Delta t^{2m+1}}{(2m+1)!\, 2^{2m+1}} M^{2m+1} = Sinh\left(\frac{\Delta t}{2} M\right) \tag{2.3.13}$$

Then, the transformation map is

$$e^{\Delta t M_2} e^{\Delta t M_1} \simeq \left(I + 2\, Sinh\left(\frac{\Delta t}{2} M\right)_2\right)\left(I + 2\, Sinh\left(\frac{\Delta t}{2} M\right)_1\right) \tag{2.3.14}$$

where subscripts 1 and 2 are defined in the same manner as the definition of M_1 and M_2, which contains only the upper-right and lower-left submatrix, respectively. By introducing the pseudo-differential operator we can use any polynomial expansion to approximate (2.3.14). For example, Tal-Ezer (1986) used the Jacobi-Anger expansion to approximate the matrix operator in the sinusoidal function

$$Sinh\left(\frac{\Delta t}{2} M\right) = 2 \sum_{m=0}^{l} J_{2m+1}\left(\frac{\Delta t}{2} R\right) Q_{2m+1}\left(\frac{M}{R}\right) \tag{2.3.15}$$

where J_m is the Bessel function of the first type and Q_m is the modified Chebyshev polynomial that satisfies the following recurrence formula as follows:

$$\begin{aligned} Q_1(w) &= w \\ Q_3(w) &= -4w^3 + 3w \end{aligned} \tag{2.3.16}$$

and

$$Q_{2m+1}(w) = 2(2w^2 + 1)Q_{2m-1}(w) - Q_{2m-3}(w) \tag{2.3.17}$$

Algorithms (2.3.16) and (2.3.17) require extra memory to contain two extra

wavefields vectors to expand. However, it is known that the convergence speed is much faster than the Taylor expansion, and a lower value of l is required to achieve an equivalent error criterion to that of equation (2.3.8).

3. Analysis

In this section, I analyze the stability and dispersion characteristics of the arbitrary-order symplectic time operator. In general, the numerical integrators that increase the time order of accuracy by the Lax-Wendroff method offer better stability properties than the normal time marching methods. I confirm that this finding holds true for the suggested algorithm by analyzing the amplification factor of the transformation map $e^{\Delta tM}$. Satisfying the symplecticity of the acoustic wave system suggests that the scheme is much more stable than explicit methods, such as the Tal-Ezer (1986) or ADER schemes (Dumbser et al. 2007), for the same order of accuracy in time. Dispersion can also be improved via arbitrary-order symplectic time operator. Stability is shown to be the necessary condition for modeling, while the dispersion criterion is a sufficient condition to achieve because the criterion of dispersion is always stricter than that of stability. In the following, I refer to the arbitrary-order symplectic time operator that expands the series n times as the 'n-th scheme.'

3.1. Stability analysis

In the previous section, I suggested the following time marching scheme, arbitrary-order symplectic time integrator formulated as equations (2.3.8) and (2.3.9). In this section, I analyze the stability of the method by applying the system of an acoustic wave (2.1.21b). The split operators are defined as follows:

$$e^{\Delta t M_1} \simeq \begin{bmatrix} 1 & 2\sum_{m=0}^{l} \frac{\Delta t^{2m+1}}{(2m+1)!\,2^{2m+1}} (\nabla^2)^m \\ 0 & 1 \end{bmatrix}$$
$$e^{\Delta t M_2} \simeq \begin{bmatrix} 1 & 0 \\ 2\sum_{m=0}^{l} \frac{\Delta t^{2m+1}}{(2m+1)!\,2^{2m+1}} (\nabla^2)^{m+1} & 1 \end{bmatrix} \tag{3.1.1}$$

The Laplacian operator ∇^2 is the spatial differential operator, which can be evaluated via several methods. The PS method is an accurate and simple way to differentiate a given function using a pair of fast Fourier transform algorithm applications (Trefethen 2000). The Laplacian operator is written as follows:

$$\nabla^2 = -\left({k_1}^2 + {k_2}^2\right) = -k^2 \tag{3.1.2}$$

where k_1 and k_2 are the wavenumbers of the x and z directions, respectively. The amplification factor of the method μ_i is equivalent to the eigenvalue of the transformation matrix λ_i. The 2-norm of the wavefield after n time steps satisfies the relation

$$\|y_n\|_2 = |\lambda_i|^n \|y_0\|_2, \quad i = 1, 2 \tag{3.1.3}$$

where y_0 is the initial value. Thus, the following should be guaranteed for the stable solution:

$$|\lambda_i| \leq 1, \quad i = 1, 2 \tag{3.1.4}$$

The determinant of the approximated transformation map is equivalent to the

product of the eigenvalues of the map

$$det(e^{\Delta t M_2} e^{\Delta t M_3}) = \prod\nolimits_{i=1,2} \lambda_i = 1 \tag{3.1.5}$$

As the main property of the symplectic transformation map is the structure preservation, the determinant of the transformation map is equal to one. This fact can also be derived from the symplectic condition (2.2.13). The physical implication of equation (3.1.5) is that the acoustic energy in the domain is conserved during the time stepping, which enables stable long-term simulation. Not only the product of the eigenvalues but also the absolute value of each eigenvalue must be equal to one. As this is the only possible way for the eigenvalues to conjugate each other, the stability of the modeling process is retained under the symplectic condition. Thus, the criterion in which the eigenvalues are conjugate complex values is the stability criterion of the symplectic time integrator. For instance, if l, the number of expansions of the pseudo-differential operator, is equal to one, the transformation map of the scheme is

$$e^{\Delta t M_2} e^{\Delta t M_3} = \begin{bmatrix} 1 & 0 \\ \Delta t - \frac{\Delta t^3}{24} c^2 k^2 & 1 \end{bmatrix} \begin{bmatrix} 1 & -\Delta t c^2 k^2 + \frac{\Delta t^3}{24} c^4 k^4 \\ 0 & 1 \end{bmatrix} \tag{3.1.6}$$

The determinant of the approximate map is one, as those of the split operator $e^{\Delta t M_2}$ and $e^{\Delta t M_3}$ are each equal to one. Two conjugate eigenvalues of (3.1.6) represent the function of $\theta = ck\Delta t$, which is proportional to the CFL number

$$\lambda_{1,2} = \frac{1}{1152}\left(1152 - 576\theta^2 + 48\theta^4 - \theta^6 \pm \sqrt{-1327104 + \left(-1152 + \theta^2(-24 + \theta^2)\right)^2}\right) \tag{3.1.7}$$

To satisfy the stability condition, the value in the root should be negative to

make the eigenvalues a complex numbers. Then, the stability of the scheme is guaranteed if $|\theta| \leq 5.694644204$.

The conventional Störmer–Verlet method, the 0th scheme, has a stability criterion of $|\theta| \leq 2$. In general, the stability criterion becomes larger as the order of accuracy of the scheme increases, which is called the CFL relaxation. This fact implies that a larger time step can be allowed for a scheme of a higher order of accuracy. The circle markers in Figure 3.1 represent the maximum θ of the arbitrary-order symplectic time integrator with respect to l, which broadly tends to increase with the number of expansion l. Because the eigenvalues are approximated with the high-order polynomial, the effect of nonlinearity occurs at some l in which the stability criterion shrinks despite the increase in l.

To confirm the effect of symplecticity, I conduct the same analysis for the numerical method with the non-symplectic time marching scheme, which can be derived by the Lax-Wendroff expansion of the central difference method as follows:

$$y_{n+1} = 2M'y_n + y_{n-1} \tag{3.1.8}$$

where

$$M' = \sum_{m=0}^{l} \frac{\Delta t^{2m+1}}{(2m+1)!\,2^{2m+1}} M^{2m+1} \tag{3.1.9}$$

The order of accuracy in time and required computational costs of the scheme (3.1.8) are equivalent to those of the symplectic scheme of the given l. The amplification factor μ_i of system (3.1.8) is:

$$\mu_i = \lambda_i \pm \sqrt{1 + {\lambda_i}^2}, \ \ i = 1, 2 \tag{3.1.10}$$

where λ_i is the eigenvalue of M'. It is well known that the scheme is stable when $|\lambda_i| < 1$. As λ_i is the function of θ, the stability criterion can also be represented with respect to the variable. The square markers in Figure 3.1 shows the stability criterion of the non-symplectic scheme with respect to l. The allowed maximum θ tends to increase with m despite some oscillations due to the nonlinearity of the eigenvalue. However the symplectic scheme has a stability region that is as much as twice as large as that of the non-symplectic method (3.1.8), which means that a much larger time step can be allowed for the symplectic time integrator which leads to the instability of the non-symplectic method.

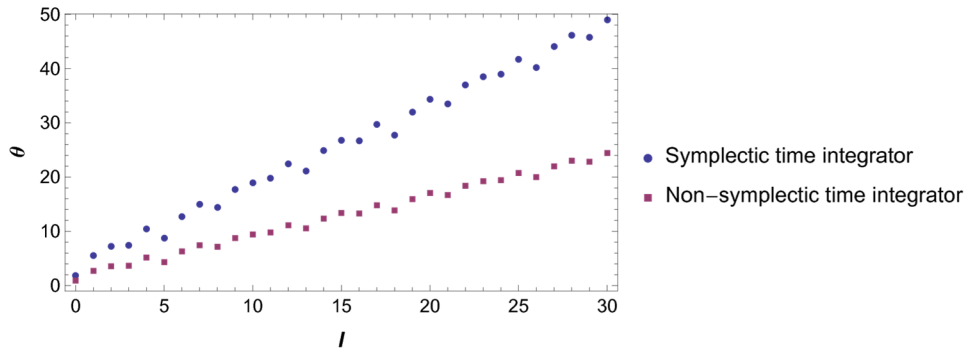

Figure 3.1 Stability criterion of the arbitrary symplectic time operator and Lax-Wendroff expansion of the central differential method.

3.2. Dispersion analysis

In this section, I conduct a dispersion analysis of the suggested scheme. The acoustic wave solution at t can be represented by separating the spatial and temporal variables as follows:

$$\overline{y}_n = \begin{bmatrix} \mathcal{R}\hat{p}(x,z) \\ \mathcal{R}\hat{q}(x,z) \end{bmatrix} e^{i\omega t} \tag{3.2.1}$$

Then, the solution at $t + \Delta t$ can be written as

$$\overline{y}_{n+1} = \begin{bmatrix} \mathcal{R}\hat{f}(x,z) \\ \mathcal{R}\hat{g}(x,z) \end{bmatrix} e^{i\omega(t+\Delta t)} \tag{3.2.2}$$

which is equivalent to the extrapolation of the solution at t with $e^{i\omega\Delta t}$ at the entire domain of interest as follows:

$$\overline{y}_{n+1} = e^{i\omega\Delta t}\,\overline{y}_n = e^{\Delta t M_2} e^{\Delta t M_1}\,\overline{y}_n \tag{3.2.3}$$

If we recall the time-stepping algorithm (2.3.9), the eigenvalue of the system λ_i acts as the analytic time extrapolation factor $e^{i\omega\Delta t}$, the complex number that has a unit length as noted in the previous section. The exact change of phase of the wave solutions during Δt is $\omega\Delta t$, which we pursue by expanding the operator $e^{\Delta t M_2} e^{\Delta t M_1}$ with the Lax-Wendroff or Jacobi-Anger expansion. We find that the angular frequency of the acoustic wave ω can be approximated by ω', and the phase change of the wavefield by the numerical modeling is $\omega'\Delta t$. The following is an argument of λ_i

$$\omega\Delta t \simeq \omega'\Delta t = Arg(\lambda_i) = \tan^{-1}\left(\frac{Im(\lambda_i)}{Re(\lambda_i)}\right) \tag{3.2.4}$$

where ω' is the approximated angular frequency

$$\omega' = \frac{1}{\Delta t}\tan^{-1}\left(\frac{Im(\lambda_i)}{Re(\lambda_i)}\right) \tag{3.2.5}$$

The phase velocity is derived as follows:

$$c_{phase} = \frac{\omega'}{k} = \frac{1}{k\Delta t}\tan^{-1}\left(\frac{Im(\lambda_i)}{Re(\lambda_i)}\right) \tag{3.2.6}$$

The phase velocity is typically normalized by the real velocity value as follows:

$$\frac{c_{phase}}{c} = \frac{1}{\theta}\tan^{-1}\left(\frac{Im(\lambda_i(\theta))}{Re(\lambda_i(\theta))}\right) \tag{3.2.7}$$

In the ideal case, the normalized phase velocity is one, which means that there is no error between the analytic phase change and that of the numerical calculation result during Δt. The eigenvalue is a function of θ, i.e., $ck\Delta t$, as shown in the previous section. If the grid size in each spatial direction is equivalent, θ can be rewritten as

$$\theta = ck\Delta t = c\frac{2\pi}{\zeta}\Delta t = \frac{2\pi}{G}\frac{c\Delta t}{h} = \frac{2\pi}{G}\gamma \tag{3.2.8}$$

where ζ is the wavelength, h is the grid size, γ is the CFL number, and G is the number of grids per wavelength. Then, the normalized phase velocity can be represented as a function of G and γ as follows:

$$\frac{c_{phase}}{c} = \frac{G}{2\pi\gamma}\tan^{-1}\left(\frac{Im\left(\lambda_i\left(\frac{2\pi}{G}\gamma\right)\right)}{Re\left(\lambda_i\left(\frac{2\pi}{G}\gamma\right)\right)}\right) \tag{3.2.9}$$

Figure 3.2 shows the normalized phase velocity error, $\frac{c_{phase}}{c} - 1$, of the zeroth, first, second, and third schemes with respect to $1/G$ for several γ values below 1.25. The normalized phase velocity error decreases dramatically as the order of the scheme increases. The error is almost negligible for the second and third schemes with low γ values of 0.25 or 0.5, even for the Nyquist sampling rate in the spatial domain, i.e., $1/G$ is 0.5. This means the simulation under

the condition yields a wavefield almost identical to the analytically derived solution, which might be deemed as the method with spectral accuracy. A deeper analysis of the spectral accuracy is presented in section 3.1.4.

The group velocity of the wave denotes the velocity of the wave packet or envelope of the wave propagating in the media. It is derived by differentiating the approximated angular frequency with wavenumber k as follows:

$$c_{group} = \frac{\partial \omega'}{\partial k} = \frac{1}{\Delta t}\frac{\partial}{\partial k}\left(\tan^{-1}\left(\frac{Im(\lambda_i)}{Re(\lambda_i)}\right)\right) \tag{3.2.10}$$

Then, the normalized group velocity is also derived as follows:

$$\frac{c_{group}}{c} = \frac{1}{c\Delta t}\frac{\partial}{\partial k}\left(\tan^{-1}\left(\frac{Im(\lambda_i)}{Re(\lambda_i)}\right)\right) \tag{3.2.11}$$

Because the λ_i is a function of θ, (3.2.10) can be represented as follows:

$$\frac{c_{group}}{c} = \frac{\partial}{\partial \theta}\left(\tan^{-1}\left(\frac{Im(\lambda_i(\theta))}{Re(\lambda_i(\theta))}\right)\right) \tag{3.2.12}$$

which can also be rewritten as a function of G and γ using equation (3.2.8). Figure 3.3 presents the normalized group velocity error, $\frac{c_{group}}{c} - 1$, of the zeroth, first, second, and third schemes, with respect to $1/G$ for the same set of γ as Figure 3.3. The normalized group velocity error is confirmed to be larger than that of the normalized phase velocity. However, the scale of the error is almost equivalent to that of the phase velocity, which can be regarded as negligible for the second or third schemes. In the previous section, it was confirmed that the stability criterion is relaxed as the order of the scheme increases, and much larger γ values can be used. Figure 3.4 and Figure 3.5 show the normalized phase and group velocity errors for γ inside the stability

criterion delineated in Figure 3.1. The error curves show that the error increases sharply as γ approaches the stability criterion.

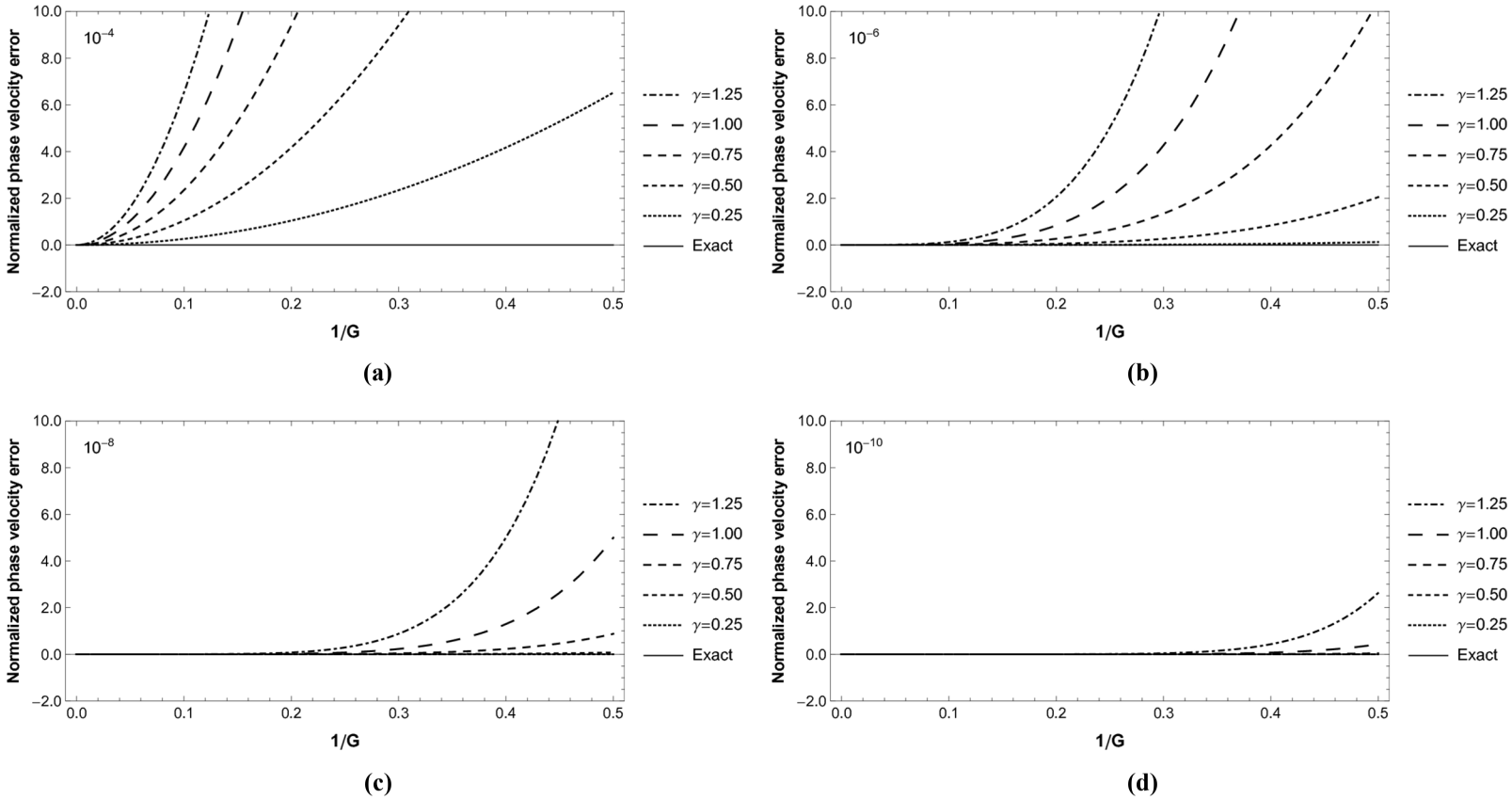

Figure 3.2 Normalized phase velocity error of the zeroth (a), first (b), second (c) and fourth schemes (d) of low CFL numbers.

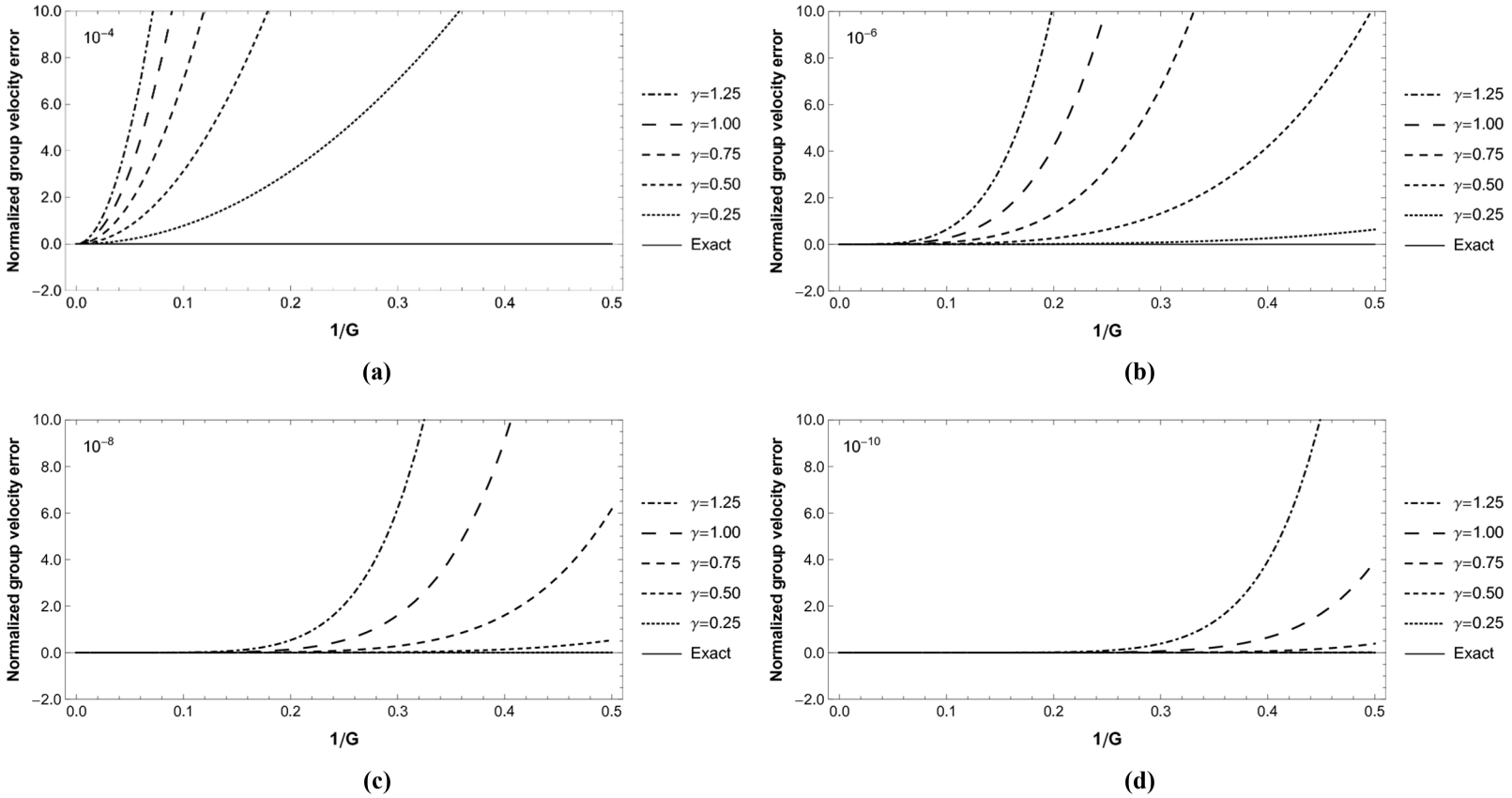

Figure 3.3 Normalized group velocity error of the zeroth (a), first (b), second (c) and fourth schemes (d) of low CFL numbers.

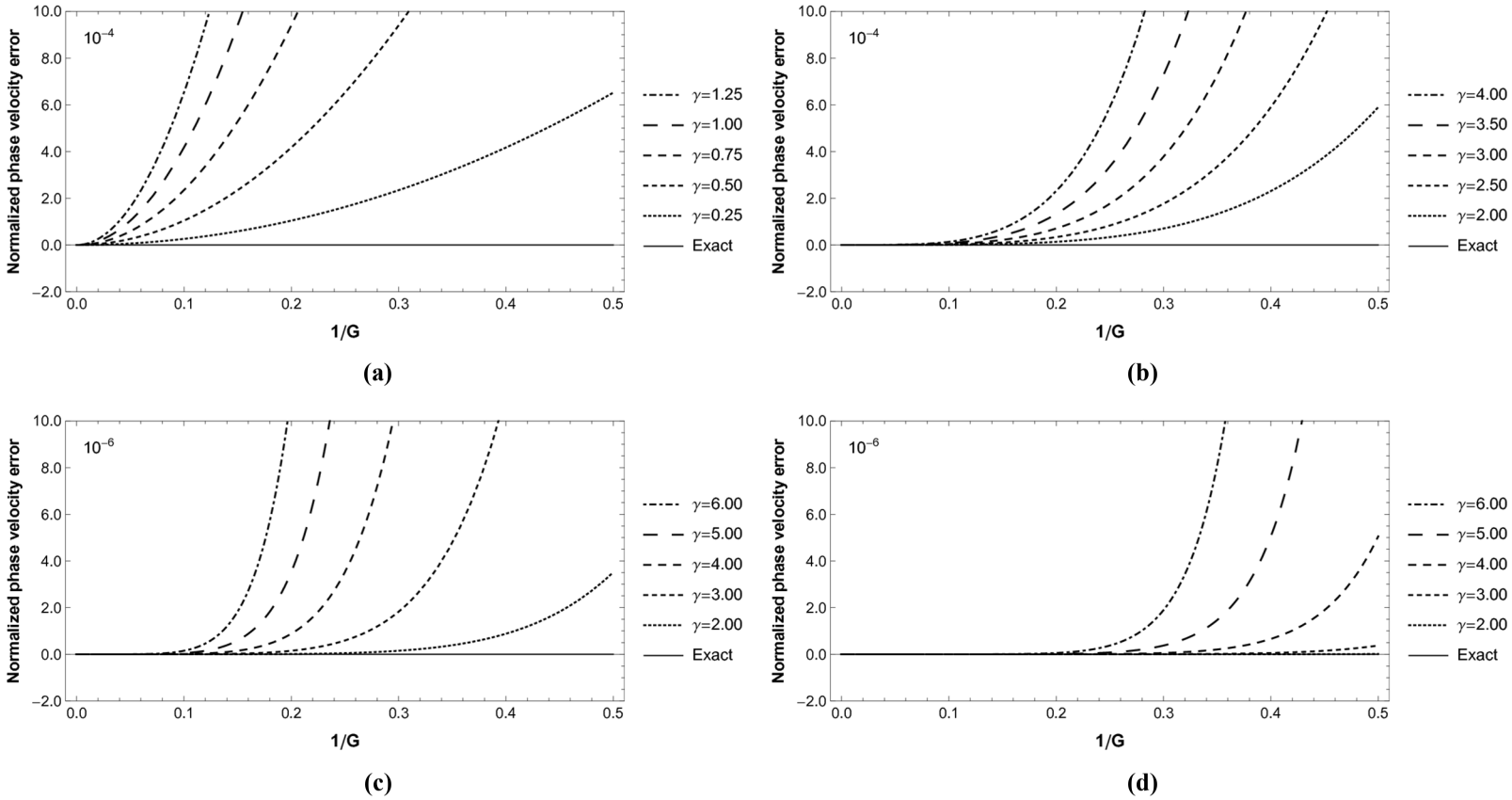

Figure 3.4 Normalized phase velocity error of the zeroth (a), first (b), second (c) and fourth schemes (d) of high CFL numbers.

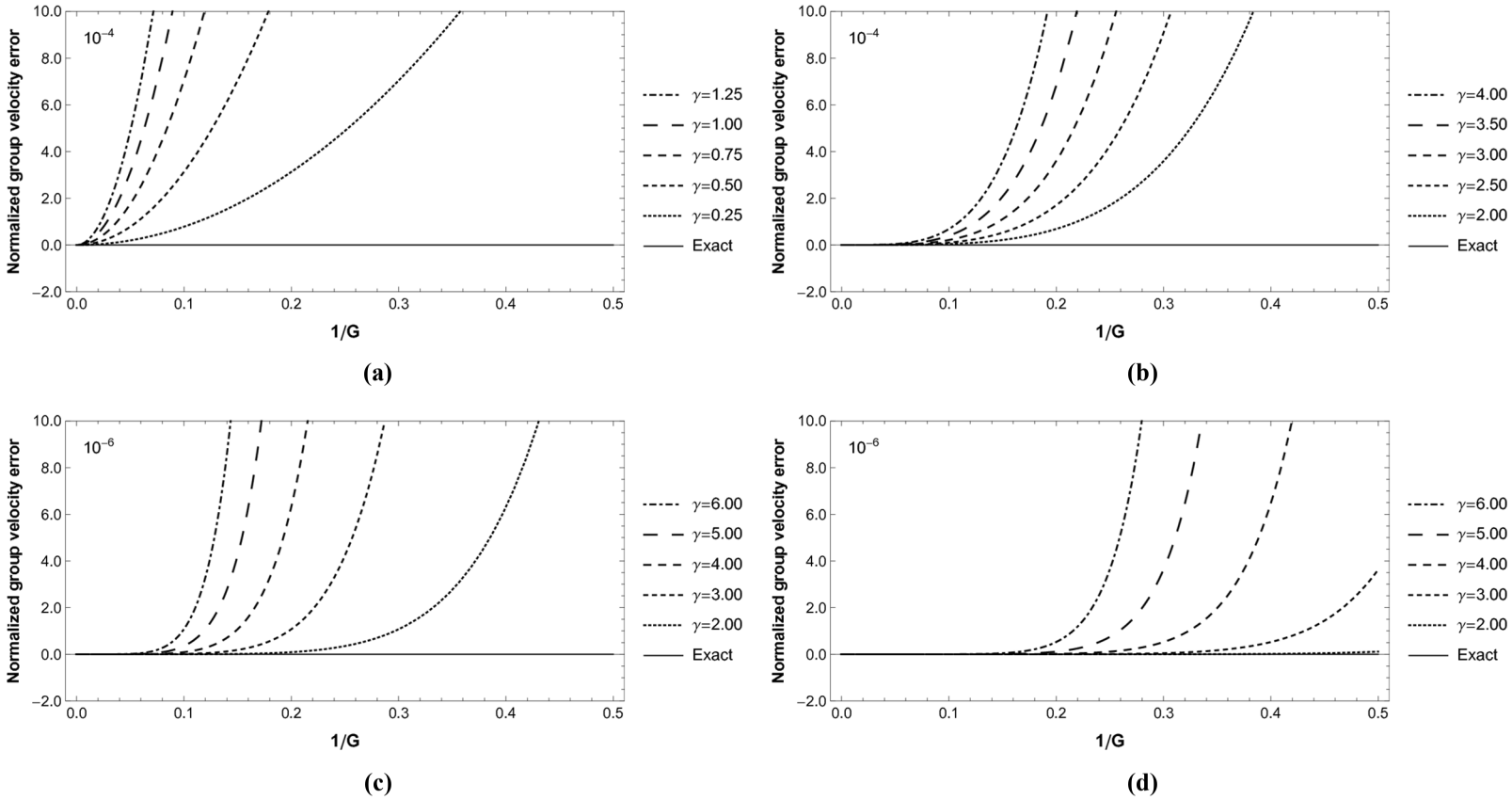

Figure 3.5 Normalized group velocity error of the zeroth (a), first (b), second (c) and fourth schemes (d) of high CFL numbers.

3.3. Phase analysis

In this section, I conduct a phase error analysis of the suggested time marching scheme. The objective of the analysis is not different from that of the dispersion or group velocity error analysis. The point of this section is to estimate the error of the numerical modeling with respect to the phase of the wavefield and then determine the time step length and the number of time steps satisfying the phase error criterion.

Again, I start the analysis from the eigenvalue of the approximated transformation matrix, λ_i. As noted in section 3.1, each eigenvalue of the symplectic map has a unit length due to its condition (2.2.13), which means that the symplectic scheme is free from dissipation error. Thus, it is sufficient to analyze the phase error. Recall the relation of the change of phase and λ_i

$$\omega\Delta t \simeq \omega'\Delta t = Arg(\lambda_i) = \tan^{-1}\left(\frac{Im(\lambda_i)}{Re(\lambda_i)}\right) \tag{3.3.1}$$

For example, recall the eigenvalues of the symplectic map of the first scheme

$$\lambda_{1,2} = \frac{1}{1152}\left(1152 - 576\theta^2 + 48\theta^4 - \theta^6 \pm \mathbb{i}\sqrt{1327104 - \left(-1152 + \theta^2(-24 + \theta^2)\right)^2}\right) \tag{3.3.2}$$

The phase change after one time step $\omega\Delta t$ equals θ as $\omega = ck$, and the phase shift of the numerical scheme is approximated as follows:

$$\theta \simeq \tan^{-1}\left(\frac{1152 - 576\theta^2 + 48\theta^4 - \theta^6}{\sqrt{1327104 - \left(-1152 + \theta^2(-24 + \theta^2)\right)^2}}\right) \tag{3.3.3}$$

The arctangent function can be rewritten as a polynomial series by Taylor series

expansion as follows:

$$\tan^{-1}\left(\frac{1152-576\theta^2+48\theta^4-\theta^6}{\sqrt{1327104-\left(-1152+\theta^2(-24+\theta^2)\right)^2}}\right) \simeq \theta+\frac{\theta^5}{1920}+O(\theta^7) \tag{3.3.4}$$

Equation (3.3.4) indicates that the phase change error per time step $\Delta\theta$ is $\theta^5/120$ and the total phase change error ψ after t is calculated as follows:

$$\psi=\frac{t}{\Delta t}\Delta\theta=\frac{t}{\Delta t}\frac{\theta^5}{1920}=\frac{tc^5k^5}{120}\Delta t^4+O(\Delta t^6) \tag{3.3.5}$$

The error depends on k, and the maximum error $\Delta\theta_{max}$ occurs at higher wavenumbers as follows:

$$\begin{aligned}\psi_{max}&=\frac{tc^5{k_{max}}^5}{1920}\Delta t^4\\&=\frac{1}{1920}t\pi^5c^5\Delta t^4\left(\sqrt{\frac{1}{\Delta x^2}+\frac{1}{\Delta z^2}}\right)^5+O(\Delta t^6)\end{aligned} \tag{3.3.6}$$

If $\psi_{max}=\pi$ at t, the phase of the wavefield is opposite the analytic wavefield. Thus, it is reasonable to set ψ_{max} to be less than π. Once ψ_{max} is set, the following inequality is expected to be satisfied

$$\psi_{max}>\frac{1}{1920}t\pi^5c^5\Delta t^4\left(\sqrt{\frac{1}{\Delta x^2}+\frac{1}{\Delta z^2}}\right)^5 \tag{3.3.7}$$

In addition, N_t, the minimum number of time steps to reach t, is derived using the relation $\Delta t=t/N_t$

$$N_t > \left(\frac{{\psi_{max}}^{-1}}{1920}\right)^{\frac{1}{4}} \left(\pi ct\sqrt{\frac{1}{\Delta x^2}+\frac{1}{\Delta z^2}}\right)^{\frac{5}{4}} \tag{3.3.8}$$

For instance, if we perform the modeling until $t = 10s$ using the third scheme in the computational domain of the grid size of each dimension with $\Delta x = \Delta z = 10m$ and the maximum p-wave velocity of the model is $5km/s$, N_t should be larger than 10750 so that the ψ_{max} is less than $\pi/10$. Then, Δt needs to be smaller than $0.9ms$.

The total phase change error of the arbitrary l-th scheme after t is also calculated as follows:

$$\psi = \frac{t}{\Delta t}\frac{\theta^{2l+2}}{4^{l+1}(2l+3)!} + O\left(\Delta t^{2l+1}\right) \tag{3.3.7}$$

and the minimum time step N_t necessary for the phase change error of the wavefield at t to be less than ψ_{max} is

$$N_t = \left(\frac{{\psi_{max}}^{-1}}{4^{l+1}(2l+3)!}\right)^{\frac{1}{2l+2}} \left(\pi ct\sqrt{\frac{1}{\Delta x^2}+\frac{1}{\Delta z^2}}\right)^{\frac{2l+3}{2l+2}}, l = 0, 1, 2 \ \ldots \tag{3.3.8}$$

It is natural that $\Delta\theta$ is proportional to the normalized phase velocity error addressed in the previous section, and this methodology enables the design of the optimal modeling configuration under the given circumstances. The total computational cost depends on the total number of multiplications of the symplectic map N_{mat}, which can be derived by equation (3.3.8) as follows:

$$N_{mat} = (2l+1)\left(\frac{{\psi_{max}}^{-1}}{4^{l+1}(2l+3)!}\right)^{\frac{1}{2l+2}} \left(\pi ct\sqrt{\frac{1}{\Delta x^2}+\frac{1}{\Delta z^2}}\right)^{\frac{2l+3}{2l+2}} \tag{3.3.9}$$

Note that N_{mat} decreases as the expansion number m increases if $\frac{k_{max}}{\psi_{max}}$ is

sufficiently large. This implies that if we wish to obtain accurate wavefields with high resolution, it is more effective to conduct numerical simulation using a higher-order scheme with a larger time step length than that using a lower-order scheme with small time steps. For instance, if $c_{max} = 5$km/s, $\Delta x = \Delta z = 0.01$ km, $t = 20$ s and $\psi_{max} = 0.01$, then $\frac{k_{max}}{\psi_{max}} = 4.4 \times 10^6$ and N_{mat} with respect to l decreases rapidly to a certain level as illustrated in Figure 3.6, which supports the implication of equation (3.3.9). N_t and Δt can also be calculated using equation (3.3.8) and dividing t by N_t with respect to l. Figure 3.7 represents the Δt under the modeling conditions above and it shows that $\psi_{max} = 0.01$ is an excessively strict tolerance because the order of Δt is 10^{-6}s, i.e., 0.001ms, for the zeroth scheme and 10^{-4}s, i.e., 0.1ms, for the second to fourth schemes. Then, we can calculate θ under the given condition (Figure 3.8) which enables us to estimate the error between the analytic eigenvalue and that of the approximate transformation matrix. Table 3.1 shows that the length of the eigenvalue error remains under the order of 10^{-4} for each l from zero to thirty, which indicates that the simulation is sufficiently accurate if ψ_{max} is confined to less than 0.01.

In addition, the non-symplectic time discretization method expressed as equation (3.1.8) is also analyzed to compare the computational efficiency in terms of N_{mat} and Δt. The total phase change error of the arbitrary l-th scheme after t of equation (3.1.8) is also calculated as follows:

$$\psi = \frac{t}{\Delta t}\frac{\theta^{2l+2}}{(2l+3)!} + O\left(\Delta t^{2l+1}\right) \tag{3.3.10}$$

Then, the minimum number of time steps N_t necessary for ψ to be less than

ψ_{max} is

$$N_t = \left(\frac{{\psi_{max}}^{-1}}{(2l+3)!}\right)^{\frac{1}{2l+2}} \left(\pi c t \sqrt{\frac{1}{\Delta x^2} + \frac{1}{\Delta z^2}}\right)^{\frac{2l+3}{2l+2}}, l = 0, 1, 2 \ \ldots \qquad (3.3.11)$$

From equation (3.3.11), it is possible to determine the Δt under the given restriction. The total number of multiplications of the characteristic matrix N_{mat} for equation (3.1.8) is

$$N_{mat} = (2l+1)\left(\frac{{\psi_{max}}^{-1}}{(2l+3)!}\right)^{\frac{1}{2l+2}} \left(\pi c t \sqrt{\frac{1}{\Delta x^2} + \frac{1}{\Delta z^2}}\right)^{\frac{2l+3}{2l+2}} \qquad (3.3.12)$$

Figure 3.9 illustrates Δt with respect to the expansion number l for the non-symplectic scheme as equation (3.1.8) (purple square markers) with that of the arbitrary-order symplectic time operator (blue circle markers), which satisfies ψ_{max} to be less than 0.01 under the modeling geometries of $\mathrm{c}_{max} = 5$km/s, $\Delta x = \Delta z = 0.01$km, and $t = 20$s. Δt for the non-symplectic scheme is half of that of the arbitrary-order symplectic time integrator; N_{mat} of the non-symplectic scheme is exactly twice that of the symplectic scheme as shown in Figure 3.10. The results imply that considering symplecticity can considerably improve both the dispersion characteristic and the stability (Figure 3.1) under equivalent modeling conditions.

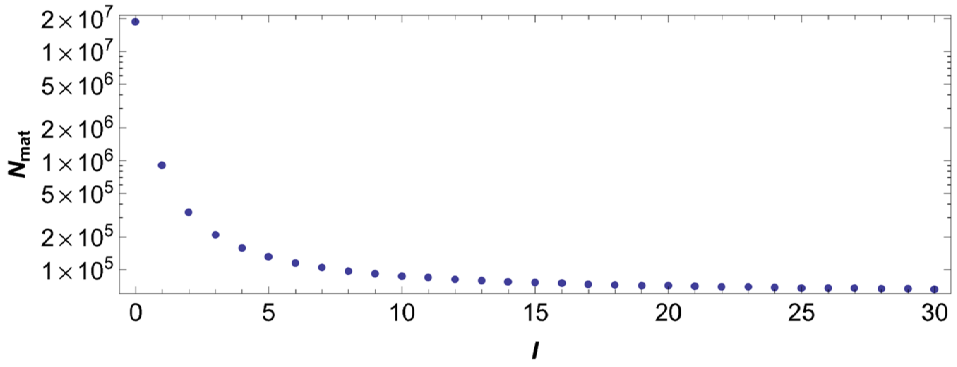

Figure 3.6 Total number of multiplications of the symplectic map to achieve a phase error of less than 0.01 after 20s with respect to the number of expansions of the smplectic map if $\mathbf{c_{max}} = \mathbf{5km/s}$, $\Delta x = \Delta z = \mathbf{0.01km}$, and $t = \mathbf{20s}$.

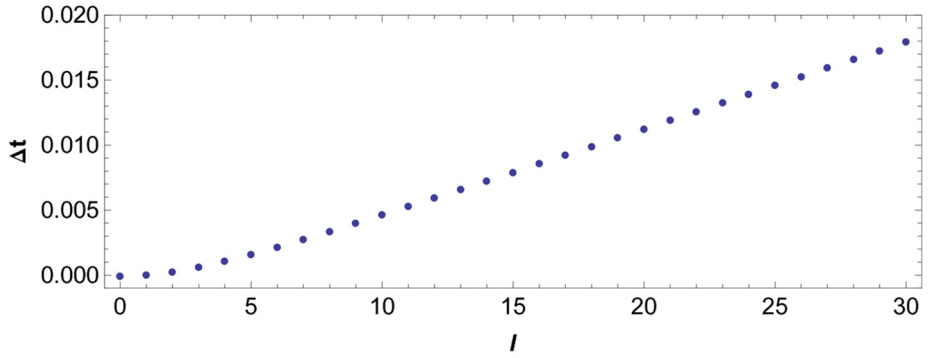

Figure 3.7 Time step length to achieve a phase error of less than 0.01 after 20s with respect to the number of expansions of the smplectic map if $c_{max} = 5$km/s, $\Delta x = \Delta z = 0.01$km, and $t = 20$s.

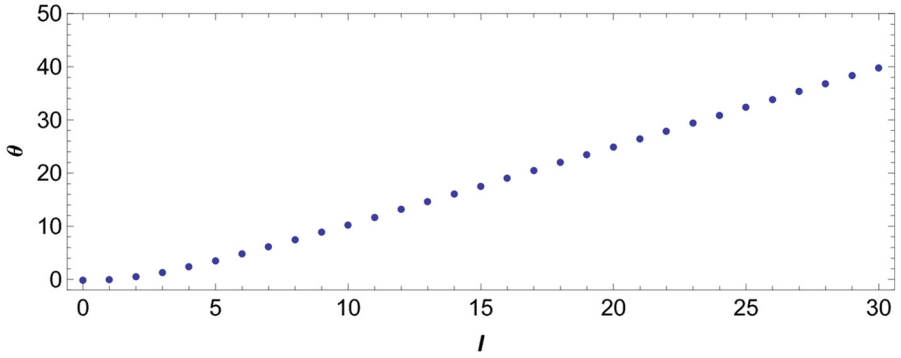

Figure 3.8 Phase change per time step to achieve a phase error of less than 0.01 after 20s with respect to the number of expansions of smplectic map if $c_{max} = 5$km/s, $\Delta x = \Delta z = 0.01$km, and $t = 20$s.

Table 3.1 The error of the analytic eigenvalue and that of the approximate map to achieve a phase error of less than 0.01 after 20s with respect to the number of expansions of the smplectic map if $\mathbf{c}_{max} = \mathbf{5km/s}$, $\Delta\mathbf{x} = \Delta\mathbf{z} = \mathbf{0.01km}$, and $\mathbf{t} = \mathbf{20s}$.

$\boldsymbol{l}$	0	1	2	3	4	5	6	7	8	9	10
$\lvert\Delta\boldsymbol{\lambda}\rvert$	5.23e-10	3.25e-8	1.53e-7	4.40e-7	1.74e-7	3.17e-6	1.40e-6	1.37e-6	2.09e-6	9.16e-6	4.72 e-6
$\boldsymbol{l}$	11	12	13	14	15	16	17	18	19	20	21
$\lvert\Delta\boldsymbol{\lambda}\rvert$	2.71 e-6	3.04 e-6	6.82 e-6	1.37 e-5	4.47 e-6	4.08 e-6	6.92 e-6	7.25 e-5	6.84 e-6	5.23 e-6	7.35 e-6
$\boldsymbol{l}$	22	23	24	25	26	27	28	29	30	-	-
$\lvert\Delta\boldsymbol{\lambda}\rvert$	5.46 e-5	1.03 e-5	6.34 e-6	7.91 e-6	2.63 e-5	1.60 e-5	8.11 e-6	8.58 e-6	1.97 e-5	-	-

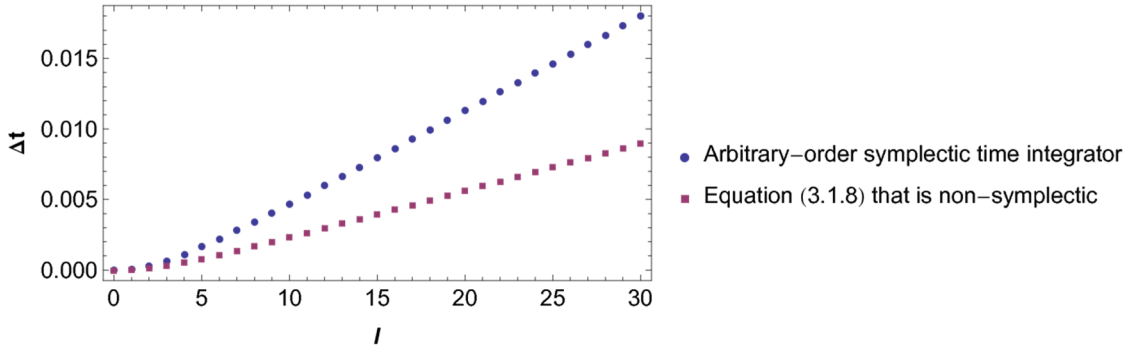

Figure 3.9 Comparison of the Δt of the arbitrary-order symplectic time integrator to the non-symplectic scheme to achieve a phase error of less than 0.01 after 20s with respect to the number of expansions of the smplectic map if $c_{max} = 5$km/s, $\Delta x = \Delta z = 0.01$km, and $t = 20$s.

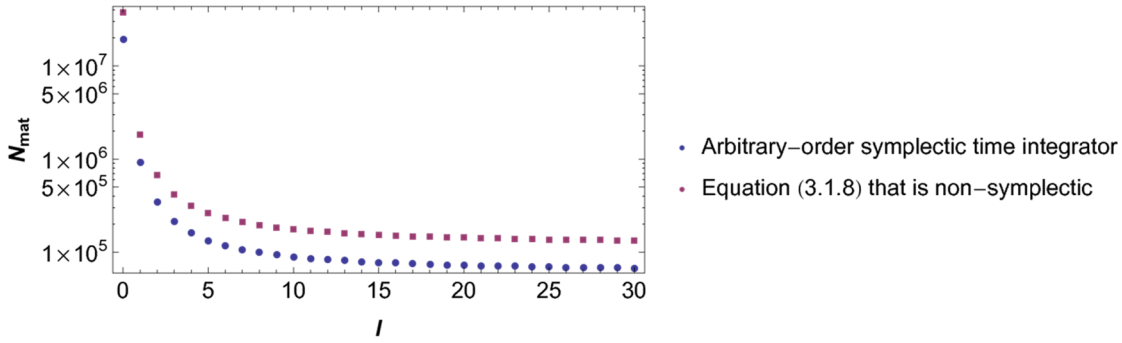

Figure 3.10 Comparison of the N_{mat} of the arbitrary-order symplectic time integrator to the non-symplectic scheme to achieve a phase error of less than 0.01 after 20s with respect to the number of expansions of the smplectic map if $c_{max} = 5$km/s, $\Delta x = \Delta z = 0.01$km, and $t = 20$s.

3.4. Spectral accuracy and compromise

The objective of this section is to suggest a strategy to attain not only high accuracy but also efficiency using the arbitrary-order symplectic time integrator. If the result of numerical simulation achieves spectral accuracy, then the numerical solution is highly accurate for both the spatial and temporal dimensions such that the wavefields in the spectral domain almost correspond to the theoretical solution. Because I use the PS method, any spatial errors arise not from the discretization of the computational domain, but instead from the time marching. Thus, spectral accuracy can be easily achieved using the arbitrary-order symplectic time integrator merely by increasing the order of accuracy in the time domain, as shown in Figure 3.2. As noted in section 2.3, the approximated symplectic map can be represented as equation (2.3.14), which is expanded recursively by the Jacobi-Anger expansion, the series of the product of the Bessel function of the first type $J_k(x)$ and the modified Chebyshev function $Q_k(x)$ formulated as equation (2.3.15). Tal-Ezer (1986) noted that the series converges to be negligible and the asymptotic behavior of the numerical result starts from l; the number of expansions of the map reaches $c_{max}k_{max}\Delta t$. This implies that the numerical simulation result can be regarded as within spectral accuracy if the number of the series expansion l satisfies

$$l \geq \theta_{max} \ (= c_{max}k_{max}\Delta t) \tag{3.4.2}$$

This criterion holds true for the Taylor series expansion such that the phase error of the scheme converges to zero at $l = \theta$. Accurate as the result may be, a high computational cost is incurred when expanding the series. The eigenvalue error is negligibly small for any l under the modeling condition of

$c_{max} = 5\text{km/s}$, $\Delta x = \Delta z = 0.01\text{km}$, and $t = 20\text{s}$, which is represented by Table 3.2. The phase error per time step, i.e., $\Delta\theta$ can also be calculated, which has the equivalent order to the eigenvalue error as shown by Table 3.3. $\Delta\theta$ approaches zero as l increases; the order of $\Delta\theta$ is 10^{-14}, which means that the simulation results are excessively accurate in that the maximum phase error theoretically reaches one percent after 10^{12} time steps. Thus, a tradeoff technique is required to ensure the efficiency of the modeling.

In section 3.3, I quantified the phase change error of the numerical result with respect to modeling configurations, i.e. p-wave velocity, grid length, and factors needed to be designed such as the number of expansion l and tolerance of phase change error $\Delta\theta$ and recording time t. In general, as the number of total time steps is larger than 10000, it is reasonable to set $\Delta\theta$ to be less than 0.0001 for the total phase error to be less than 1. Then, we can find the minimum θ that satisfies

$$|\Delta\theta| = \left|\cos^{-1}\left(\text{Re}\left(\lambda_i(\theta)\right)\right) - \cos^{-1}(\cos\theta)\right| \leq 10^{-4} \qquad (3.4.3)$$

for each scheme. Alternatively, merely finding θ_e, the minimum θ that satisfies

$$|\Delta\text{Re}(\lambda)| = \left|\text{Re}\left(\lambda_i(\theta)\right) - \cos\theta\right| \leq 10^{-4} \qquad (3.4.4)$$

produces almost equivalent results. Figure 3.11, 3.12, 3.13 and 3.14 depict curves of $\cos\theta$, $\text{Re}\left(\lambda_i(\theta)\right)$ and its difference of even-order schemes from zero to fourteenth. $\text{Re}\left(\lambda_i(\theta)\right)$ approaches $\cos\theta$ for large θ, which means that the scheme yields accurate solutions for larger time steps as the order of the scheme increases. Figure 3.15 illustrates θ_e for each scheme from the

zeroth to thirtieth by the purple square marker. The relation of θ and l satisfying the spectral accuracy is plotted with the olive diamond marker. Figure 3.15 convinces us that the strategy that follows the compromised method can reduce the computational costs of performing the simulation because the required number of expansions is smaller than that of the scheme that follows equation (3.4.2). For instance, if the maximum θ calculated by the modeling geometry is 20, l should be 20 to achieve spectral accuracy, but should be 16 according to the blue marker that ensures that $\Delta\theta$ is less than 10^{-4}.

In addition, θ_e can be rewritten by the modeling geometries as follows:

$$\theta_e(l) = ck\Delta t = ck\frac{t_{max}}{N_t} \tag{3.4.5}$$

Then, the total number of time steps is

$$N_t = ck\frac{t_{max}}{\theta_e(l)} \tag{3.4.6}$$

The total number of matrix multiplications can be written as follows:

$$N_{mat} = (2l+1)\frac{ckt_{max}}{\theta_e(l)} \tag{3.4.7}$$

Figure 3.16(a) illustrates N_{mat}, i.e., computational cost, with respect to l from zero to thirty, which is normalized by the N_{mat} of the zeroth scheme. The figure shows that it is more effective to perform numerical simulation using a higher-order scheme with a larger time step length, as noted in the previous section. Figure 3.16(b) represents the inverse of the normalized N_{mat}, i.e., computational speed. This implies that numerical simulation using higher-order schemes increases the speed by almost 4.5 times faster compared with the speed using zeroth order with small a time stride length.

Table 3.2 The error of the analytic eigenvalue and that of the approximate map with respect to the number of expansions of the smplectic map when satisfying equaion (3.4.2).

l	0	1	2	3	4	5	6	7	8	9	10
$\lvert\Delta\lambda\rvert$	0	5.90e-4	7.25e-4	2.91e-3	2.40e-4	5.80e-4	2.15e-5	1.03e-5	6.66e-6	9.31e-6	3.12e-6
l	11	12	13	14	15	16	17	18	19	20	21
$\lvert\Delta\lambda\rvert$	5.63e-7	1.87e-7	8.32e-8	4.86e-8	4.86e-8	4.78e-8	5.15e-8	5.63e-9	1.68e-9	6.97e-10	3.75e-10
l	22	23	24	25	26	27	28	29	30	31	32
$\lvert\Delta\lambda\rvert$	3.01e-10	1.47e-8	6.09e-11	1.58e-11	6.09e-12	3.05e-12	2.11e-12	4.19e-22	7.34e-13	1.56e-13	5.53e-14

Table 3.3 $\Delta\theta$ of the arbitrary-order symplectic time operator with respect to the number of expansions of the smplectic map when satisfying equaion (3.4.2).

l	0	1	2	3	4	5	6	7	8	9	10
$\lvert\Delta\theta\rvert$	0	5.90e-4	7.25e-4	2.91e-3	2.42e-4	5.80e-5	2.15e-5	1.03e-5	6.66e-6	9.31e-6	3.12e-6
l	11	12	13	14	15	16	17	18	19	20	21
$\lvert\Delta\theta\rvert$	5.63e-7	1.87e-7	8.32e-8	4.86e-8	4.77e-8	5.15e-8	5.63e-9	1.68e-9	6.97e-10	3.75e-10	3.01e-10
l	22	23	24	25	26	27	28	29	30	31	32
$\lvert\Delta\theta\rvert$	1.47e-8	6.09e-11	1.59e-11	6.10e-12	3.05e-12	2.12e-12	4.19e-12	7.33e-13	1.57e-13	5.40e-14	2.70e-14

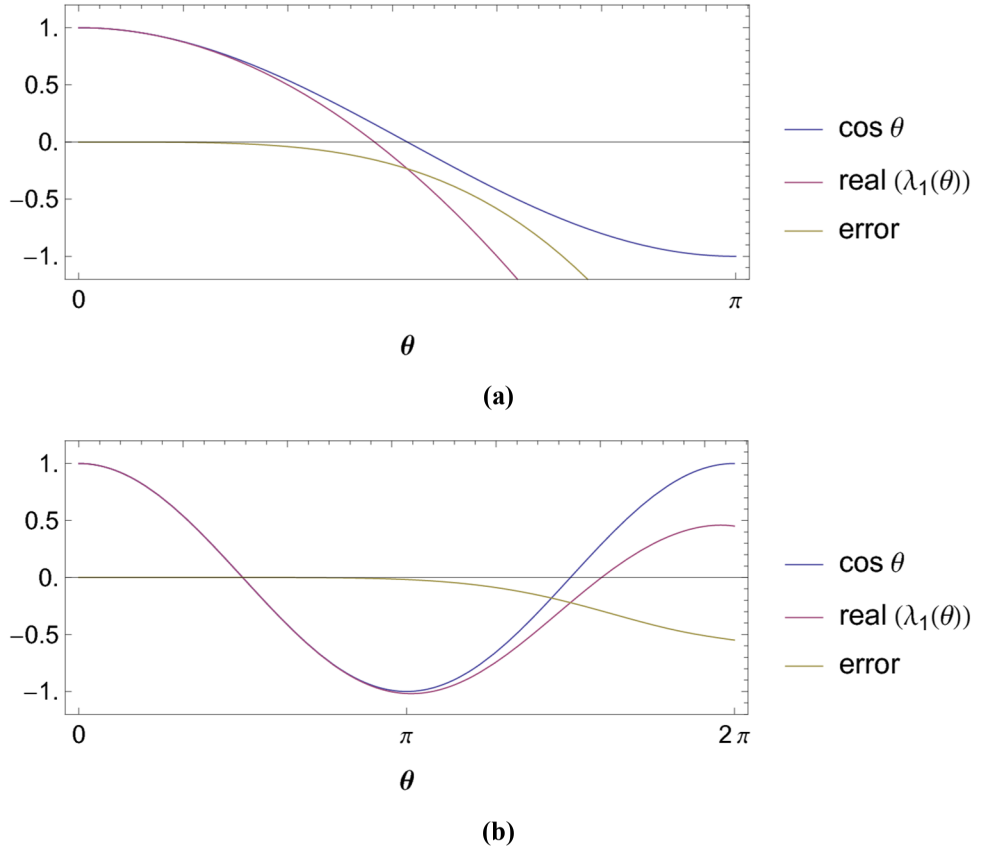

Figure 3.11 Real part of the analytic and approximated eigenvalue and its error of the zeroth (a) and second schemes (b).

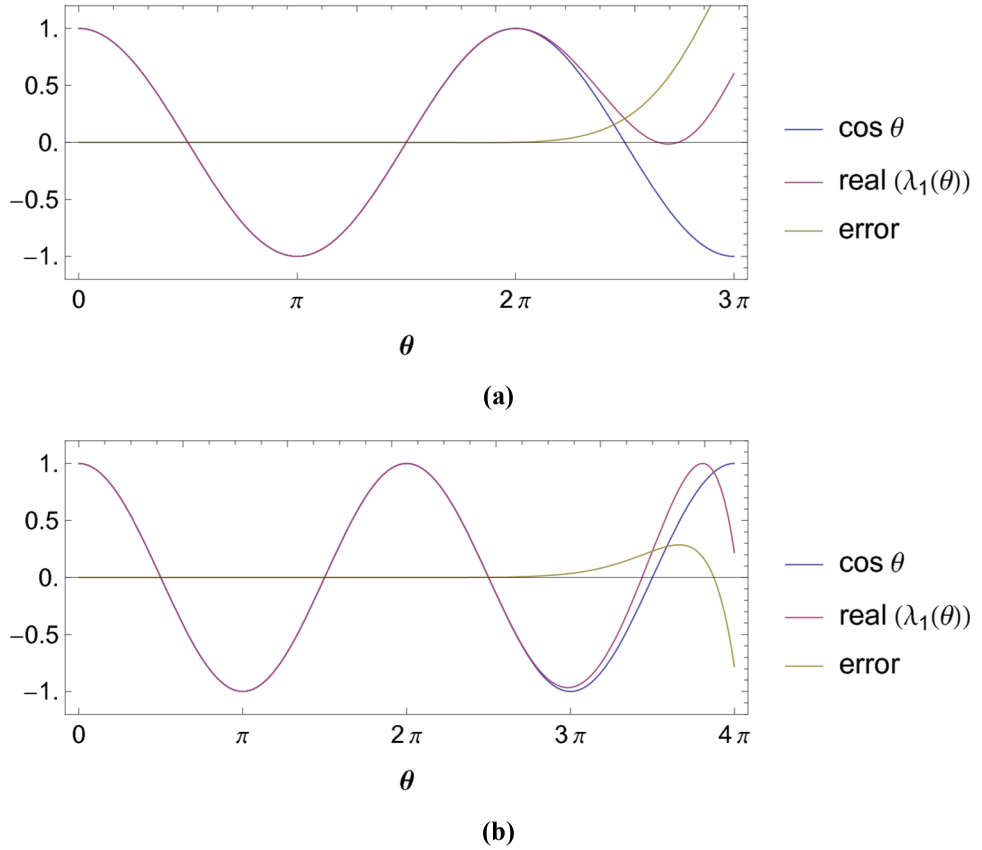

Figure 3.12 Real part of the analytic and approximated eigenvalue and its error of the fourth (a) and sixth schemes (b).

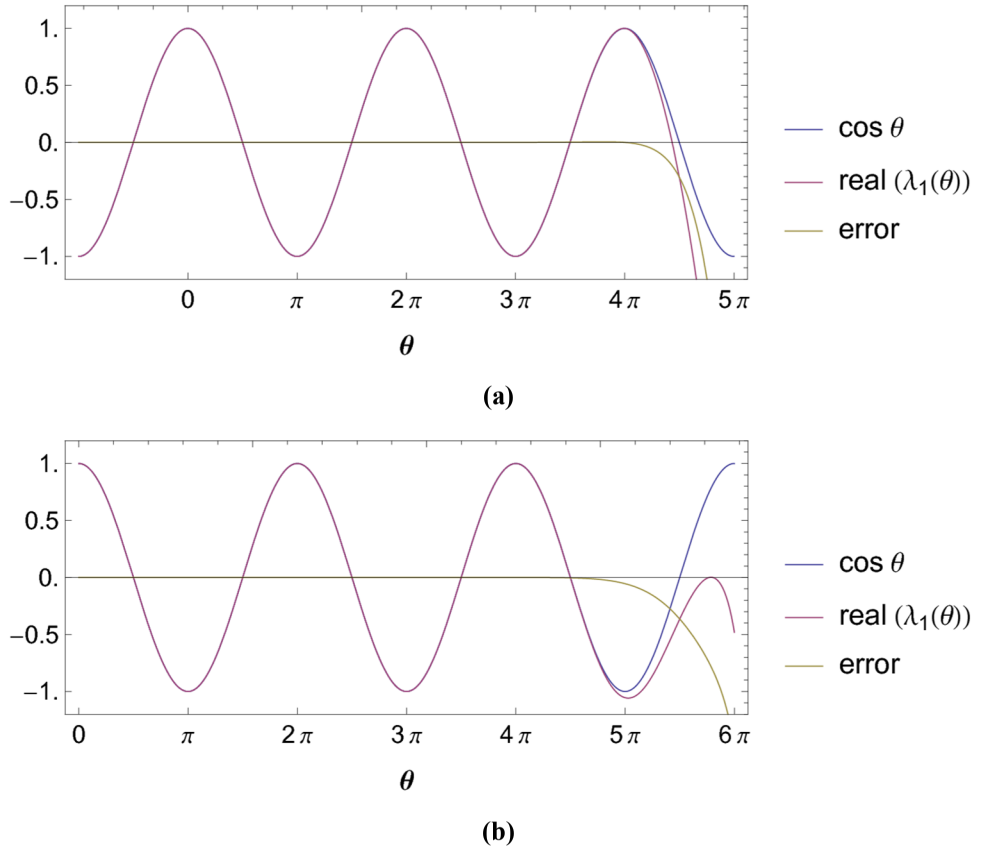

Figure 3.13 Real part of the analytic and approximated eigenvalue and its error of the eighth (a) and tenth schemes (b).

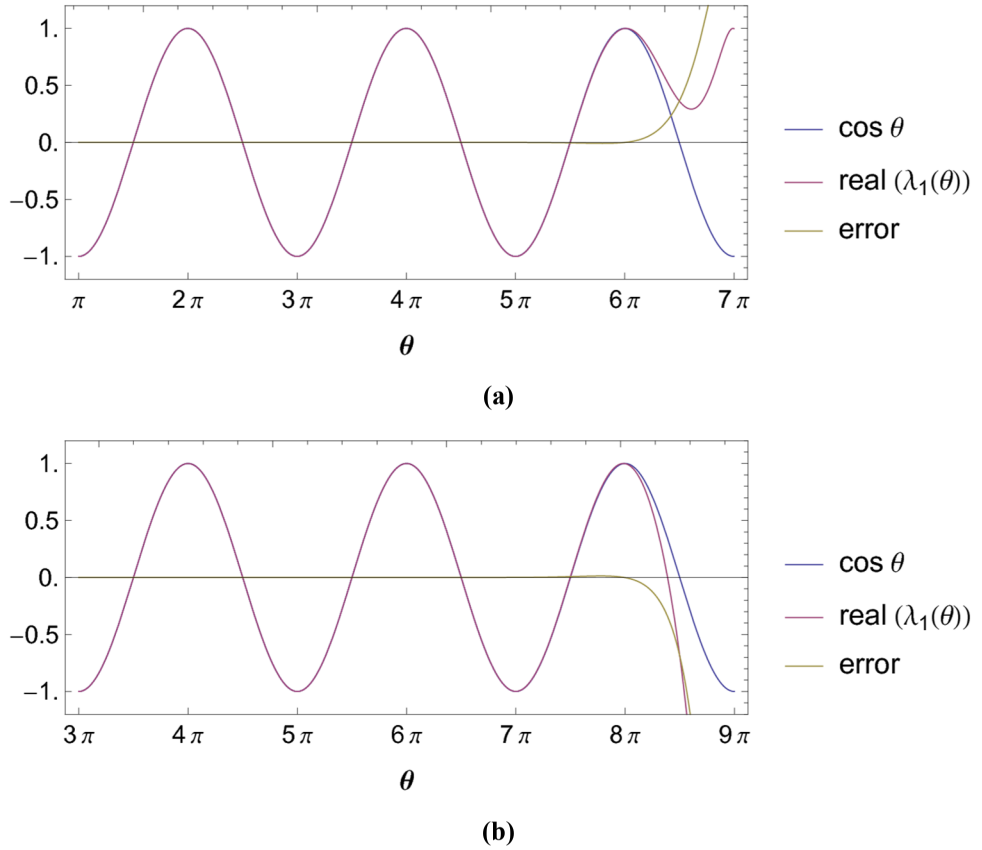

Figure 3.14 Real part of the analytic and approximated eigenvalue and its error of the twelfth (a) and fourteenth schemes (b).

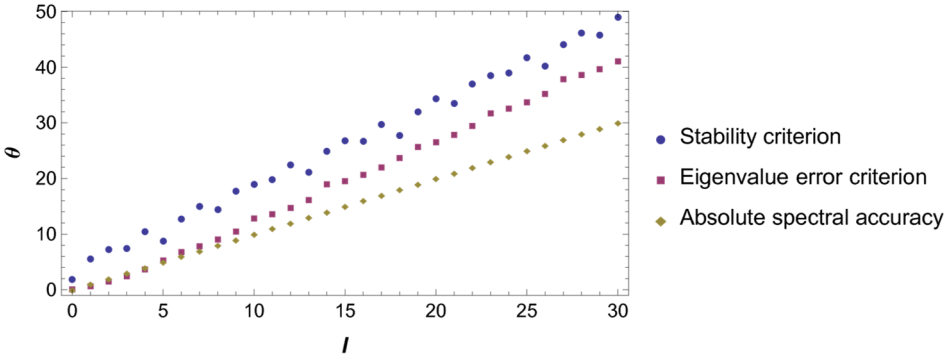

Figure 3.15 θ_e with respect to l (purple square) within the stability criterion (blue circle) and the relation that guarantees absolute accuracy (olive diamond).

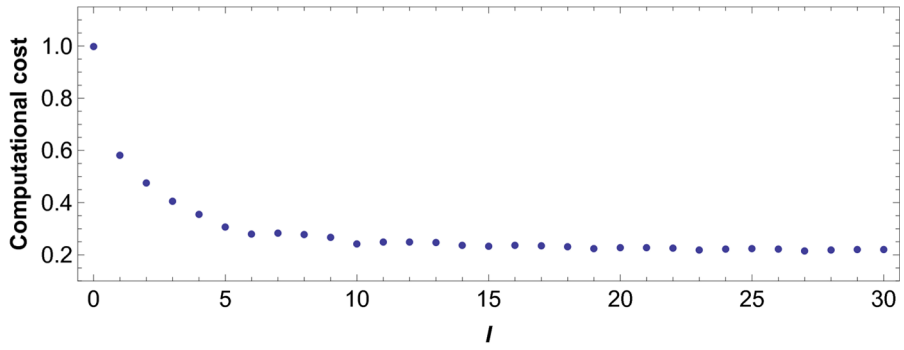

(a)

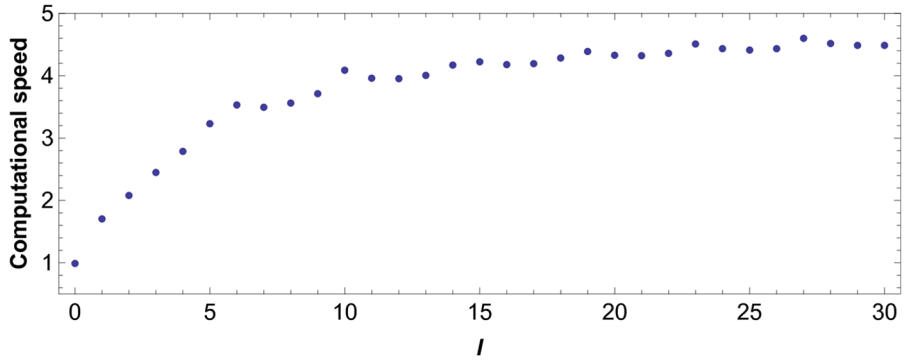

(b)

Figure 3.16 Relative total computational cost over recorded time (a) and computational speed (b) with respect to l.

3.5. Source wavelet issue

These long, representative characteristics of the arbitrary-order symplectic time integrator are analyzed using the initial value problem of the PDE. In this section, I discuss important issues regarding the effects of the source wavelet on modeling configuration designs, i.e., grid size, time step length, and the order of the scheme.

In fact, the conventional method to impose the source wavelet is imperfect. If we consider the inhomogeneous solution of the acoustic wave equation

$$\frac{\partial}{\partial t} y = My + q \tag{3.5.1}$$

where q is the input vector, i.e., a source wavelet, then the analytic solution is represented as follows:

$$y(t) = e^{tM} y_0 + e^{tM} * q \tag{3.5.2}$$

If the simulation is started from the state of tranquility, the convolutional term is the solution of the system. However, the convolutional term is cumbersome to calculate, and only a single source problem can be solved by this expression, which cannot be applied to the adjoint modeling process in the majority of applications, such as imaging or inverse problems. To solve this problem, Pestana and Stoffa (2010) convert the source problem to the discretized initial value problems with impulsive source signals at the source points. This approach requires the time step length to be confined to a certain level. In addition, the source wavelet is the design factor for controlling the resolution of the image via RTM. Thus, fine discretization on the time axis is required to guarantee high-resolution results, which may devalue the main advantage of the

suggested scheme that allow a large time step length.

As explained in the previous section, the quality of the modeling result is controlled by the number of expansions l to the given phase change per time step θ of the modeling geometry. Thus, we first need to determine maximum θ that is produced. When we set the maximum frequency component of the source wavelet as the Nyquist frequency, f_{max}, the maximum allowable time step length Δt_{max} is

$$\Delta t_{max} = \frac{1}{2f_{max}} \tag{3.5.3}$$

Otherwise, the modeling result is inaccurate due to aliasing, which may reduce the effectiveness of the scheme. Δt_{max} is not a sufficient condition but is a necessary condition for the reliable result of the source problem. This implies that the result can be inaccurate under certain modeling conditions, such as high p-wave velocity models.

The next thing to consider is the determination of l, which is the number of expansions of the symplectic map to satisfy a level of quality that we set. The describable maximum k_{max} depends on the grid sizes as follows:

$$k_{max} = \sqrt{{k_{x,max}}^2 + {k_{z,max}}^2} = \pi \sqrt{\frac{1}{{h_x}^2} + \frac{1}{{h_z}^2}} \tag{3.5.4}$$

where h_x and h_z are the grid size of the computational domain. Thus, the maximum θ is written as follows:

$$\theta_{max} = c_{max} k_{max} \Delta t_{max} = \frac{\pi c_{max}}{2f_{max}} \sqrt{\frac{1}{{h_x}^2} + \frac{1}{{h_z}^2}} \tag{3.5.5}$$

Then, it is possible to determine l as the nearest large integer of θ_{max} to

ensure the spectral accuracy or corresponding value to achieve $\Delta\theta \simeq 10^{-4}$ using the relation illustrated in Figure 3.15.

In addition, it is necessary to design the maximum grid size h of the domain to avoid degrading the result of the modeling. The acoustic wavefield at any position is governed by the dispersion relation as follows:

$$k = \frac{\omega}{c} \tag{3.5.6}$$

where ω is the angular frequency of the wavefield. If the wave is generated by external sources imposed on the media, the frequency of the wave depends on that of the wavelet of the source imposed on the isotropic media without dispersion or dissipation. Then, the maximum wavenumber due to the source signature is

$$k_s = \frac{2\pi f_{max}}{c_{min}} \tag{3.5.7}$$

which should be equal to or less than k_{max}. Then, the grid size should satisfy

$$h \leq \frac{c_{min}}{\sqrt{2} f_{max}} \tag{3.5.8}$$

if $h_x = h_z = h$.

4. Numerical Examples

In this section, numerical examples of the arbitrary-order symplectic time integrator are presented to verify the properties of the schemes explained in the analysis section. First, the numerical results of the initial value problem in homogeneous media are introduced with the periodic boundary condition naturally imposed on the PS method using the fast Fourier transform to calculate spatial differentiation terms. Several time steps are used to confirm the relaxation nature of the scheme this is of a high order in time. The accuracy of each result is compared to the analytic solution of the initial value problem. Next, source problems are dealt with separately. In this case, the pretty good sponge boundary invented by Lavelle and Thacker (2007) is applied.

4.1. Initial value problems

4.1.1. Homogeneous model

The initial value problem is conducted using a $4\pi \times 4\pi$ km^2 computational domain composed of 512 equally spaced grid points with a grid length of 0.2454 km for each spatial dimension. I use the p-wave velocity model with a homogeneous 5 km/s to make the modeling geometry sufficiently severe for θ to be large. For the initial value, I impose a Gaussian profile of $e^{-\alpha r^2}$, where α equals 80 and r is the distance from the center of the computational domain. For the numerical simulation, four different Δt values are used (1 ms, 10 ms, 20 ms, and 40 ms) to yield an acoustic wavefield over 20 s. Table 4.1 represents the maximum θ, the order of the scheme required by l to maintain the phase error within 10^{-4}, the number of total time steps N_t, and the number of total multiplication steps of the characteristic matrix N_{mat} for each case of Δt. As θ increases with Δt, a higher-order scheme is required to accommodate θ. As we know the total number of time steps, we can calculate the total number of matrix multiplication steps. We can confirm that the scheme using a higher order with large Δt is more efficient in terms of N_{mat}. The computational cost of wave simulation with 4ms is less than a quarter of that with $1ms$. Although the ratio of the total number of operator multiplication steps approaches one, which implies that the efficiency of modeling is not improved dramatically as Δt or θ increases, N_{mat} decreases at all events. The wavefield at 5 s, 10 s, 15 s and 20 s is illustrated in Figure 4.1(b), 4.2(b), 4.3(b) and 4.4(b), respectively, with results of different Δt values shown at each quadrant. These

figures can be compared to the analytic wavefield solution at the same point depicted in Figure 4.1(a), 4.2(a), 4.3(a) and 4.4(a), respectively. The wavefield results are notably equivalent to the analytic solutions in terms of the scale and location of the events. The L2 error of the wavefield is calculated at the time points as shown in Table 4.2; the error is negligibly small. It is also confirmed that phase lead or lag does not occur even for the result of a large time step of 20 ms at 20 s. This finding is also shown by the time traces illustrated in Figure 4.5, 4.6, 4.7 and 4.8 and at four different receiver positions at (0.074, 0.049), (2.352, 0.049), (3.92, 0.049) and (5.488, 0.049), respectively. The figures show that the events are synchronized without any dispersive errors separated from the main events.

4.1.2. Synthetic heterogeneous model: Marmousi-2

Numerical simulation of the acoustic wavefield in the heterogeneous model is now performed. The purpose of this test is to confirm the feasibility of the scheme for the transformation map of heterogeneous media. The Marmousi-2 model is used for the simulation, which is illustrated in Figure 4.9. The model is 17 km long and 3.5 km deep with a grid size of 12.5 m. The maximum and minimum p-wave velocities are 4.7 km/s and 1.028 km/s, respectively. The Gaussian profile $e^{-\alpha r^2}$, where α equals 80 and r is the distance from the center of the computational domain, is imposed as the initial value. Similarly, for the initial value problem of the homogeneous model, 1 ms, 10 ms, 20 ms and 40 ms are used as the time step lengths. The θ for each Δt and l required to achieve a phase change error per time step less than 10^{-4} is shown

in Table 4.3. The total number of operator multiplications decreases as expected. Time traces are recorded at the four receiver points, (1.0625, 0.025), (3.1875, 0.025), (5.3125, 0.025) and (7.4375, 0.025); Figure 4.10, 4.11, 4.12, and 4.13 illustrate the traces at each receiver. Again, the figures show that all events are synchronized without any dispersive errors separated from the main events.

Table 4.1 The phase change per time step θ, required l, total number of time steps and total number of multiplications of the operator with respect to each time step length of the simulation using a homogeneous model with a 24.5m grid space.

Δt	1ms	10ms	20ms	40ms
θ	0.905	9.051	18.102	36.204
l	2	8	14	27
N_t	20000	2000	1000	500
N_{mat}	100000	34000	29000	28000
CPU time (s)	5829.62	2097.18	1786.56	1667.06

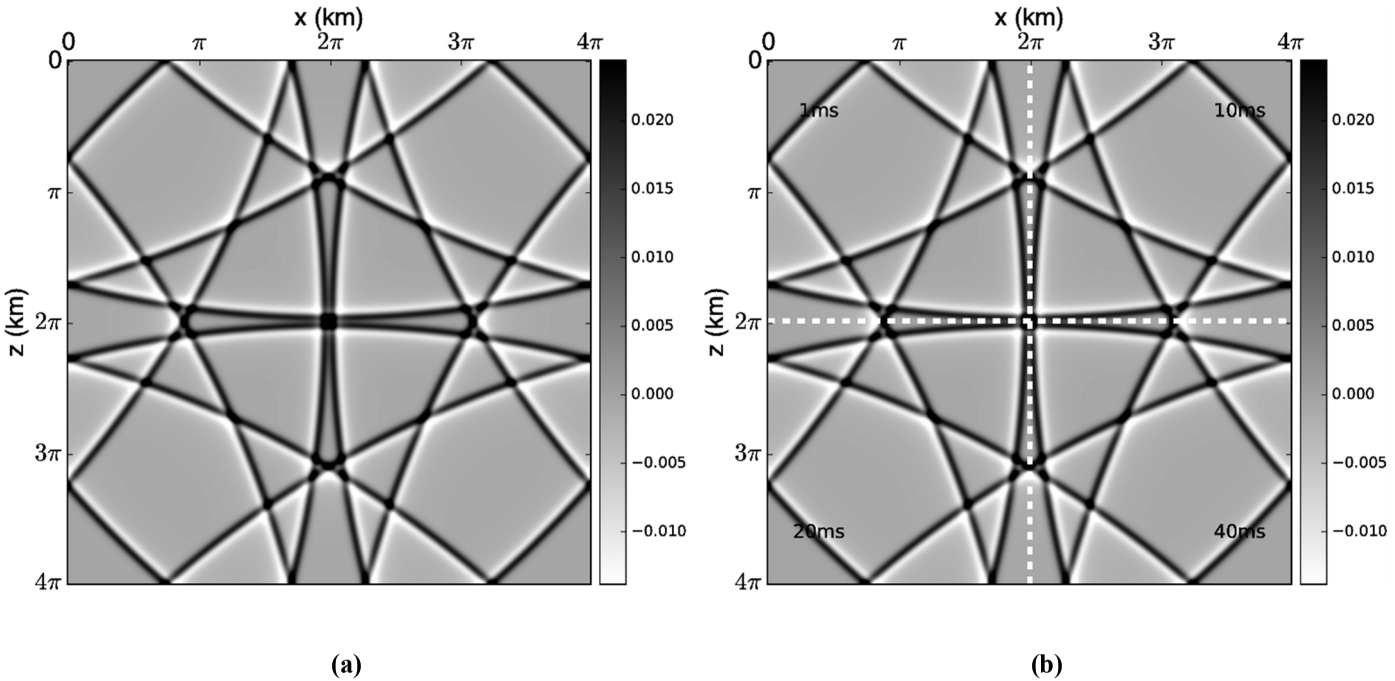

Figure 4.1 Analytic solution (a) and numerical results of each time step length (b) at 5 s.

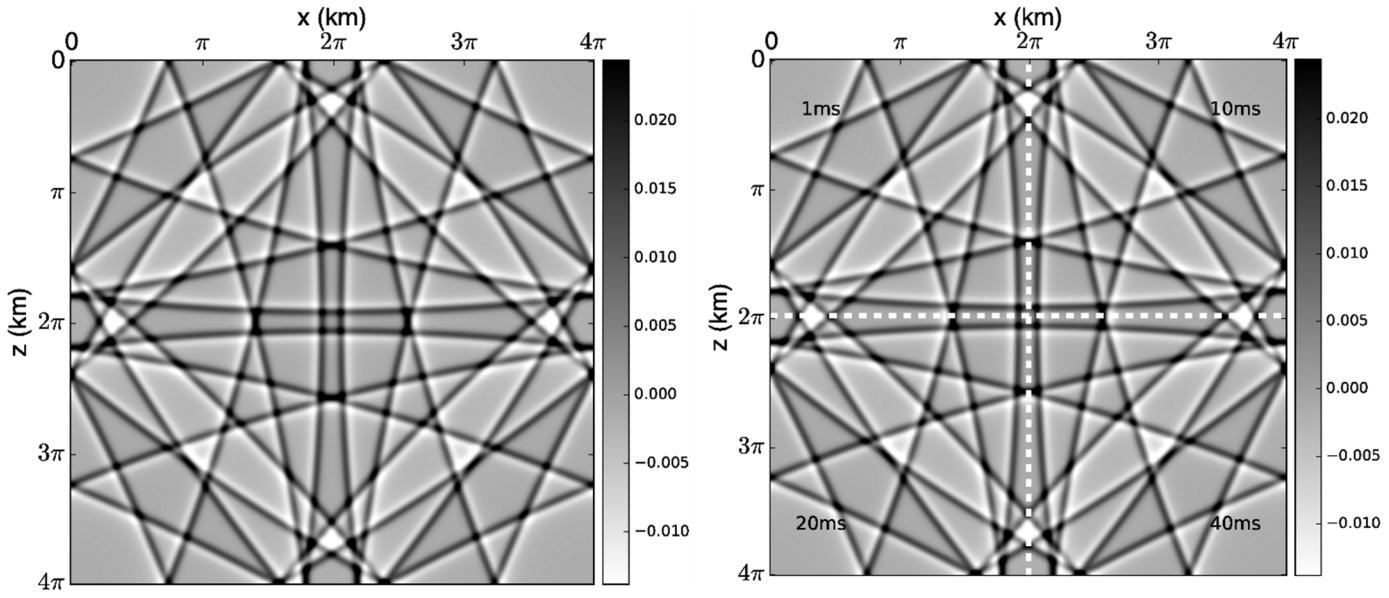

Figure 4.2 Analytic solution (a) and numerical results of each time step length (b) at 10 s.

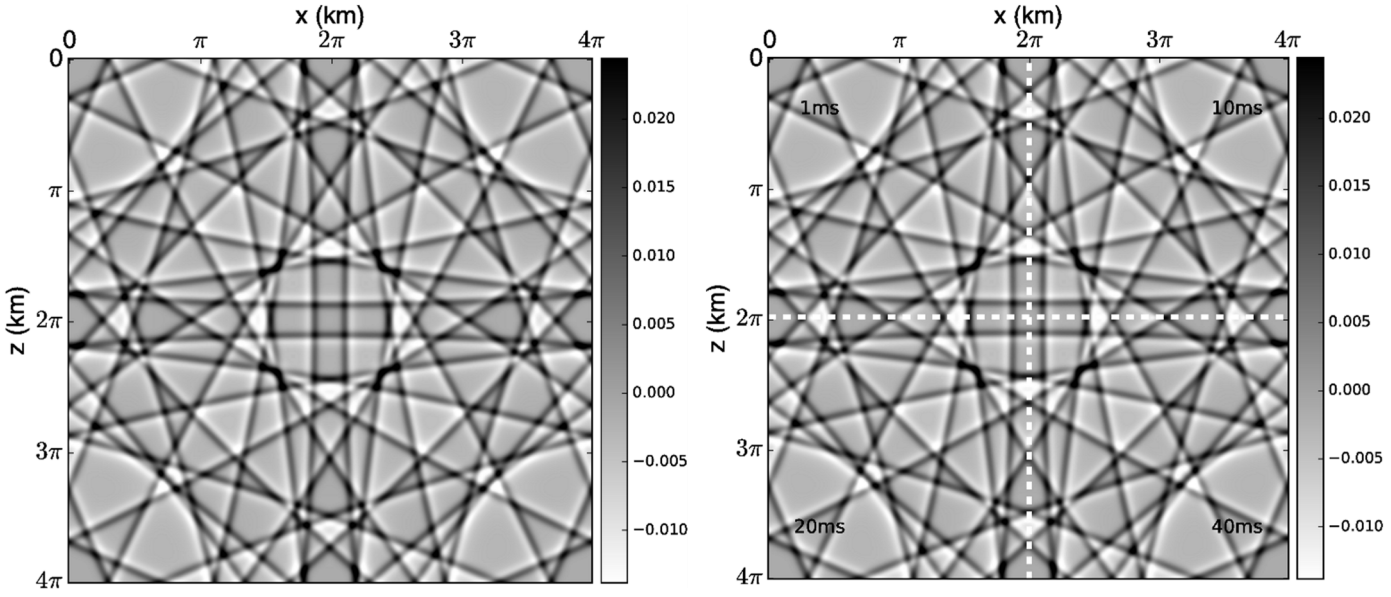

Figure 4.3 Analytic solution (a) and numerical results of each time step length (b) at 15 s.

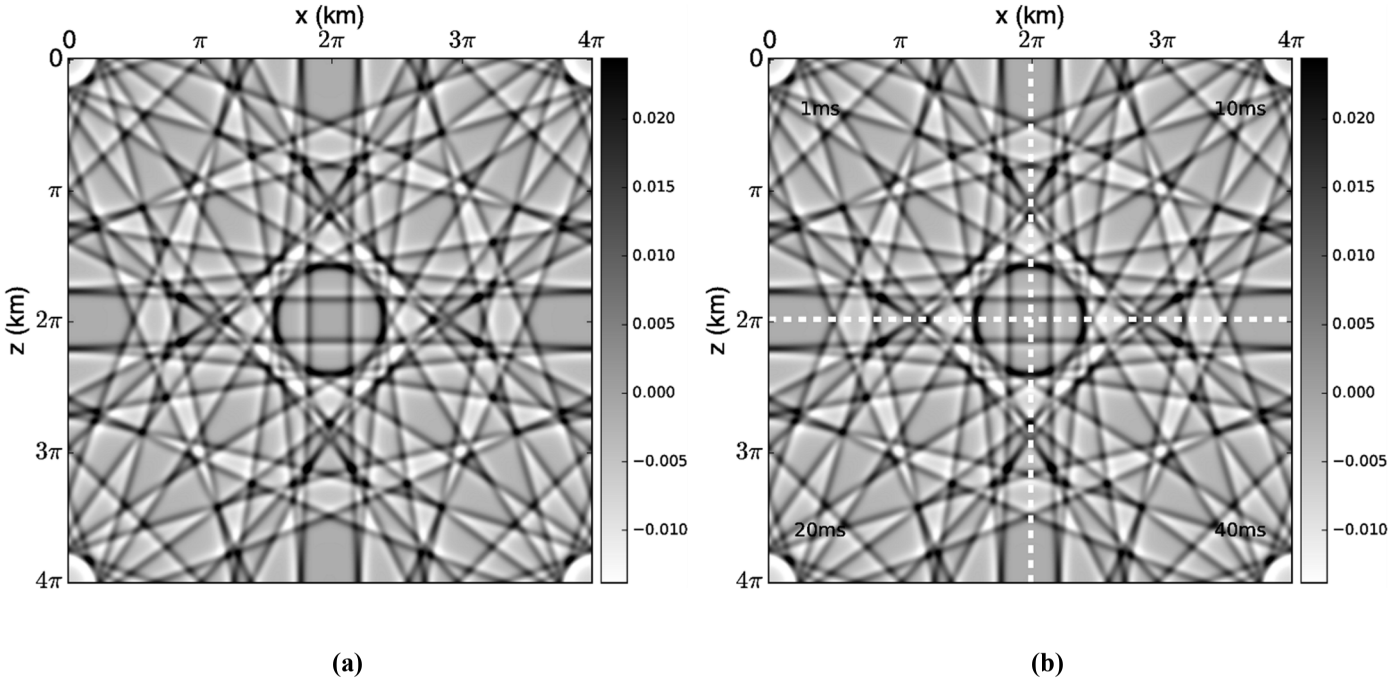

Figure 4.4 Analytic solution (a) and numerical results of each time step length (b) at 20 s.

Table 4.2 L2 norm of the error of the wavefield at 5 s, 10 s, 15 s and 20 s.

Δt	5 s	10 s	15 s	20 s
L2 error (1ms)	6.81e-8	9.55e-8	1.14e-7	1.30e-7
L2 error (10ms)	2.19e-9	9.09e-13	2.36e-10	2.24e-9
L2 error (20ms)	1.19e-9	4.03e-10	8.72e-10	8.15e-10
L2 error (40ms)	6.71e-10	7.13e-10	2.28e-9	3.60e-9

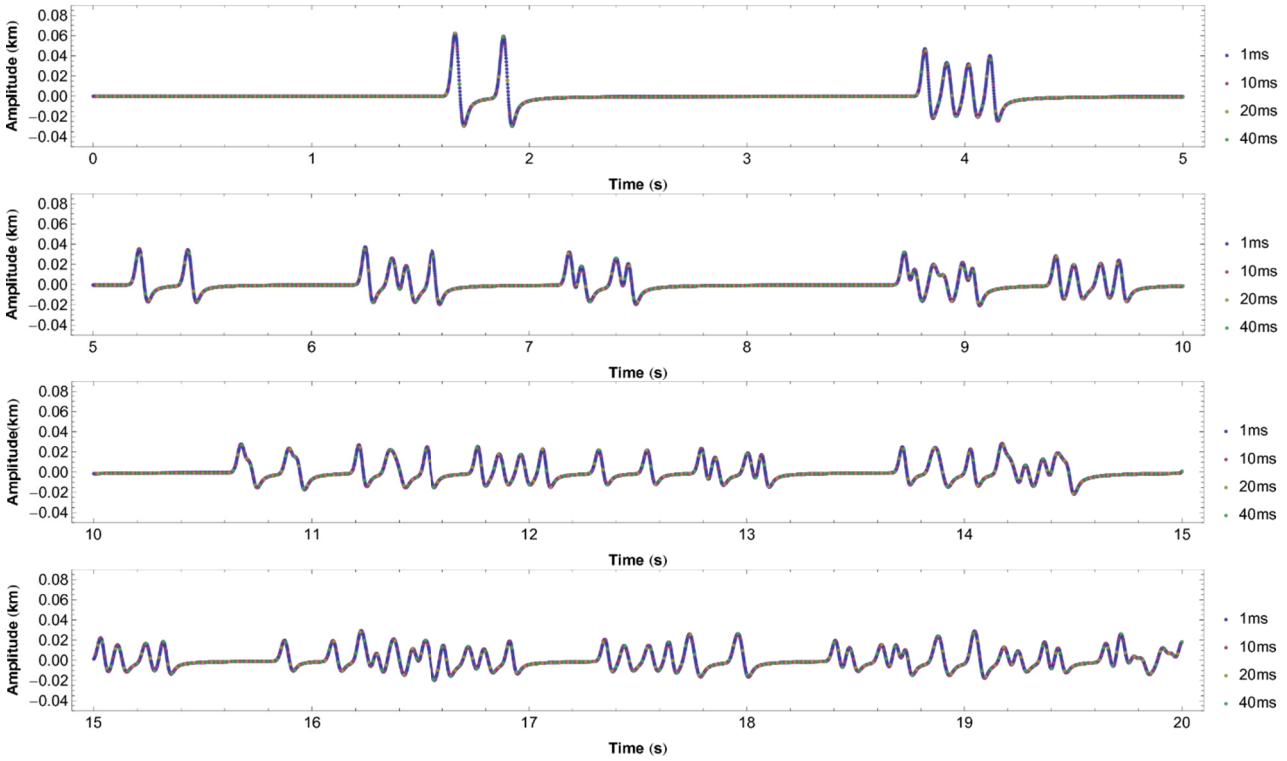

Figure 4.5 Trace at receiver 1 over 20 s simulation of each time step length.

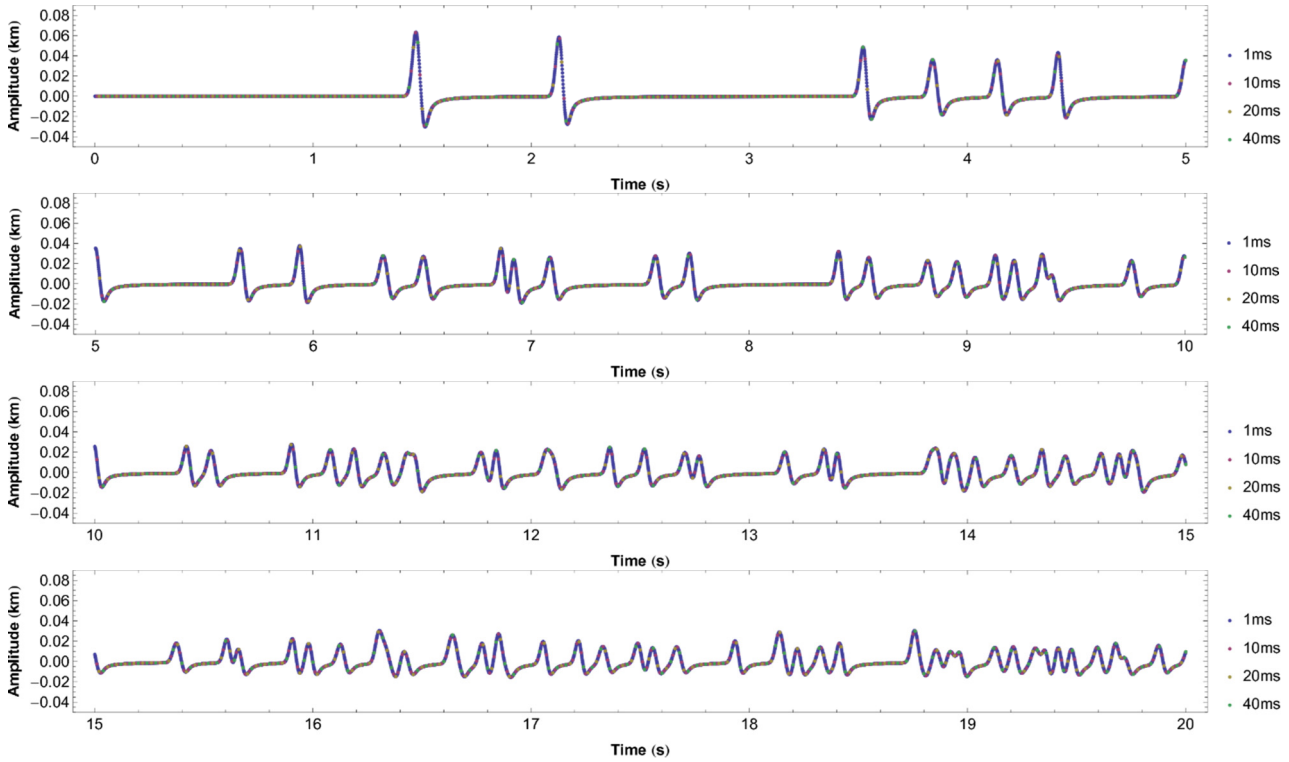

Figure 4.6 Trace at receiver 2 over 20 s simulation of each time step length.

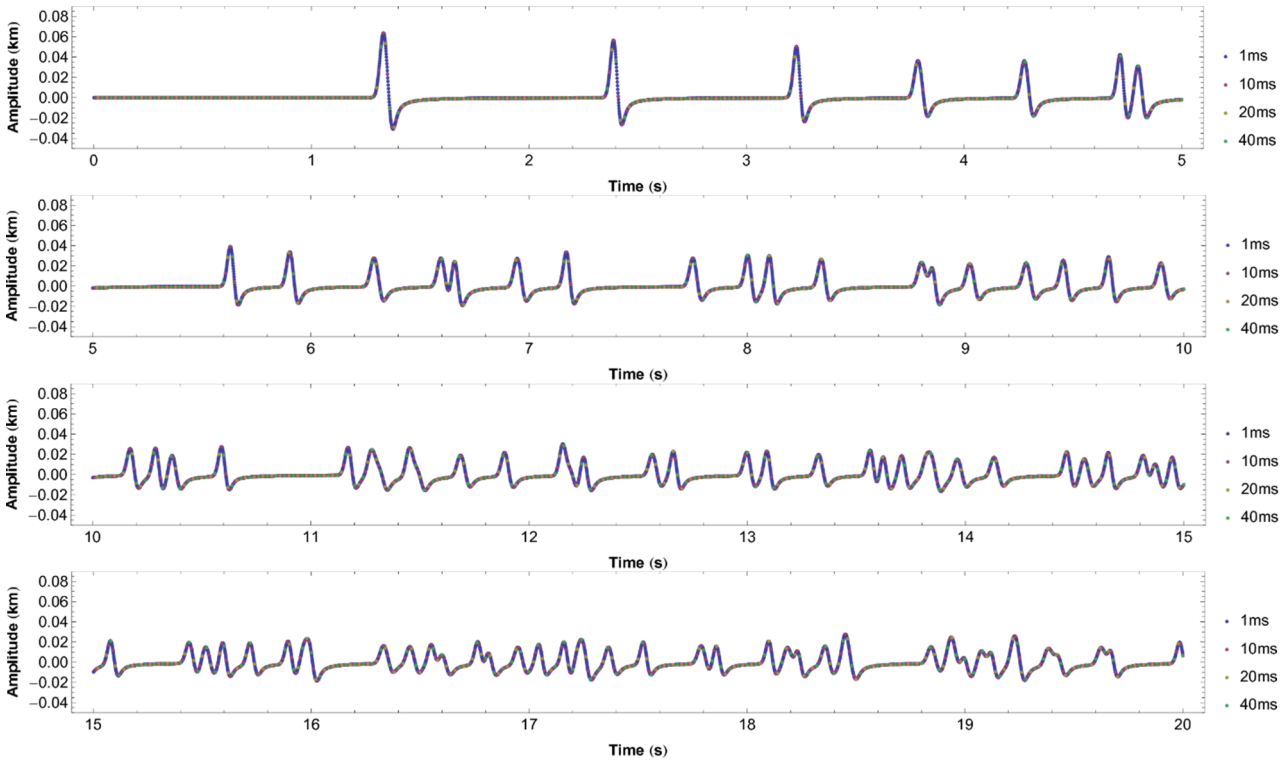

Figure 4.7 Trace at receiver 3 over 20 s simulation of each time step length.

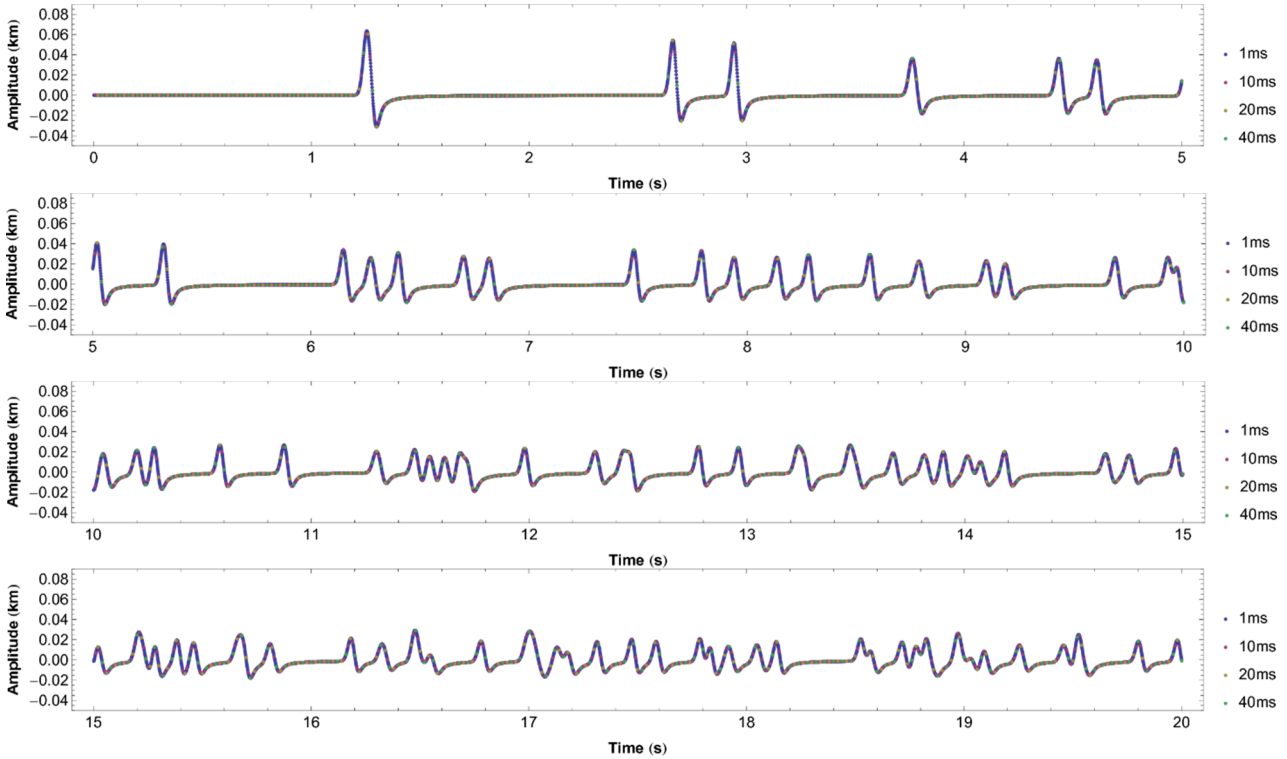

Figure 4.8 Trace at receiver 4 over 20 s simulation of each time step length.

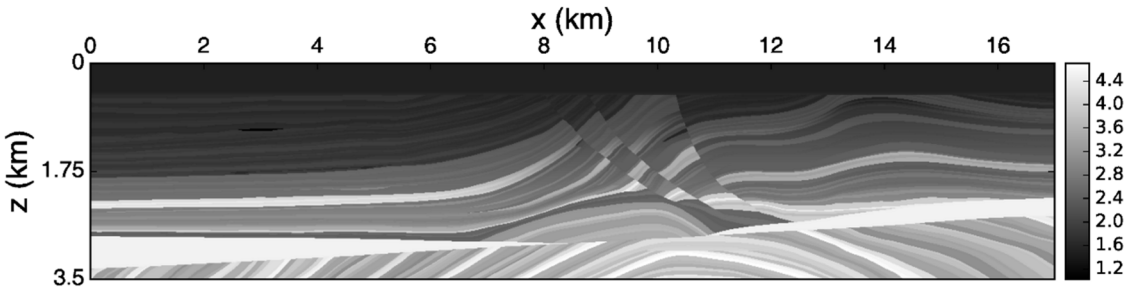

Figure 4.9 The Marmousi-2 model.

Table 4.3 The phase change per time step θ, required l, total number of time steps and total number of multiplications of the operator with respect to each time step length of the simulation using the Marmousi2 model with a 12.5m grid space.

Δt	1ms	10ms	20ms	40ms
θ	1.671	16.705	33.411	66.822
l	8	14	25	49
N_t	20000	2000	1000	500
N_{mat}	340000	58000	51000	49500
CPU time (s)	37416.59	5748.11	5044.08	5029.57

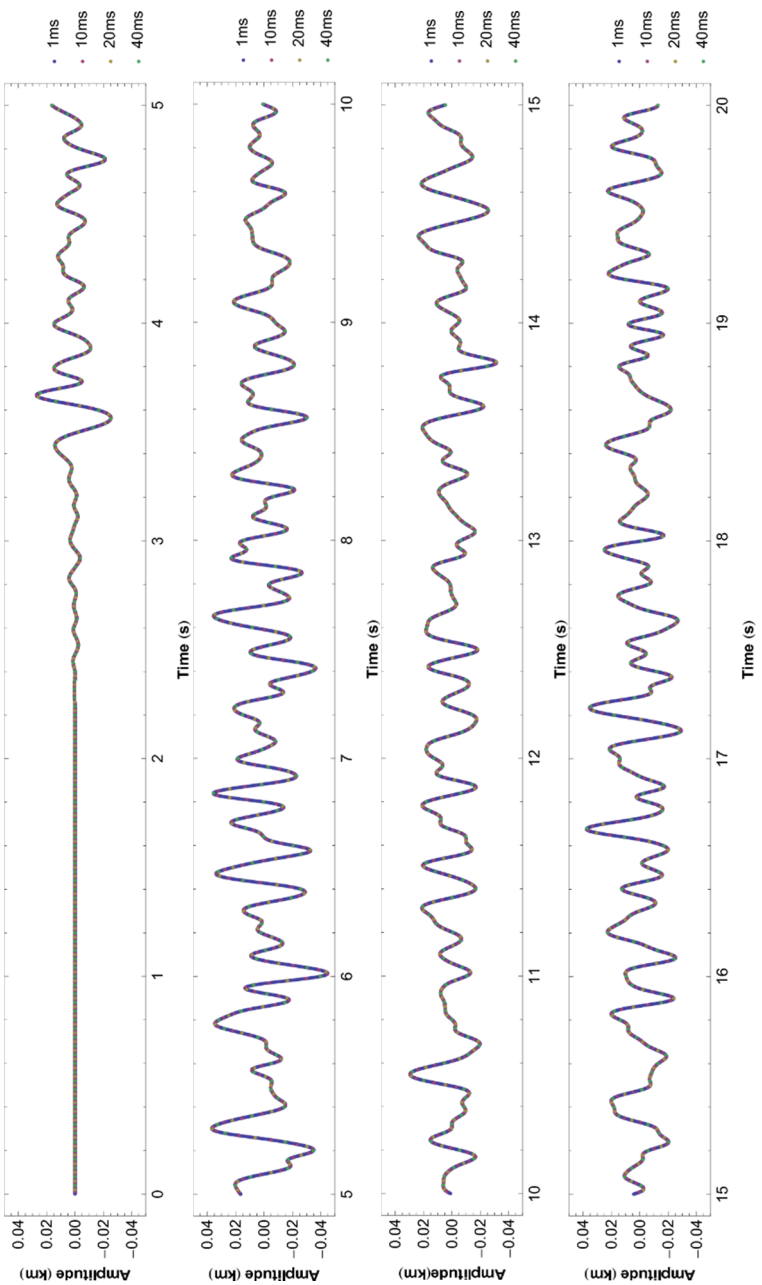

Figure 4.10 Trace at receiver 1 over 20 s simulation of each time step length.

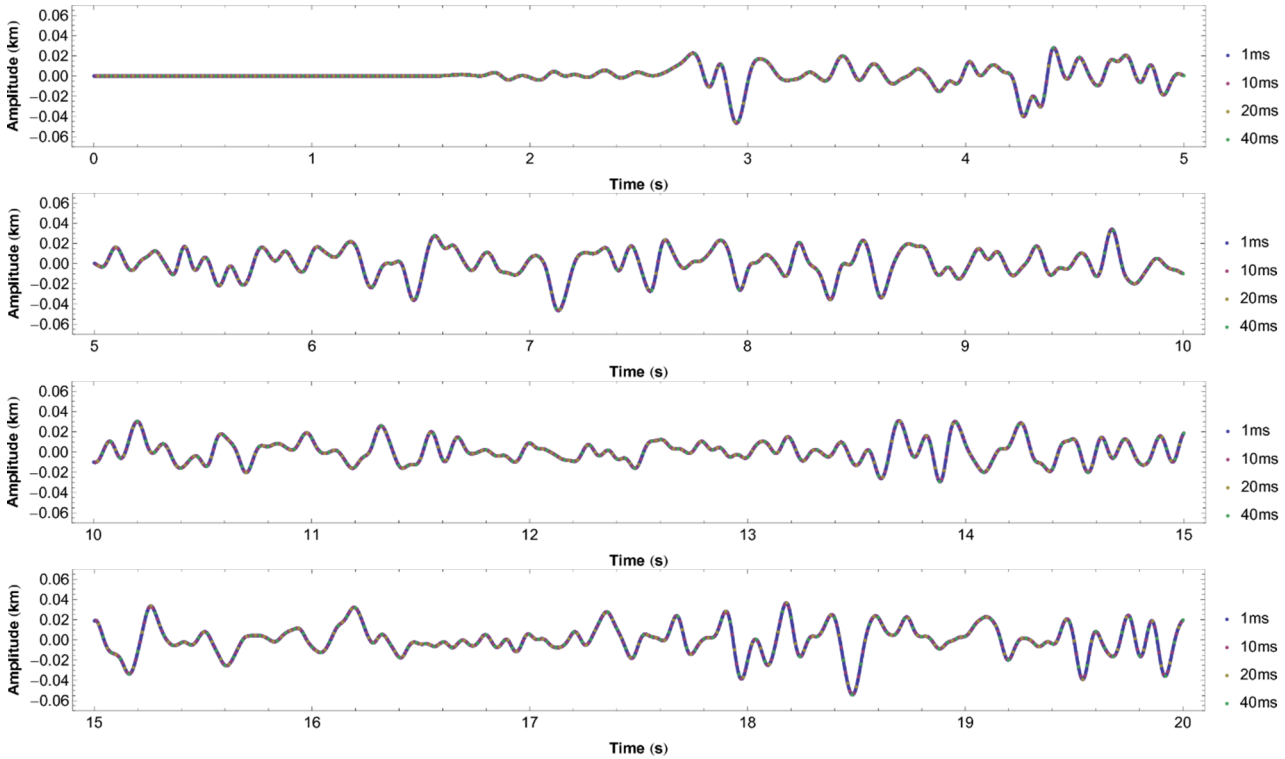

Figure 4.11 Trace at receiver 2 over 20 s simulation of each time step length.

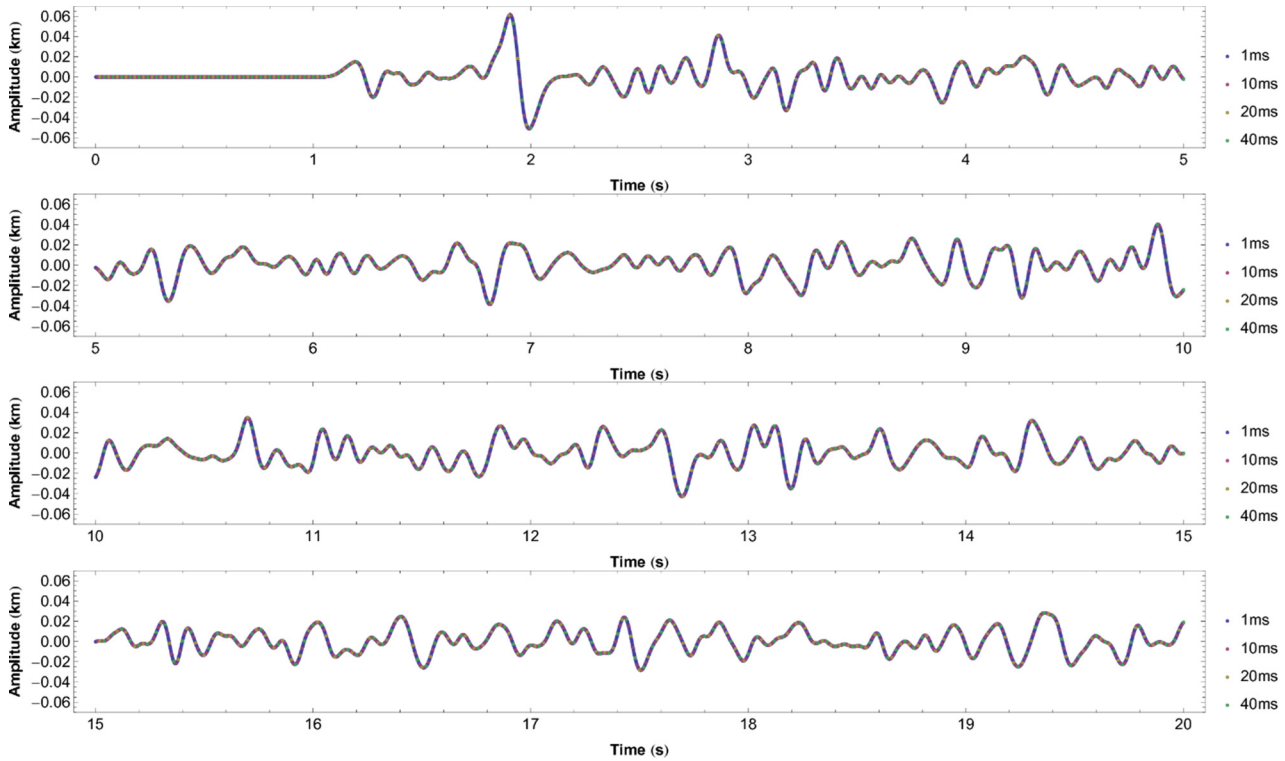

Figure 4.12 Trace at receiver 3 over 20 s simulation of each time step length.

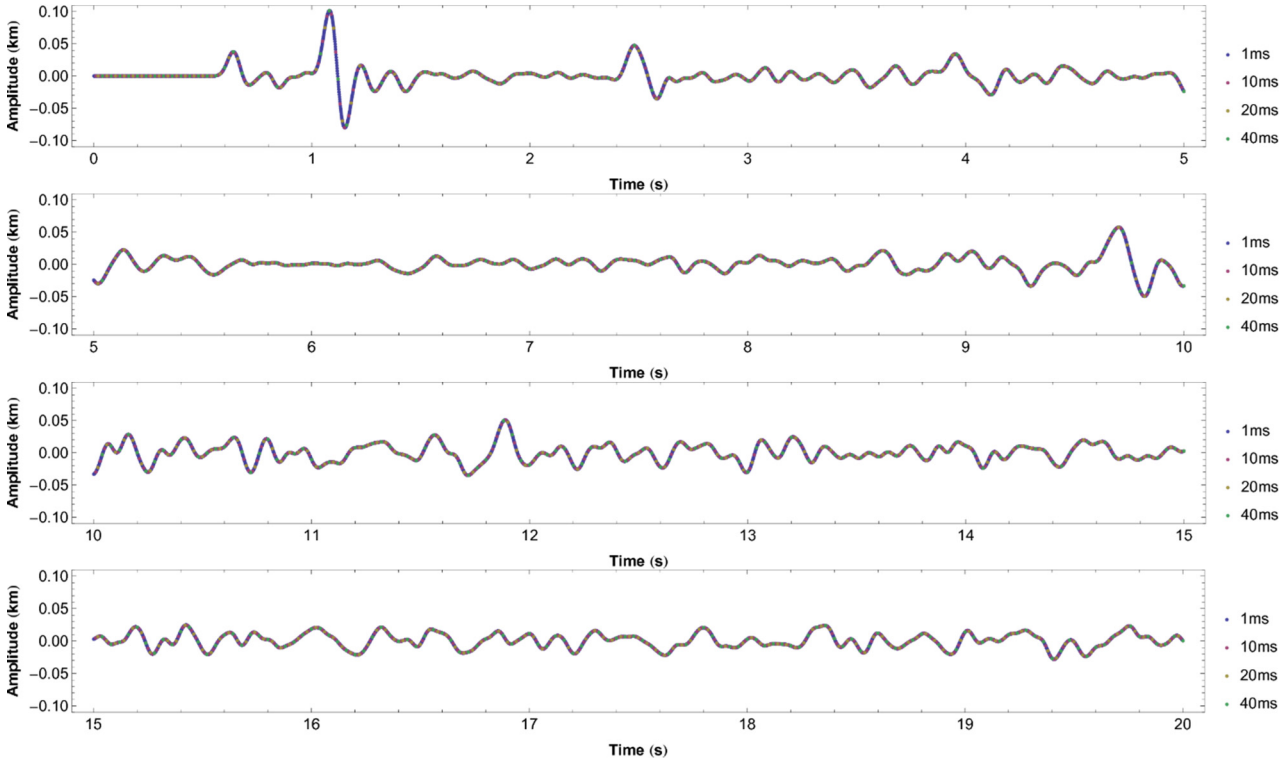

Figure 4.13 Trace at receiver 4 over 20 s simulation of each time step length.

4.2. Source problems

4.2.1. Homogeneous model

As mentioned in section 3.5, there is a limitation on the time step length because the wavefield should cover the maximum frequency of the designed or real source signal. Thus, a dramatically large time step length cannot be used. The size of the velocity model is equivalent to the model utilized in section 4.1.1, and the velocity is a homogeneous 1 km/s elsewhere. A Ricker wavelet $q(t) = (1 - 2k^2)e^{-k^2}$, where $k = \pi(f_0 t - \beta)$ is used as a source wavelet with $f_0 = 10$ Hz and $\beta = 1.00$, as illustrated in Figure 4.14(a). Figure 4.14(b) shows that the most energetic frequency component is 10 Hz and that the frequency band of the wavelet is confined within approximately 30 Hz. Thus, it is reasonable to set f_{max} as 30 Hz, and Δt_{max} (to satisfy that f_{max} is the Nyquist frequency) is 16.667 ms. For the numerical simulation, 1ms, 10ms and Δt_{max} are used. To ensure that the wavefield is smooth, the source is distributed in the Gaussian profile $f(x, z) = e^{-200\left((x-2\pi)^2+(z-2\pi)^2\right)}$. Table 4.4 shows that the computational cost reduces as Δt increases, which is in accordance with N_{mat}. Figure 4.15 illustrates the combined seismogram of each time step length recorded by the line receivers located horizontally at a depth of π. The seismogram shows that three results are in agreement in terms of the scale and location of the event. To precisely visualize the results, traces recorded at (3.1415, 3.1415), (4.7124, 3.1415) and (6.2832, 3.1415) are plotted in Figure 4.21. The traces of each time step length are confirmed to be equivalent. What if a Δt value larger than Δt_{max} is used? In fact, a time step

length slightly longer than Δt_{max} has little effect, as the energy of the source near 30 Hz is relatively small. However, an effectively larger Δt deteriorates the solution, causing the aliasing depicted in Figure 4.17 when Δt is 50 ms. Figure 4.18 illustrates the traces at the three receivers at the same location, and the effect of aliasing is clearly shown in the form of oscillations after the event has passed. Figure 4.19 shows the spectral energy distribution of each trace for different time steps. Although 20 ms and 25 ms are larger than Δt_{max} and the describable frequencies are 25 Hz and 20 Hz, which are less than 30 Hz, the effect on the simulation is negligible, as seen in the spectral distribution, and the result of 50 ms is substantially inaccurate.

4.2.2. Synthetic heterogeneous model: Marmousi-2

For numerical modeling with the synthetic model, the Marmousi2 model is used in section 4.1.2. An equivalent source wavelet is applied with the source distribution in the Gaussian profile $f(x,z) = e^{-200r^2}$, where r is the distance from the center of the computational domain. As the equivalent source wavelet is used, the same set of time step lengths are applied to the computational modeling as 1ms, 10ms and Δt_{max} 16.667 ms. Similar to the previous cases, the computational cost and time decrease as Δt as shown in Table 4.5. Figure 4.20 shows the combined seismogram of each time step length and indicates that the kinematics are in agreement. For a detailed comparison, time traces recorded at (3.75, 0.875), (5.00, 0.875) and (6.25, 0.875) (referred to as the receivers 1, 2 and 3) are plotted in Figure 4.21. Early arrivals are almost equivalent irrespective of the step lengths, while some misfits are found after a

few seconds. It is strikingly revealed in Figure 4.21(b) and (c) that the results of 1 ms and 10 ms have smaller amplitudes at 1.5 s and 1.7 s than those of Δt_{max}. Figure 4.22 depicts the spectral energy distribution of the traces at three receivers; the small misfit in the time trace affects the mid-range of the spectrum from 10 Hz to 20 Hz. These disparities are caused by the effectiveness of the absorbing boundary condition such that the larger time step modeling dampen the solution in the absorbing layer less because of the small number of large time steps used to apply the exponential damping. To verify the effect, simulation was conducted under the same conditions but without the absorbing layer. Figure 4.23 illustrates the combined seismograms of each time step length. The time traces are similar to one another at each receiver, as shown in Figure 4.24, and the spectral energy distribution illustrated in Figure 4.25 of the traces at each receiver confirm this finding. Some misfits of the traces at the extremum points in Figure 4.24 and the slight offsets in the high-frequency region in Figure 4.25 stem from the large time sampling rate and the sparse source wavelet signal because of it. In any case, an effective absorbing boundary for large time strides is required for more accurate modeling of the acoustic wavefield.

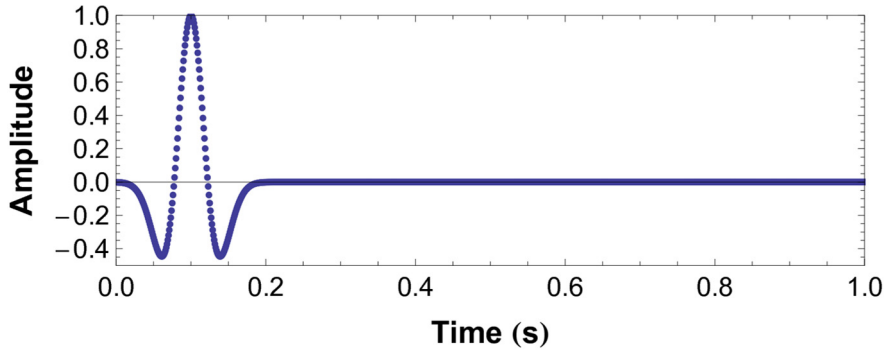

(a)

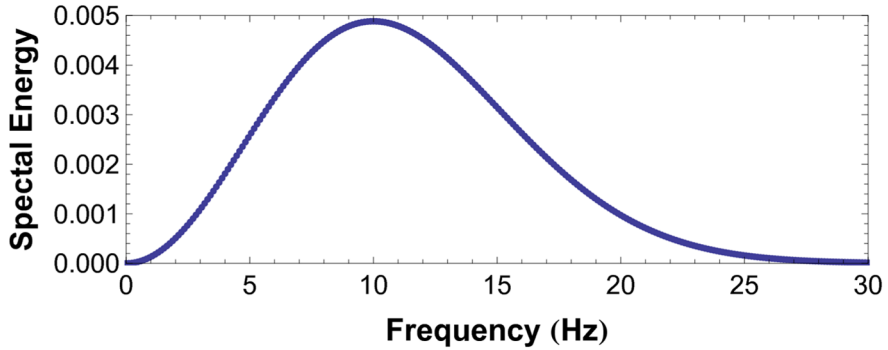

(b)

Figure 4.14 Ricker wavelet imposed on the simulation and its spectral energy distribution.

Table 4.4 The phase change per time step θ, required l, total number of time steps and total number of multiplications of the operator with respect to each time step length of the simulation using a homogeneous model with a 24.5m grid space.

Δt	1ms	10ms	16.67ms
θ	0.181	1.813	3.017
m	1	3	4
N_t	8500	850	510
N_{mat}	25500	5950	4590
CPU Time (s)	1358.88	324.08	272.53

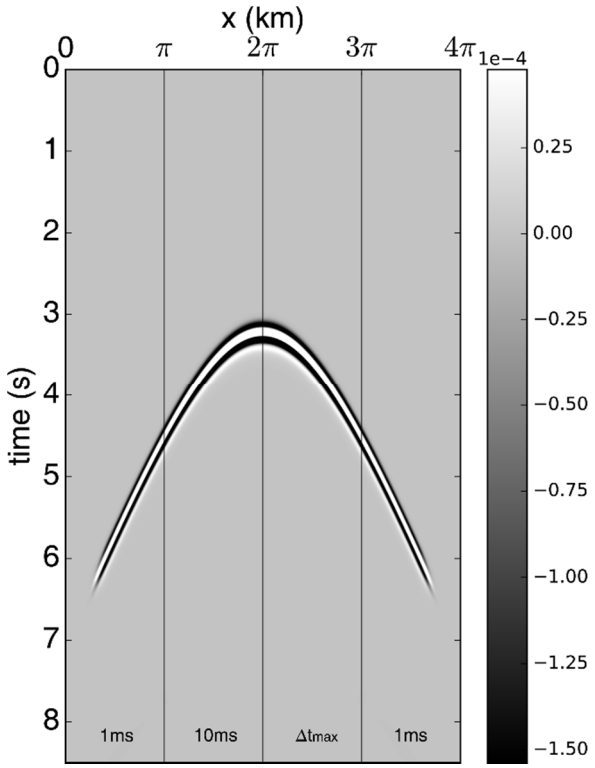

Figure 4.15 Combination of seismograms of each time step length.

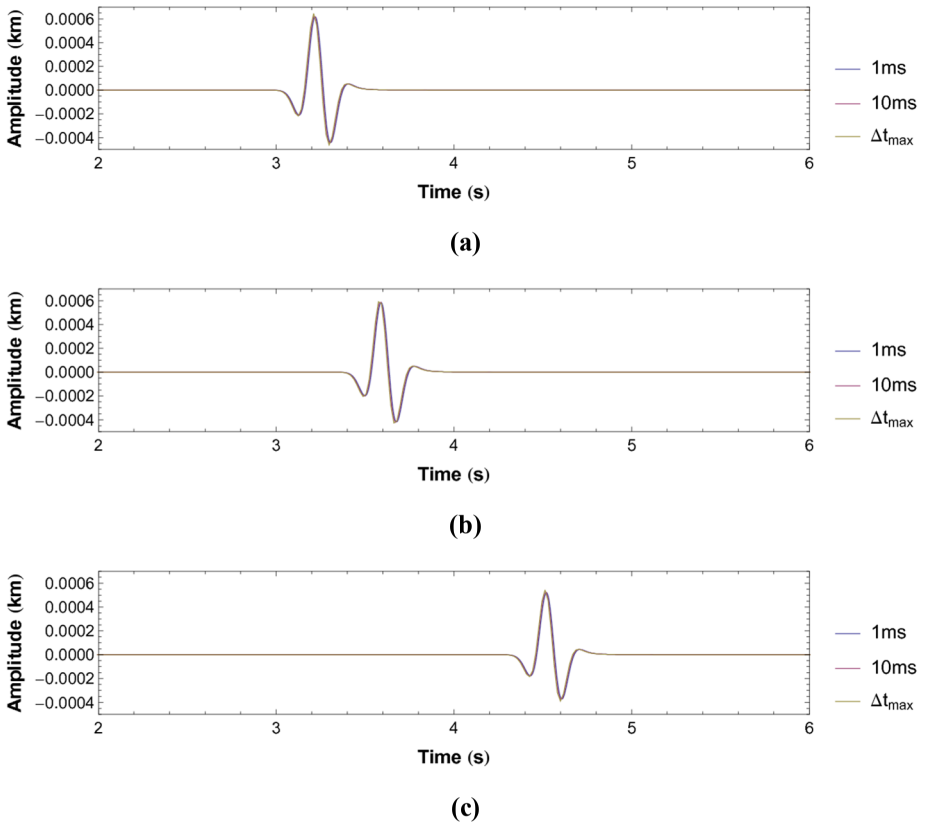

Figure 4.16 Traces at receivers 1 (a), 2 (b) and 3 (c) of each time step length.

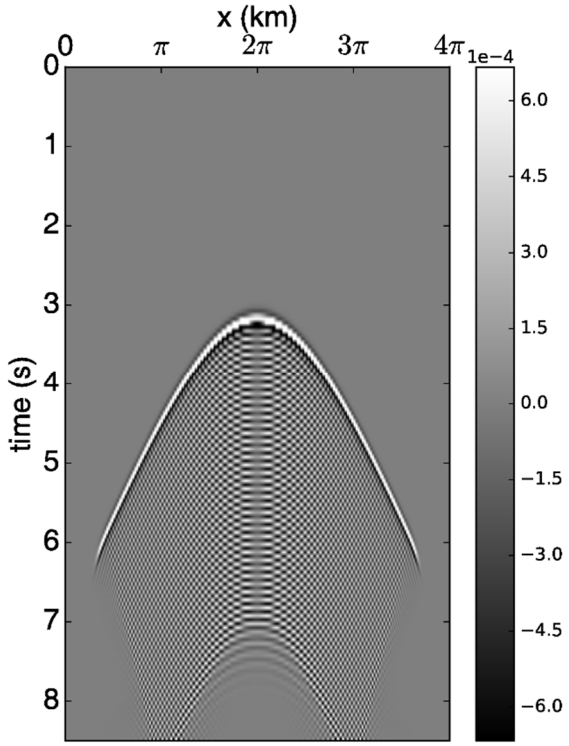

Figure 4.17 Seismogram of the modeling using a homogeneous velocity model using a time step length of $\Delta t = 50$ ms.

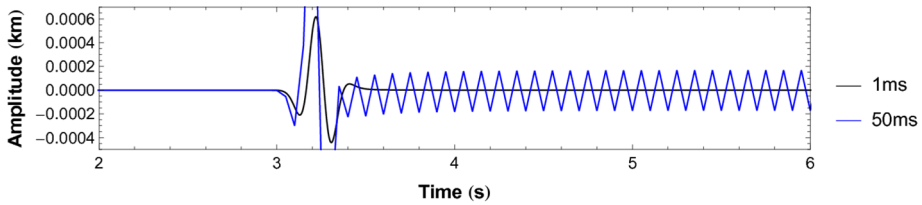

(a)

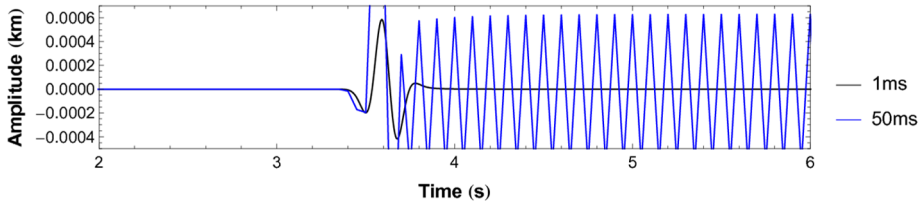

(b)

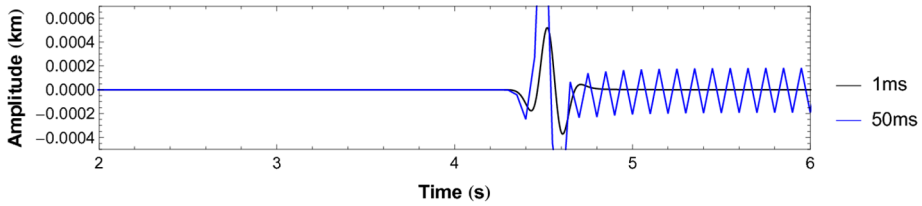

(c)

Figure 4.18 Traces at receivers 1 (a), 2 (b) and 3 (c) of each time step length.

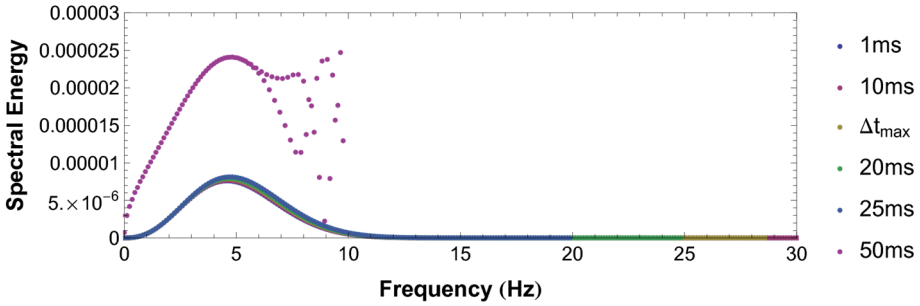

(a)

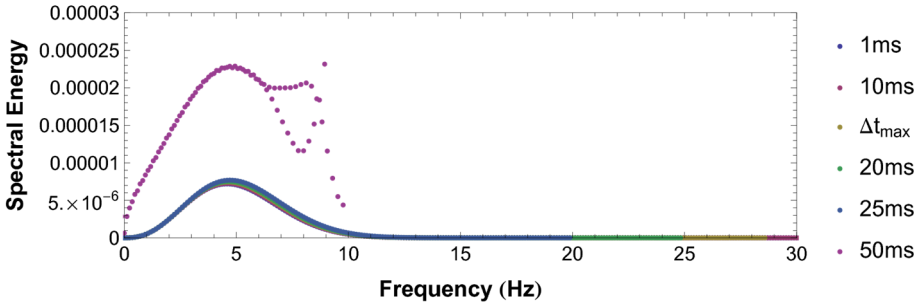

(b)

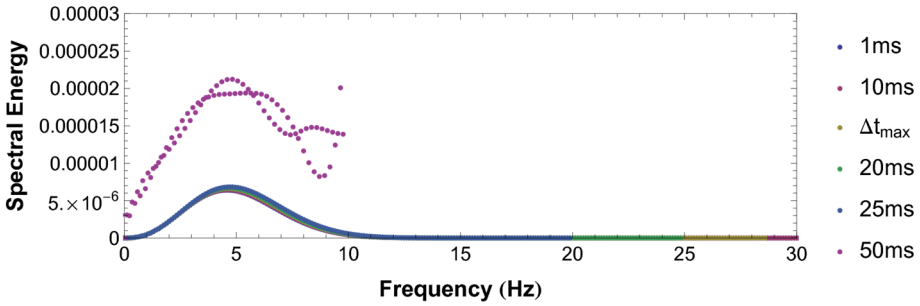

(c)

Figure 4.19 Spectral energy distribution of the traces at receivers 1 (a), 2 (b) and 3 (c) of each time step length.

Table 4.5 The phase change per time step θ, required l, total number of time steps and total number of multiplications of the operator with respect to each time step length of the simulation using the Marmousi2 model with a 12.5m grid space.

Δt	1ms	10ms	16.67ms
θ	1.671	16.705	27.842
l	8	14	21
N_t	5000	500	300
N_{mat}	85000	14500	12900
CPU Time (s)	8332.45	1488.29	1312.90

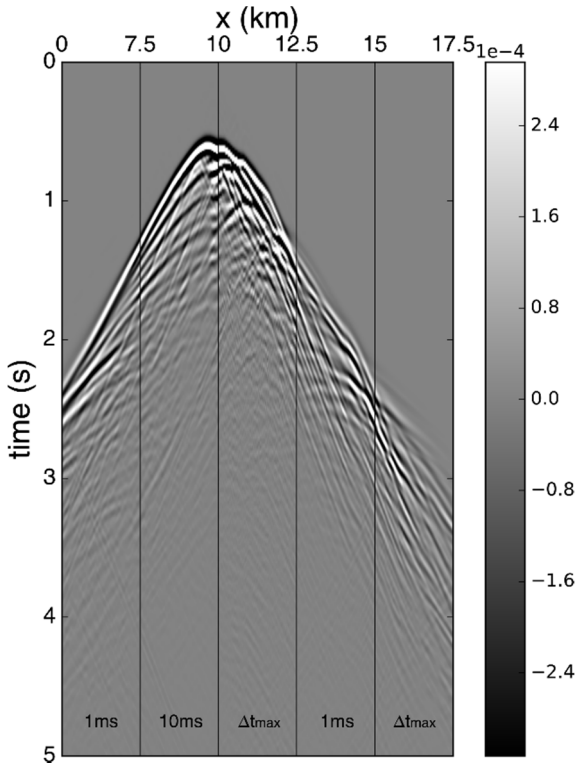

Figure 4.20 Combination of seismograms of each time step length.

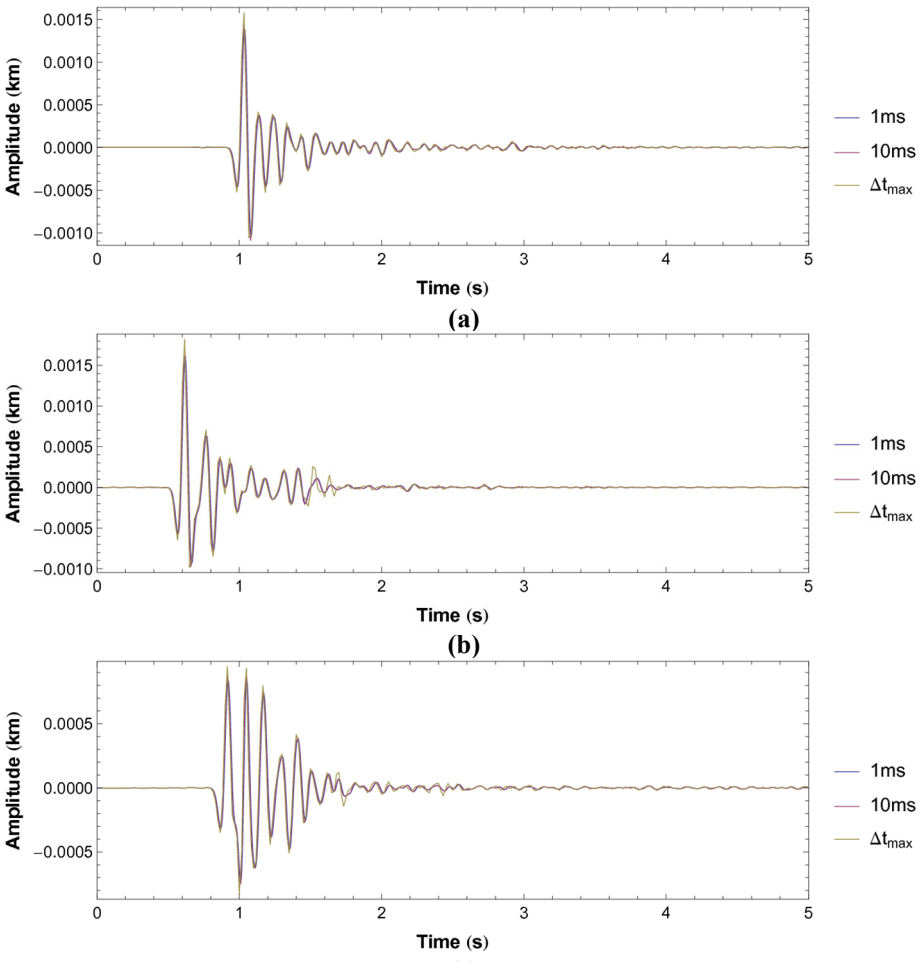

Figure 4.21 Traces at receivers 1 (a), 2 (b) and 3 (c) of each time step length.

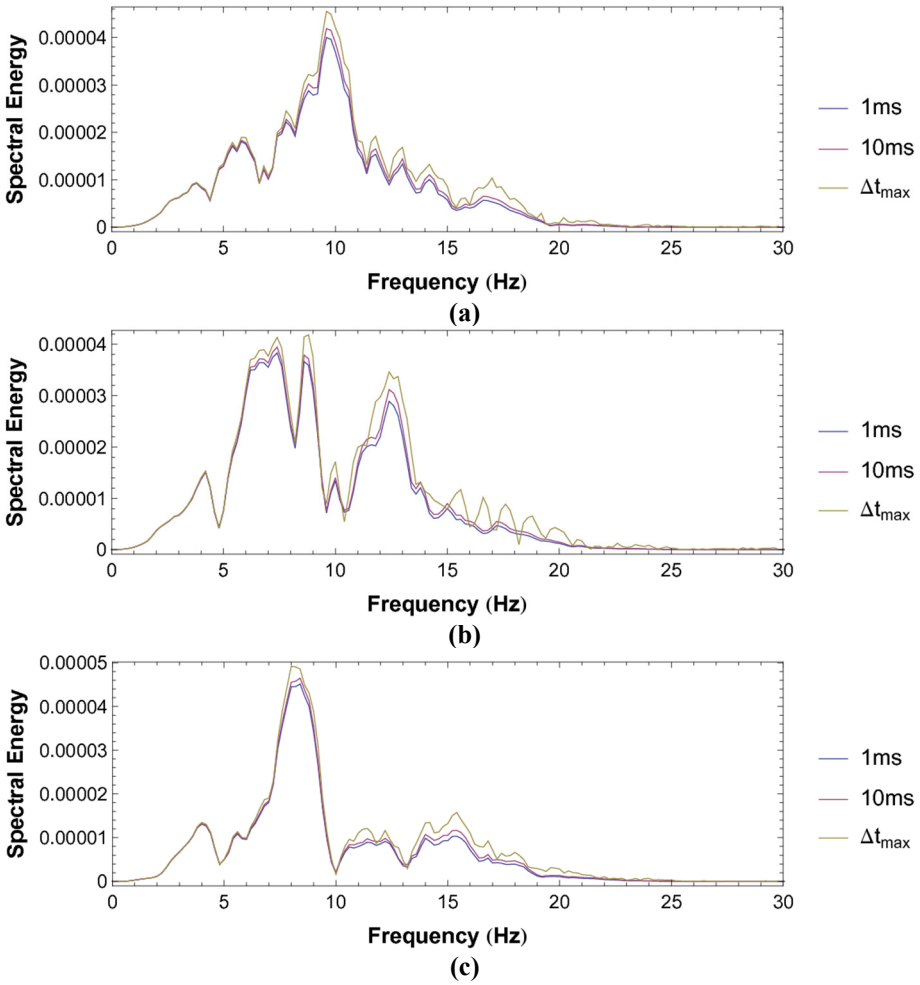

Figure 4.22 Spectral energy distribution of the traces at receivers 1 (a), 2 (b) and 3 (c) of each time step length.

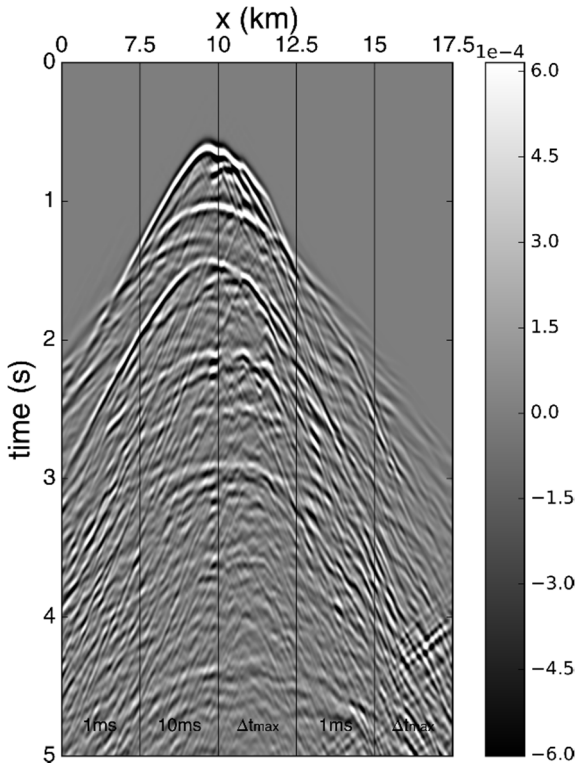

Figure 4.23 Combination of seismograms of each time step length. The absorbing boundary condition is not applied.

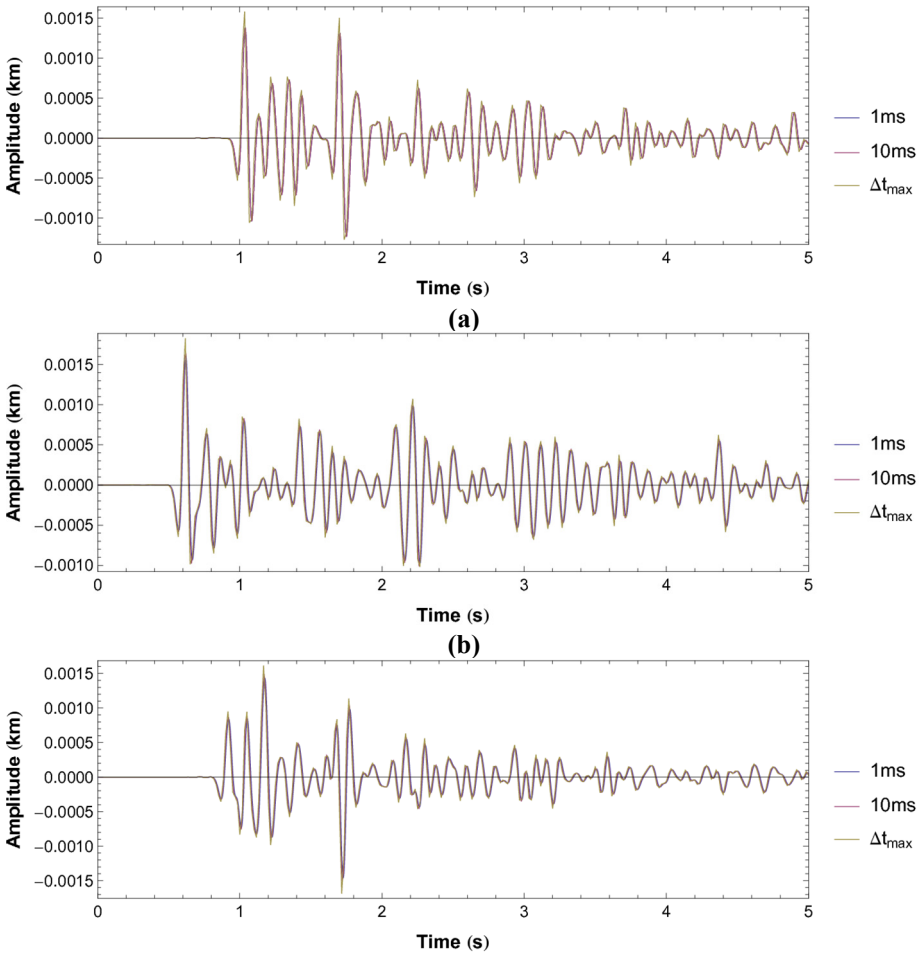

Figure 4.24 Traces at receivers 1 (a), 2 (b) and 3 (c) of each time step length. The absorbing boundary condition is not applied.

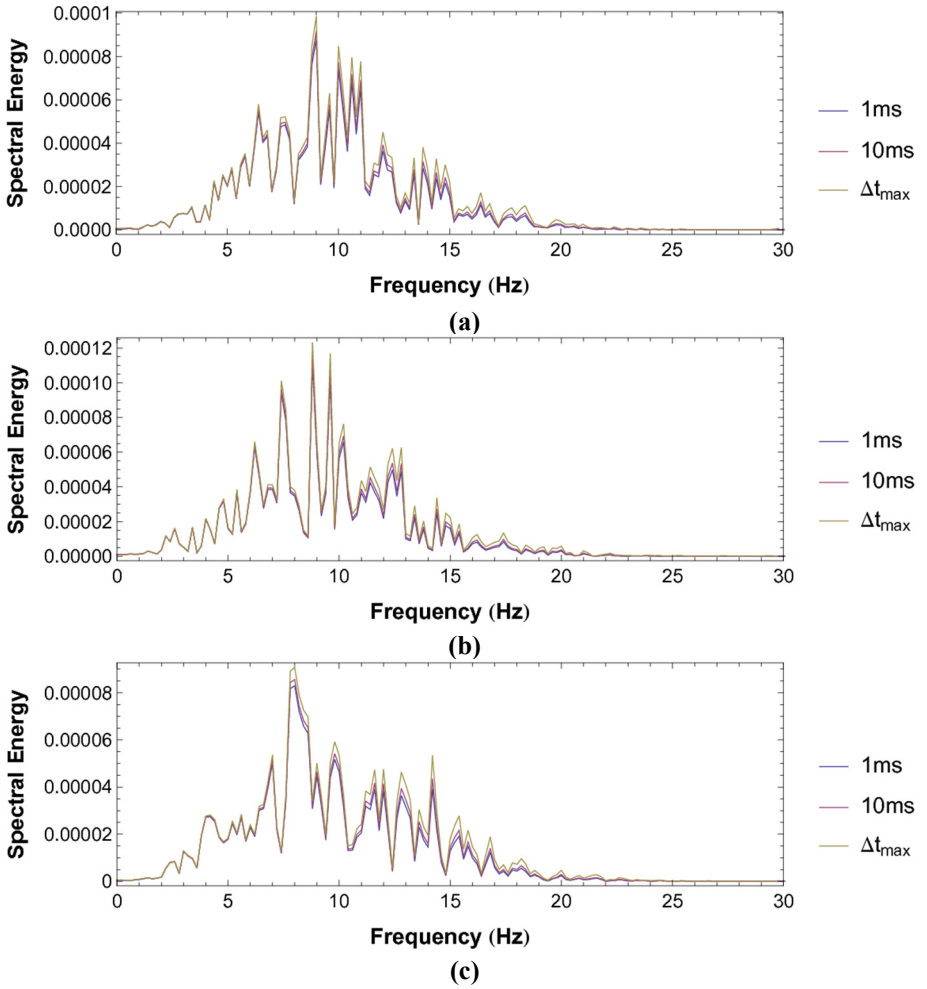

Figure 4.25 Spectral energy distribution of the traces at receivers 1 (a), 2 (b) and 3 (c) of each time step length. The absorbing boundary condition is not applied.

4.3. Discussion on factors debasing the accuracy

These long, numerical results of the initial value and source problems are presented. As illustrated in section 4.1, accurate results can be calculated by the arbitrary-order symplectic time integrator. However, some issues are found from the results of the source problems. First, sponge boundary layers do not work well under certain modeling conditions. The only remedy for this problem is to use thicker absorbing layers unless a more effective absorbing boundary is imposed, such as the perfectly matched layer (PML). However, by numerous simulations, I concluded that the PML does not fit to the PS method with a large time step length because of the unstable nature of the system defined in the PML, which can be found in the appendix section.

The second problem is the misfit of the acoustic wave signals. This problem appears in two major ways: the amplitude errors at the extremum points as shown in the previous section and the aliasing of the signal. To examine the causes of the problem, several source problems are performed under the equivalent modeling conditions of section 4.2.1 except p-wave velocity; four different values from 2 to 5 are used. Figure 4.26 illustrates the traces of each time step length recorded at (4.7124, 3.1415). It is clear that there can be substantive relationships between the accuracy of the source problem and Δt and p-wave velocity; the figure shows that as Δt and p-wave velocity increase, spiky signals are obtained and aliasing even occurs for the velocity of the model higher than 3 km/s even Δt_{max} satisfies the Nyquist sampling theory. Such errors on traces are clearly noted for the results of Δt_{max} at the region over 8Hz as illustrated in Figure 4.27. In my experience, 10 ms is appropriate for the

source problem when imposing the wavelet with maximum frequency of 30 Hz for the simulation with the realistic velocity model found in nature. In general, 30 Hz covers the band of interests for the inverse problems, such as tomography or FWI. Thus, it is reasonable to set Δt equal to or less than 10 ms to guarantee the accuracy of the result. Then, what of the high-resolution image via RTM? In fact, amplitude error does not affect the quality of the migration image at all; such a sharpened signal without a severe phase shift increases the definition of the reflectors. However, aliasing should be avoided such that a fluctuating signal lagging the event significantly deteriorates the resolution of the image. I presume that the sparsity of the source wavelet due to a large time step, as shown in Figure 4.28(b) and (c), causes the spiky results. Then, it would be helpful to select Δt less than Δt_{max} if there are high-velocity structures at the locations of the sources. In my experience, two-thirds of Δt_{max} would be sufficient; however, more consideration is required to determine the appropriate Δt for given modeling conditions.

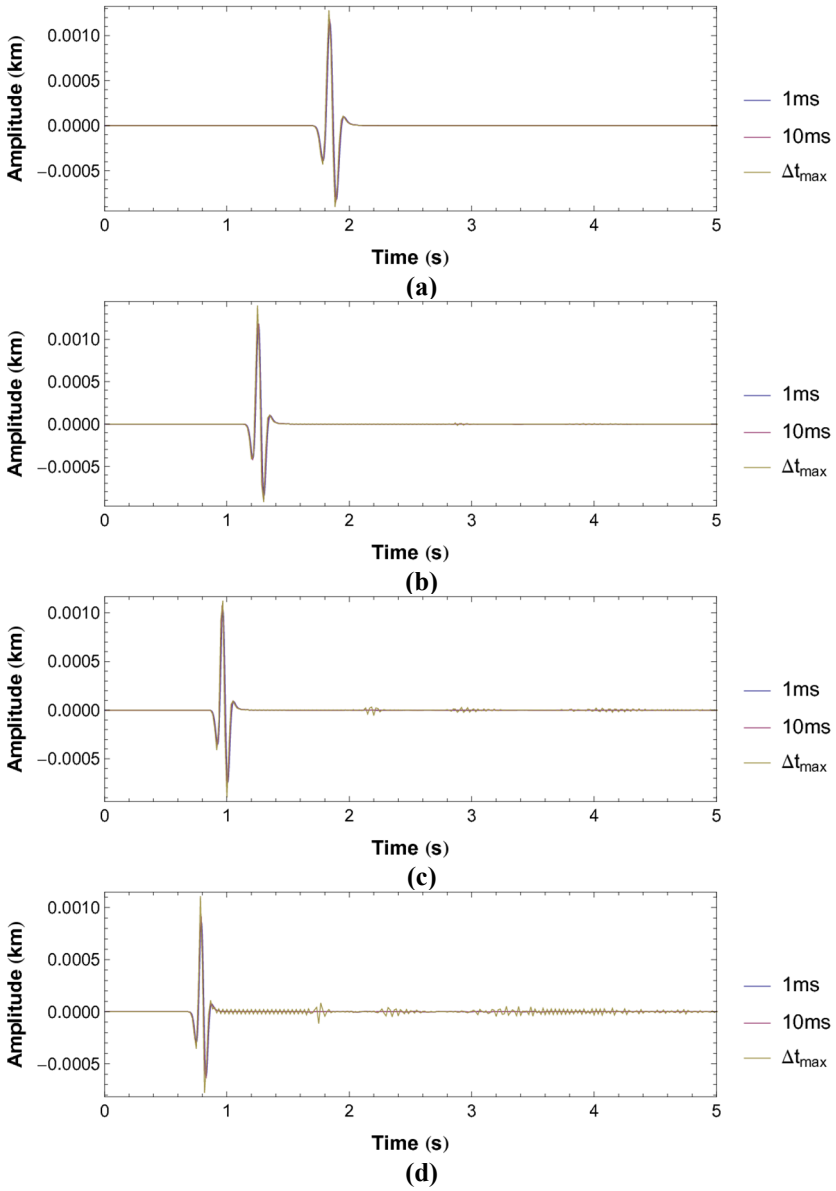

Figure 4.26 Time traces of each time step length recorded at (4.7124, 3.1415) in the homogeneous model of 2 km/s (a), 3 km/s (b), 4 km/s (c) and 5 km/s (d).

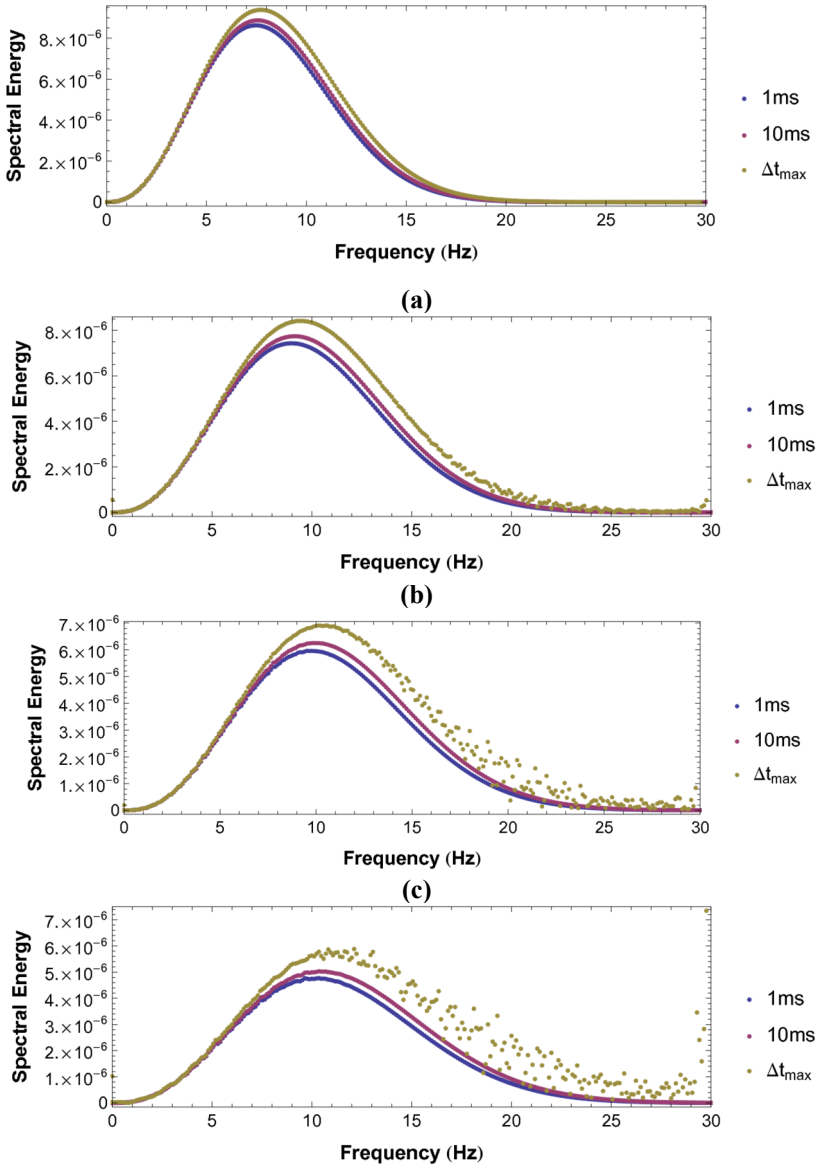

Figure 4.27 Spectral energy distribution of the time traces of each time step length recorded at (4.7124, 3.1415) in the homogeneous model of 2 km/s (a), 3 km/s (b), 4 km/s (c) and 5 km/s (d).

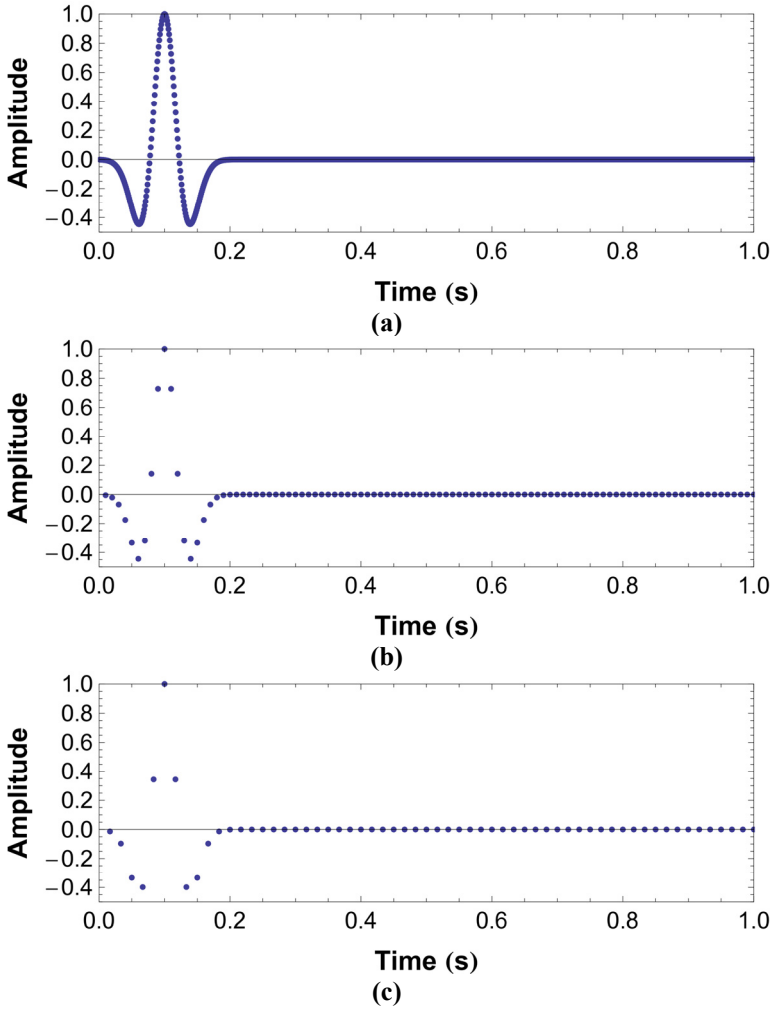

Figure 4.28 Ricker wavelet when the time step length is 1 ms (a), 10 ms (b) and Δt_{max}.

5. Conclusions

An arbitrary-order symplectic time operator is a useful scheme to simulate the acoustic wave equation, which intrinsically satisfies the symplecticity condition irrespective of the variables representing the system PDE. The order of accuracy of the suggested scheme can be increased recursively such that the quality of the result can be easily controlled by the simple choice of the expansion number of the transformation matrix for the given modeling geometries.

The representative characteristics of the arbitrary-order symplectic time operator, such as stability, dispersive characteristic and cumulative phase error, are analyzed by solving the eigenvalue problems of the approximate symplectic map of each expansion order. A non-symplectic time discretization method that has the equivalent computational cost per time step to the suggested scheme is also analyzed to compare the effect of symplecticity. The stability criterion and the allowed time step length to obey the given error restriction are twice when considering the property. This enables the computational cost of the suggested method to be reduced as much as half compared with the scheme not considering symplecticity. A strategy to select the number of the expansion of

the symplectic map is suggested that is based on the similarity of an actual eigenvalue and that of the approximate matrix; the suggested strategy is more effective in terms of quality and computational cost when the allowed maximum time step length is applied.

The numerical simulation results provide evidence that precise modeling is possible using the arbitrary-order symplectic time operator with a large time step length. However, several issues are found when the scheme is applied to the source problem because of the intrinsic limitation on the time discretized solution of a source problem. Thus, numerical results are inaccurate when performing a simulation with a large time step length when the source is imposed at high velocity region. In addition, a large time step length or high p-wave model causes the acoustic wave to pass the absorbing boundary layer that is not dampened sufficiently. A practical remedy for these problems is to use a thicker boundary condition or reduce the time stride. Spiky events due to the sparse sampling of the source wavelet do not affect the quality of RTM results. However, aliasing should be avoided by reducing the time step length; two-thirds of the maximum value is recommended based on my experience.

The arbitrary-order symplectic time integrator can be applied to practical problems, i.e., the high-resolution imaging via RTM or FWI of multicomponent data. Other types of problems, such as elastodynamics or electromagnetics, are also Hamiltonian systems; the suggested scheme can be extended to those fields in future works. Although the PS method is used to differentiate the variable, it would be meaningful to use other discretization techniques, such as finite difference or finite element methods, which remains for future works. In this

case, the scheme's characteristics are expected to be considerably different from the analysis results of this study because of the effect of spatial dispersion errors.

References

Araujo, E. S., Pestana, R. C., & dos Santos, A. W. (2014). Symplectic scheme and the Poynting vector in reverse-time migration. Geophysics, 79(5), S163-S172.

Arnold, D. N., Brezzi, F., Cockburn, B., & Marini, L. D. (2002). Unified analysis of discontinuous Galerkin methods for elliptic problems. SIAM journal on numerical analysis, 39(5), 1749-1779.

Baysal, E., Kosloff, D. D., & Sherwood, J. W. (1983). Reverse time migration. Geophysics, 48(11), 1514-1524.

Bonomi, E., Brieger, L., Nardone, C., & Pieroni, E. (1998). 3D spectral reverse time migration with no-wraparound absorbing conditions. In 68th Annual Meeting, Society Of Exploration Geophysicists.

Cerjan, C., Kosloff, D., Kosloff, R., & Reshef, M. (1985). A nonreflecting boundary condition for discrete acoustic and elastic wave equations. Geophysics, 50(4), 705-708.

Chen, J. B. (2009). Lax-Wendroff and Nyström methods for seismic modelling. Geophysical Prospecting, 57(6), 931-941.

Cohen, G., & Joly, P. (1990). Fourth order schemes for the heterogeneous acoustics equation. Computer Methods in Applied Mechanics and Engineering, 80(1-3), 397-407.

Crank, J., & Nicolson, P. (1947). A practical method for numerical evaluation of solutions of partial differential equations of the heat-conduction type. In Mathematical Proceedings of the Cambridge Philosophical Society (Vol. 43, No. 01, pp. 50-67). Cambridge University Press.

Dablain, M. A. "The application of high-order differencing to the scalar wave equation." *Geophysics* 51.1 (1986): 54-66.

De Basabe, J. D., Sen, M. K., & Wheeler, M. F. (2008). The interior penalty discontinuous Galerkin method for elastic wave propagation: grid dispersion. Geophysical Journal International, 175(1), 83-93.

del Castillo, G. F. T., & Linares, E. G. (2003). Hamiltonian structures for the acoustic field. Revista Mexicana de Física, 49(4), 344-347.

Dumbser, M., & Käser, M. (2006). An arbitrary high-order discontinuous Galerkin method for elastic waves on unstructured meshes—II. The three-dimensional isotropic case. Geophysical Journal International, 167(1), 319-336.

Dumbser, M., Käser, M., & Toro, E. F. (2007). An arbitrary high-order Discontinuous Galerkin method for elastic waves on unstructured meshes-V. Local time stepping and p-adaptivity. Geophysical Journal International, 171(2), 695-717.

Etgen, J. T., & Brandsberg-Dahl, S. (2009). The pseudo-analytical method: Application of pseudo-Laplacians to acoustic and acoustic anisotropic wave propagation. In 2009 SEG Annual Meeting. Society of Exploration Geophysicists.

Iwatsu, R. (2009). Two new solutions to the third-order symplectic integration method. Physics Letters A, 373(34), 3056-3060.

Fairweather, G., & Mitchell, A. R. (1967). A new computational procedure for ADI methods. SIAM Journal on Numerical Analysis, 4(2), 163-170.

Forest, E., & Ruth, R. D. (1990). Fourth-order symplectic integration. Physica D: Nonlinear Phenomena, 43(1), 105-117.

Fornberg, B. (1988). Generation of finite difference formulas on arbitrarily spaced grids. Mathematics of computation, 51(184), 699-706.

Geller, R. J., & Takeuchi, N. (1998). Optimally accurate second-order time-domain finite difference scheme for the elastic equation of motion: one-dimensional cases. Geophysical Journal International, 135(1), 48-62.

Goldstein, H. (1965). Classical mechanics. Pearson Education India.

Grote, M. J., & Sim, I. (2010). Efficient PML for the wave equation. arXiv preprint arXiv:1001.0319.

Hairer, E., Lubich, C., & Wanner, G. (2006). Geometric numerical integration: structure-preserving algorithms for ordinary differential equations (Vol. 31). Springer Science & Business Media.

Hesthaven, J. S., & Warburton, T. (2007). Nodal discontinuous Galerkin methods: algorithms, analysis, and applications. Springer Science & Business Media.

Hermann, Verena, Martin Käser, and Cristóbal E. Castro. "Non-conforming hybrid meshes for efficient 2-D wave propagation using the Discontinuous Galerkin Method." Geophysical Journal International 184.2 (2011): 746-758.

Käser, M., & Dumbser, M. (2006). An arbitrary high-order discontinuous Galerkin method for elastic waves on unstructured meshes—I. The two-dimensional isotropic case with external source terms. Geophysical Journal International, 166(2), 855-877.

Kim, S., & Lim, H. (2007). High-order schemes for acoustic waveform simulation. Applied Numerical Mathematics, 57(4), 402-414.

Komatitsch, D., & Vilotte, J. P. (1998). The spectral element method: An efficient tool to simulate the seismic response of 2D and 3D geological structures. Bulletin of the seismological society of America, 88(2), 368-392.

Kosloff, D., Queiroz Filho, A., Tessmer, E., & Behle, A. (1989). Numerical solution of the acoustic and elastic wave equations by a new rapid expansion method. Geophysical Prospecting, 37(4), 383-394.

Lavelle, J. W., & Thacker, W. C. (2008). A pretty good sponge: Dealing with open boundaries in limited-area ocean models. Ocean Modelling, 20(3), 270-292.

Lax, P. D., & Wendroff, B. (1964). Difference schemes for hyperbolic equations with high order of accuracy. Communications on pure and applied mathematics, 17(3), 381-398.

Levander, A. R. (1988). Fourth-order finite-difference P-SV seismograms. Geophysics, 53(11), 1425-1436.

LeVeque, R. J. (2002). Finite volume methods for hyperbolic problems (Vol. 31). Cambridge university press.

Li, J., Fehler, M., Yang, D., & Huang, X. (2014). 3D weak-dispersion reverse time migration using a stereo-modeling operator. Geophysics, 80(1), S19-S30.

Liu, Y., & Sen, M. K. (2009). A new time–space domain high-order finite-difference method for the acoustic wave equation. Journal of computational Physics, 228(23), 8779-8806.

Liu, Y., & Sen, M. K. (2011). Scalar wave equation modeling with time–space domain dispersion-relation-based staggered-grid finite-difference schemes. Bulletin of the Seismological Society of America, 101(1), 141-159.

Liu, Y., & Sen, M. K. (2013). Time–space domain dispersion-relation-based finite-difference method with arbitrary even-order accuracy for the 2D acoustic wave equation. Journal of Computational Physics, 232(1), 327-345.

Lu, X., & Schmid, R. (1997). A symplectic algorithm for wave equations. Mathematics and Computers in simulation, 43(1), 29-38.

Marfurt, K. J. (1984). Accuracy of finite-difference and finite-element modeling of the scalar and elastic wave equations. Geophysics, 49(5), 533-549.

Ma, X., Yang, D., & Liu, F. (2011). A nearly analytic symplectically partitioned Runge–Kutta method for 2-D seismic wave equations. Geophysical Journal International, 187(1), 480-496.

Ma, X., Yang, D., Song, G., & Wang, M. (2014). A low-dispersive symplectic partitioned Runge–Kutta method for solving seismic-wave equations: I. scheme and theoretical analysis. Bulletin of the Seismological Society of America.

Ma, X., Yang, D., & Song, G. (2015). A Low-Dispersive Symplectic Partitioned Runge–Kutta Method for Solving Seismic-Wave Equations: II. Wavefield Simulations. Bulletin of the Seismological Society of America.

Okunbor, D., & Skeel, R. D. (1992). Explicit canonical methods for Hamiltonian systems. Mathematics of computation, 59(200), 439-455.

Park, H., Lee, J., Lee, K., & Shin, C. (2014). A split formulation of the nearly perfectly matched layer for an acoustic wave equation using the discontinuous Galerkin method. Proc. SEG Tech. Program Expand Abstract, 3344-3348.

Pestana, R. C., & Stoffa, P. L. (2010). Time evolution of the wave equation using rapid expansion method. Geophysics, 75(4), T121-T131.

Pratt, R. Gerhard, Changsoo Shin, and G. J. Hick. "Gauss–Newton and full Newton methods in frequency–space seismic waveform inversion." Geophysical Journal International 133.2 (1998): 341-362.

Ruth, R. D. (1983). A canonical integration technique. IEEE Trans. Nucl. Sci, 30(4), 2669-2671.

Shin, C., & Cha, Y. H. (2008). Waveform inversion in the Laplace domain. Geophysical Journal International, 173(3), 922-931.

Shin, C., & Cha, Y. H. (2009). Waveform inversion in the Laplace—Fourier domain. Geophysical Journal International, 177(3), 1067-1079.

Tal-Ezer, H. (1986). Spectral methods in time for hyperbolic equations. SIAM Journal on Numerical Analysis, 23(1), 11-26.

Tam, C. K., & Webb, J. C. (1993). Dispersion-relation-preserving finite difference schemes for computational acoustics. Journal of computational physics, 107(2), 262-281.

Tan, S., & Huang, L. (2014). An efficient finite-difference method with high-order accuracy in both time and space domains for modelling scalar-wave propagation. Geophysical Journal International, ggu077.

Tarantola, A. (1983). Nonlinear inverse problem for an heterogeneous acoustic medium. Pre-print submitted to Geophysics, 295.

Tarantola, A. (1984). Inversion of seismic reflection data in the acoustic approximation. Geophysics, 49(8), 1259-1266.

Trefethen, L. N. (2000). Spectral methods in MATLAB (Vol. 10). SIAM.

Virieux, J. (1986). P-SV wave propagation in heterogeneous media: Velocity-stress finite-difference method. Geophysics, 51(4), 889-901.

Whitmore, N. D. (1983). Iterative depth migration by backward time propagation. In 1983 SEG Annual Meeting. Society of Exploration Geophysicists.

Yee, K. S. (1966). Numerical solution of initial boundary value problems involving Maxwell's equations in isotropic media. IEEE Trans. Antennas Propag, 14(3), 302-307.

Yoshida, H. (1990). Construction of higher order symplectic integrators. Physics Letters A, 150(5), 262-268.

Appendix A. Additional formulations

A1. Absorbing boundary conditions

Absorbing boundary conditions (ABCs) terminate undesired waves reflected from the edges of a computational domain. As a result of the absorbing boundary, we can confine the domain within the zone of interest to perform numerical modeling of unbounded media. The PML is a type of absorbing boundary, introduced by Berenger (1994), and it is known as the most effective such boundary condition. The PML can dampen waves within a layer with a thickness of tens of nodes regardless of the frequency and incidence angle. Among the variants on the PML schemes, I consider the method invented by Park et al. (2014) and Grote and Sim (2010) for systems (2.1.21a) and (2.1.21b), respectively. Note that the system equation in the PML layer is clearly not symplectic as the determinant of the characteristic matrix M cannot be equal to one because of the dissipation of the wavefield. Nevertheless, PML schemes have been applied to wave equation. In the following, I introduce a technique to impose a PML using an arbitrary-order symplectic time integrator.

Park et al. (2014) extended the first-order system of an acoustic wave in the PML zone by dividing the pressure field p into p_x and p_z as follows:

$$\begin{aligned}
\frac{\partial p_x}{\partial t} &= -\rho_0 c^2 \left(\frac{\partial u}{\partial x} + \frac{\partial v}{\partial z}\right) - d_x p_x \\
\frac{\partial p_z}{\partial t} &= -\rho_0 c^2 \left(\frac{\partial u}{\partial x} + \frac{\partial v}{\partial z}\right) - d_z p_z \\
\frac{\partial u}{\partial t} &= -\frac{1}{\rho_0}\frac{\partial p_x}{\partial x} - d_x u
\end{aligned} \tag{A1.1}$$

$$\frac{\partial v}{\partial t} = -\frac{1}{\rho_0}\frac{\partial p_z}{\partial z} - d_x v$$

where d_x and d_z are damping profiles with respect to the x and z directions. The scheme is simple to implement. An increase in the variable does not incur additional computational cost because we can reuse the spatial derivatives once it is calculated. p_x and p_z are identical in the domain of interest but yield different values in the PML zone. Thus, we can choose either of them as the pressure field. The characteristic matrix of (A1.1) is:

$$M = \begin{bmatrix} -d_x & 0 & -\rho_0 c^2 \frac{\partial}{\partial x} & -\rho_0 c^2 \frac{\partial}{\partial z} \\ 0 & -d_z & -\rho_0 c^2 \frac{\partial}{\partial x} & -\rho_0 c^2 \frac{\partial}{\partial z} \\ -\frac{1}{\rho_0}\frac{\partial}{\partial x} & 0 & -d_x & 0 \\ 0 & -\frac{1}{\rho_0}\frac{\partial}{\partial z} & 0 & -d_z \end{bmatrix} \tag{A1.2}$$

and $M = N + D$ where

$$N = \begin{bmatrix} 0 & 0 & -\rho_0 c^2 \frac{\partial}{\partial x} & -\rho_0 c^2 \frac{\partial}{\partial z} \\ 0 & 0 & -\rho_0 c^2 \frac{\partial}{\partial x} & -\rho_0 c^2 \frac{\partial}{\partial z} \\ -\frac{1}{\rho_0}\frac{\partial}{\partial x} & 0 & 0 & 0 \\ 0 & -\frac{1}{\rho_0}\frac{\partial}{\partial z} & 0 & 0 \end{bmatrix} \tag{A1.3}$$

$$D = \begin{bmatrix} -d_x & 0 & 0 & 0 \\ 0 & -d_z & 0 & 0 \\ 0 & 0 & -d_x & 0 \\ 0 & 0 & 0 & -d_z \end{bmatrix}$$

It is necessary to decompose M into a spatial derivative operator matrix N and the remainder D to determine whether the new characteristic matrix N leads to the symplectic structure in the PML layer. If not, the PML cannot be

applied, and another absorbing condition must be imposed. In that case, wave phenomena in the PML layer retain the symplecticity. The remainder matrix D acts as a sponge boundary condition that can be independently considered by simply multiplying by $e^{-d_x \Delta t}$ or $e^{-d_z \Delta t}$ at the update of each variable. For instance, the transformation operator of a second-order symplectic scheme applied to the PML is

$$e^{\Delta t M} \simeq e^{\Delta t D_2} e^{\Delta t N_2} e^{\Delta t D_1} e^{\Delta t N_1} \tag{A1.4}$$

where N_1 and N_2 are the matrices that contain only the upper-right and lower-left submatrices of N, and D_1 and D_2 are the matrices that contain the upper-left and the lower-right submatrices of D.

The PML scheme for the standard second-order equation is considered for system (2.1.21b). The simplest formula invented by Grote and Sim (2010) is

$$\begin{aligned}
\frac{\partial \dot{p}}{\partial t} &= c^2 \left(\frac{\partial^2 p}{\partial x^2} + \frac{\partial^2 p}{\partial z^2} \right) + \frac{\partial \phi_x}{\partial x} + \frac{\partial \phi_z}{\partial z} - (d_x + d_z)\dot{p} - d_x d_z p \\
\frac{\partial \phi_x}{\partial t} &= -d_x \phi_x + (d_z - d_x) \frac{\partial p}{\partial x} \\
\frac{\partial \phi_z}{\partial t} &= -d_z \phi_z + (d_x - d_z) \frac{\partial p}{\partial z} \\
\frac{\partial p}{\partial t} &= \dot{p}
\end{aligned} \tag{A1.5}$$

where ϕ_x and ϕ_z are the auxiliary variables. The characteristic matrix M in the PML zone is:

$$M$$

$$= \begin{bmatrix} -(d_x + d_z) & c^2\left(\frac{\partial^2}{\partial x^2} + \frac{\partial^2}{\partial z^2}\right) - d_x d_z & \frac{\partial}{\partial x} & \frac{\partial}{\partial z} \\ 0 & -d_x & 0 & (d_z - d_x)\frac{\partial}{\partial x} \\ 0 & 0 & -d_z & (d_x - d_z)\frac{\partial}{\partial z} \\ 1 & 0 & 0 & 0 \end{bmatrix} \quad \text{(A1.6)}$$

and $M = N + D$ where

$$N = \begin{bmatrix} 0 & c^2\left(\frac{\partial^2}{\partial x^2} + \frac{\partial^2}{\partial z^2}\right) & \frac{\partial}{\partial x} & \frac{\partial}{\partial z} \\ 0 & 0 & 0 & (d_z - d_x)\frac{\partial}{\partial x} \\ 0 & 0 & 0 & (d_x - d_z)\frac{\partial}{\partial z} \\ 1 & 0 & 0 & 0 \end{bmatrix} \quad \text{(A1.7)}$$

$$D = \begin{bmatrix} -(d_x + d_z) & -d_x d_z & 0 & 0 \\ 0 & -d_x & 0 & 0 \\ 0 & 0 & -d_z & 0 \\ 0 & 0 & 0 & 0 \end{bmatrix}$$

However, the first-order system of N is not symplectic; it is impossible to apply a symplectic time integrator in the PML zone. Other absorbing boundary conditions such as a spongy layer (Cerjan 1995) can be used in the system because the system of N retains a symplectic structure in the layer.

As mentioned in section 4.3, the system in the PML zone is prone to diverge when using a PS method with a large time step. This is why I applied the pretty good sponge boundary invented by Lavelle and Thacker (2007); the system equation in the absorbing layer is slightly different from that of the PML as follows:

$$\frac{\partial p}{\partial t} = -\rho_0 c^2\left(\frac{\partial u}{\partial x} + \frac{\partial v}{\partial z}\right) - (d_x + d_z)p \quad \text{(A1.8)}$$

$$\frac{\partial u}{\partial t} = -\frac{1}{\rho_0}\frac{\partial p}{\partial x} - d_x u$$

$$\frac{\partial v}{\partial t} = -\frac{1}{\rho_0}\frac{\partial p}{\partial z} - d_x v$$

The system is stable. Although a damping of the wavefield is less effective than the PML, this yields better performance than the conventional sponge layers.

A2. Analytic solution

We can derive the analytic solution of the acoustic wave equation in a homogeneous model using the PS method. Two dimensional system of equation (2.1.21a) can be rewritten as follows:

$$\frac{\partial}{\partial t}\begin{bmatrix} p \\ u \\ w \end{bmatrix} = \begin{bmatrix} 0 & -\rho_0 \mathrm{c}^2 \frac{\partial}{\partial x} & -\rho_0 \mathrm{c}^2 \frac{\partial}{\partial z} \\ -1/\rho_0 \frac{\partial}{\partial x} & 0 & 0 \\ -1/\rho_0 \frac{\partial}{\partial z} & 0 & 0 \end{bmatrix} \begin{bmatrix} p \\ u \\ w \end{bmatrix} \tag{A.2.1}$$

This equation can be converted into system ordinary differential form (ODE) via Fourier transformation of the spatial derivatives as follows:

$$\frac{\partial}{\partial t}\begin{bmatrix} \tilde{p} \\ \tilde{u} \\ \tilde{w} \end{bmatrix} = \begin{bmatrix} 0 & \mathbb{i}\,\rho_0 \mathrm{c}^2 k_x & \mathbb{i}\,\rho_0 \mathrm{c}^2 k_z \\ \mathbb{i}\,1/\rho_0 \, k_x & 0 & 0 \\ \mathbb{i}\,1/\rho_0 \, k_z & 0 & 0 \end{bmatrix} \begin{bmatrix} \tilde{p} \\ \tilde{u} \\ \tilde{w} \end{bmatrix} \tag{A.2.2}$$

Then, the acoustic wave solution in the time-wavenumber domain is

$$\tilde{y} = e^{t\widetilde{M}} \tilde{y}_0. \tag{A.2.3}$$

where

$$e^{t\widetilde{M}} = \begin{bmatrix} \cos(ckt) & \frac{\mathbb{i}\rho c k_x \sin(ckt)}{k} & \frac{\mathbb{i}\rho c k_z \sin(ckt)}{k} \\ \frac{\mathbb{i}\rho c k_x \sin(ckt)}{k} & \frac{{k_z}^2 + {k_x}^2 \cos(ckt)}{k^2} & \frac{k_x k_z(-1+\cos(ckt))}{k^2} \\ \frac{\mathbb{i}\rho c k_z \sin(ckt)}{k} & \frac{k_x k_z(-1+\cos(ckt))}{k^2} & \frac{{k_z}^2 + {k_x}^2 \cos(ckt)}{k^2} \end{bmatrix} \tag{A.2.4}$$

and $\widetilde{M}$ is a system matrix of equation (A.2.2). $\tilde{y}_0$ is an initial value in the time-wavenumber domain that can be easily calculated by Fourier transform in the x- and z-directions. $\tilde{y}$ is a solution vector in the time-wavenumber

domain that requires the inverse Fourier transform to convert into the wavefield in the spatial domain at time t as follows:

$$y = FFT^{-1}\left[e^{t\tilde{M}}FFT[y_0]\right]. \qquad \text{(A.2.5)}$$

Appendix B. Matlab codes

B1. Arbitrary-order symplectic time integrator

```
clear all;
close all;
clc;

% Computational domain
Nx = 512;
Nz = 512;
Lx = 4*pi;
Lz = 4*pi;
hx = Lx/Nx;
hz = Lz/Nz;
x = hx*(1:Nx)';
z = hz*(1:Nz);
[xx,zz] = meshgrid(x,z);

% Wavenumber domain
kx0 = 2*pi/Lx*[0:Nx/2-1 0 -Nx/2+1:-1];
kz0 = 2*pi/Lz*[0:Nz/2-1 0 -Nz/2+1:-1];
[kx,kz] = meshgrid(kx0, kz0);

% physical properties
cp  = 5*ones(Nz,Nx);
rho = ones(Nz,Nx);

% Time stepping
Tmax = 20;
dt = 0.02;
t = dt:dt:Tmax;

% physical variables
p = exp(-80*((xx-Lx/2).^2 + (zz-Lz/2).^2));
u = zeros(Nz,Nx);
w = zeros(Nz,Nx);

% intermediate variables for symplectic & Lax-wendroff
du_0 = zeros(Nz,Nx);
du_2 = zeros(Nz,Nx);
dw_0 = zeros(Nz,Nx);
dw_2 = zeros(Nz,Nx);
dp_0 = zeros(Nz,Nx);
dp_2 = zeros(Nz,Nx);

% non-symplectic method
p_new = zeros(Nz,Nx);
```

```
u_new = zeros(Nz,Nx);
w_new = zeros(Nz,Nx);


%CFL
CFL_sqare = pi^2*max(max(cp))^2*dt^2*(1/hx^2+1/hz^2);
theta = sqrt(CFL_sqare)

m_expansion = 14;

%%% start time stepping %%%

tic

% Half time stepping
du_0 = - 0.5*dt./rho.*real(ifft2(1i*kx.*fft2(p)));
dw_0 = - 0.5*dt./rho.*real(ifft2(1i*kz.*fft2(p)));
u = u + du_0;
w = w + dw_0;
% Lax-Wendroff
for m=1:m_expansion
    du_2 =
0.125*dt*dt/(m*(2*m+1))./rho.*(real(ifft2(1i*kx.*fft2(rho
.*cp.*cp.*(real(ifft2(1i*kx.*fft2(du_0)))))))+real(ifft2(
1i*kx.*fft2(rho.*cp.*cp.*real(ifft2(1i*kz.*fft2(dw_0)))))
));
    dw_2 =
0.125*dt*dt/(m*(2*m+1))./rho.*(real(ifft2(1i*kz.*fft2(rho
.*cp.*cp.*(real(ifft2(1i*kx.*fft2(du_0)))))))+real(ifft2(
1i*kz.*fft2(rho.*cp.*cp.*real(ifft2(1i*kz.*fft2(dw_0)))))
));
    u = u + du_2;
    w = w + dw_2;
    du_0 = du_2;
    dw_0 = dw_2;
end

for i=1:length(t)

    % i=0 : 2nd order symplectic
    dp_0 = -
dt*rho.*cp.*cp.*(real(ifft2(1i*kx.*fft2(u)))+real(ifft2(1
i*kz.*fft2(w))));
    p = p + dp_0;
    % i>0: Lax-Wendroff expansion
    for m=1:m_expansion
       dp_2
=0.125*dt*dt/(m*(2*m+1))*rho.*cp.*cp.*(real(ifft2(1i*kx.*
fft2(1./rho.*real(ifft2(1i*kx.*fft2(dp_0))))))+real(ifft2
(1i*kz.*fft2(1./rho.*real(ifft2(1i*kz.*fft2(dp_0)))))));
       p = p + dp_2;
       dp_0 = dp_2;
```

```
    end


    % i=0 : 2nd order symplectic
    du_0 = - dt./rho.*real(ifft2(1i*kx.*fft2(p)));
    dw_0 = - dt./rho.*real(ifft2(1i*kz.*fft2(p)));
    u = u + du_0;
    w = w + dw_0;
    % i>0: Lax-Wendroff expansion
    for m=1:m_expansion
       du_2 =
0.125*dt*dt/(m*(2*m+1))./rho.*(real(ifft2(1i*kx.*fft2(rho
.*cp.*cp.*(real(ifft2(1i*kx.*fft2(du_0)))))))+real(ifft2(
1i*kx.*fft2(rho.*cp.*cp.*real(ifft2(1i*kz.*fft2(dw_0)))))
));
       dw_2 =
0.125*dt*dt/(m*(2*m+1))./rho.*(real(ifft2(1i*kz.*fft2(rho
.*cp.*cp.*(real(ifft2(1i*kx.*fft2(du_0)))))))+real(ifft2(
1i*kz.*fft2(rho.*cp.*cp.*real(ifft2(1i*kz.*fft2(dw_0)))))
));
       u = u + du_2;
       w = w + dw_2;
       du_0 = du_2;
       dw_0 = dw_2;
    end

     % plot animation "mesh"
     if mod(i,2) == 0
       mesh(xx,zz,p);
       xlim([0 Lx]);
       ylim([0 Lz]);
       zlim([-0.5 1]);
       pbaspect([Lx Lz Lz*0.5]);
       caxis([-0.2, 1]);
       title(num2str(i*dt, '%10.5e\n'));
       pause(.00001)
     end

end

toc
```

B2. Analytic solution

```
clear all;
clc;

% Computational domain
Nx = 512;
Nz = 512;
Lx = 4*pi;
Lz = 4*pi;
hx = Lx/Nx;
hz = Lz/Nz;
x = hx*(1:Nx)';
z = hz*(1:Nz);
[xx,zz] = meshgrid(x,z);

% Wavenumber domain
kx0 = 2*pi/Lx*[0:Nx/2-1 0 -Nx/2+1:-1];
kz0 = 2*pi/Lz*[0:Nz/2-1 0 -Nz/2+1:-1];
[kx,kz] = meshgrid(kx0, kz0);

% target mement t
t = 20;

% physical variables
p_0 = exp(-80*((xx-Lx/2).^2 + (zz-Lz/2).^2));
u_0 = zeros(Nz,Nx);
w_0 = zeros(Nz,Nx);

% variables in wavenumber domain
p_k0 = zeros(Nz,Nx);
u_k0 = zeros(Nz,Nx);
w_k0 = zeros(Nz,Nx);
p_k1 = zeros(Nz,Nx);
u_k1 = zeros(Nz,Nx);
w_k1 = zeros(Nz,Nx);

% solution at 't'
p = zeros(Nz,Nx);
u = zeros(Nz,Nx);
w = zeros(Nz,Nx);

% physical properties
cp  = 5*ones(Nz,Nx);
rho = ones(Nz,Nx);

% onestep solution %
p_k0 = fft2(p_0);
u_k0 = fft2(u_0);
w_k0 = fft2(w_0);
p_k1 = cos(cp.*sqrt(kx.^2+kz.^2)*t).*p_k0 -
```

```
1i*kx.*rho.*cp.*sin(cp.*sqrt(kx.^2+kz.^2)*t)./sqrt(sqrt(k
x.^2+kz.^2)).*u_k0 -
1i*kz.*rho.*cp.*sin(cp.*sqrt(kx.^2+kz.^2)*t)./sqrt(sqrt(k
x.^2+kz.^2)).*w_k0;
u_k1 = -
1i*kx./cp./rho.*sin(cp.*sqrt(kx.^2+kz.^2)*t)./sqrt(sqrt(k
x.^2+kz.^2)).*p_k0 +
(kz.^2+kx.^2.*cos(cp.*sqrt(kx.^2+kz.^2)*t))./(kx.^2+kz.^2
).*u_k0 + (kx.*kz.*(1-
cos(cp.*sqrt(kx.^2+kz.^2)*t)))./(kx.^2+kz.^2).*w_k0;
w_k1 = -
1i*kz./cp./rho.*sin(cp.*sqrt(kx.^2+kz.^2)*t)./sqrt(sqrt(k
x.^2+kz.^2)).*p_k0 + (kx.*kz.*(1-
cos(cp.*sqrt(kx.^2+kz.^2)*t)))./(kx.^2+kz.^2).*u_k0 +
(kx.^2+kz.^2.*cos(cp.*sqrt(kx.^2+kz.^2)*t))./(kx.^2+kz.^2
).*w_k0;
% Nan check
p_k1(1,1) = p_k0(1,1);
p_k1(1,1+Nx/2) = p_k0(1,1+Nx/2);
p_k1(1+Nx/2,1) = p_k0(1+Nx/2,1);
p_k1(1+Nx/2,1+Nx/2) = p_k0(1+Nx/2,1+Nx/2);
% Nan check
u_k1(1,1) = u_k0(1,1);
u_k1(1,1+Nx/2) = u_k0(1,1+Nx/2);
u_k1(1+Nx/2,1) = u_k0(1+Nx/2,1);
u_k1(1+Nx/2,1+Nx/2) = u_k0(1+Nx/2,1+Nx/2);
% Nan check
w_k1(1,1) = w_k0(1,1);
w_k1(1,1+Nx/2) = w_k0(1,1+Nx/2);
w_k1(1+Nx/2,1) = w_k0(1+Nx/2,1);
w_k1(1+Nx/2,1+Nx/2) = w_k0(1+Nx/2,1+Nx/2);
% solution
p = real(ifft2(p_k1));
u = real(ifft2(u_k1));
w = real(ifft2(w_k1));

% plot
figure(11);
mesh(xx,zz,p);
%axis equal;
xlim([0 Lx]);
ylim([0 Lz]);
zlim([-0.5 1]);
pbaspect([Lx Lz Lz*0.5]);
caxis([-0.2, 1]);
title(num2str(t, '%10.5e\n'));

 % Binary file write
fileID_p =
fopen('output_analytic_5000mps_512/p_analytic_5000mps_512
_20s.bin','w');
fwrite(fileID_p, p, 'float32');
fclose(fileID_p);
```

초록

음향 파동방정식에 적용된 유사 스펙트럴 방법을 이용한 임의 차수의 심플렉틱 시간 적분법

이 재 준

협동과정 계산과학전공

서울대학교 대학원

해밀토니안 역학으로 표현된 시스템은 일반적으로 심플렉틱하다. 해밀토니안 시스템을 정확히 모사하기 위해서 심플렉틱 시간 적분법을 사용한다. 이 때, 수치적으로 계산된 해의 에너지 혹은 일반화 에너지의 총량, 즉, 해밀토니안이 보존되기 때문이다. 본 연구에서는 음향파동 방정식이 심플렉틱 시스템임을 밝힌다. 이 후 임의의 시간 차수로 확장이 가능한 심플렉틱 시간 적분법을 제시한다. 이는 랙스-웬드로프 전개법을 기반으로 하며, 압력장 그리고 이와 다른 종류의 변수, 가령 속도 혹은 압력장의 시간 변화율 등을 서로 엇갈린 시간 축에 배치시킨 후 이를 이산화하여 정리 된 식이다. 랙스-웬드로프 전개는 선형화된 시스템의 변환 매트릭스의 테일러 전개이며, 음향 파동방정식은 위와 같은 전개에서 유사 미분 오퍼레이터로 환원되는데 이는 쌍곡 사인함수임을 밝혔다. 이를 이용하면 테일러 전개 외에 자코비-앵거 전개 등의 수렴 속도가 뛰어난 다른 전개법을 사용하여 파동 방정식 시스템의 오퍼레이터를 근사할 수 있다. 본 연구에서 제시된 시간 적분법은 우수한 안정 특성을 보이며 이는 심플렉틱이라는 성질을 만족하지 않는 시간 차분 방식에 비해 같은 조건에서 더욱 안정적이다. 더불어 시간 스텝 당 위상 변화 오차가 적기 때문에 장시간 시뮬레이션에 적합하다. 위상 분석 결과를 통해 시간 스텝 간격이 크고 시간 차수가 높을수록 컴퓨팅 파워를 줄일 수 있음을 도출하였다. 다만 소스 웨이브렛 문제를 풀 경우 소

스를 정확히 모사하기 위한 최대 시간 간격을 고려해야 한다. 임의 차수 심플렉틱 시간 적분법을 상속도 속도 모델을 이용한 초기값 문제에 적용하였으며 해석해와 비교한 결과 시간 스텝길이가 충분히 긴 경우에도 해석해와 동등한 계산 결과를 도출할 수 있다. 비균질 모델이서도 마찬가지로 시간 간격과 관계 없이 동일한 모델링 결과를 산출함을 확인하였다. 이는 제안된 방법은 소스 문제에도 효율적으로 적용할 수 있다. 다만 다소 긴 시간 간격을 사용한 경우 스펀지 흡수 경계조건이 효율적으로 작동하지 않을 수 있으며 해결을 요구하는 문제로 남아있다.

주요어 : 심플렉틱 시간 적분법, 음향 파동방정식, 유사 스펙트럴 방법, 스펙트럴 정확도
학번 : 2012-30910